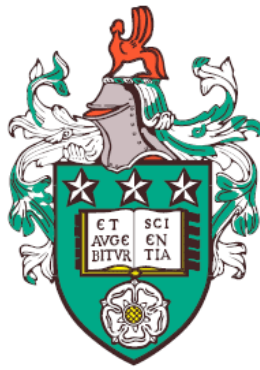


Tracking space debris using directional statistics



Shambo Bhattacharjee
School of Mathematics
University of Leeds

A thesis submitted for the degree of
Doctor of Philosophy

April 2020

Intellectual Property and Publication Statements

The candidate confirms that the work submitted is his own and that appropriate credit has been given where reference has been made to the work of others. This copy has been supplied on the understanding that it is copyright material and that no quotation from the thesis may be published without proper acknowledgment. The right of Shambo Bhattacharjee to be identified as Author of this work has been asserted by Shambo Bhattacharjee in accordance with the Copyright, Designs and Patents Act 1988.

Acknowledgements

My PhD was really a good experience. First of all, I would like to thank my family for always supporting my work. Next, I would like to thank my supervisor Prof. John. T. Kent for his continuous support and for trusting me. I would also like to thank the AFOSR for funding my PhD, this PhD was impossible without their funding. Further, I would like to thank my other PhD supervisors (Weston R. Faber, Islam I. Hussein and Moriba K. Jah) for their valuable inputs and helps.

In addition, I am thankful to Prof. Hugh Hill (International Space University) for continuously providing me mental support and believing in my abilities. Finally, I would like to thank Prof. Chris Welch (International Space University), Dr. Marc Kuchner (NASA GSFC) and others for their help and support.

Abstract

One of the main concerns in space situational awareness is to keep track of the large number of space objects, including both satellites and debris, orbiting the earth. The state of an orbiting object indicates the position and velocity of the object and it is generally represented using a 6-dimensional state vector. Observations typically take the form of angles-only measurements from ground-based telescopes. Two specific challenges are the tracking of objects and the association of objects. Ideas from the directional statistics can be used to tackle both of these challenges.

There are two sets of contributions made in this thesis. The first set of contributions deals with the tracking of an orbiting object. In general, the filtering or tracking problem is simplest when the joint distribution of uncertainties in the state vector and the observation vector is normally distributed. To achieve this goal, the “Adapted SStructural (AST)” coordinate system has been developed to describe the orbiting object and the measurements of the object. The propagated orbital uncertainty represented using the AST coordinate system is approximately Gaussian under a wide range of conditions and as a result this coordinate system is suitable for using a Kalman filter for tracking space objects. A comparative study has been performed to understand behavior of different non-linear Kalman filters. Further, two new Kalman filters, namely the Observation-Centered extended Kalman filter and Observation-Centered unscented Kalman filter, have been developed. Various uses of the AST coordinate system are described using suitable examples.

The second set of contributions is related to the representation of the 2-dimensional uncertainty, associated with the angles-only position. The concept of the newly developed “Adapted Spherical (ASP)” coordinate system is described in detail. Several examples are provided to discuss the usefulness of the ASP coordinate system for solving association problems. In addition, limitations of the ASP coordinate system are also highlighted. Especially for a break-up event scenario, the propagated point cloud in the ASP coordinate system displays a “bow-tie” or “pinching” pattern when the propagation period is a close multiple of half orbital period. A new “Pinched-Normal (PN)” distribution has been developed to understand the reason. Finally, the distribution of the radial component is analyzed.

Abbreviations

AST	Adapted STructural (coordinate system)
ASP	Adapted SPherical (coordinate system)
PN	Pinched-Normal (distribution)
ESA	European Space Agency
ECI	Earth-centered Inertial
SSA	Space Situational Awareness
SDS	Simplified Dynamic System
STT	State Transition Tensor
PCE	Polynomial Chaos Expansion
GMM	Gaussian Mixture Models
PCM	Polynomial Chaos Model
EKF	Extended Kalman Filter
UKF	Unscented Kalman Filter
IEKF	Iterated Extended Kalman Filter
IUKF	Iterated Unscented Kalman Filter
OCEKF	Observation-centred Extended Kalman Filter
OCUKF	Observation-centred Unscented Kalman Filter
RTN	Radial Tangential Normal
RAAN	Longitude of the Ascending Node (Right Ascension of the Ascending Node)
LEO	Low Earth Orbit
MEO	Medium Earth Orbit
GEO	Geosynchronous Equatorial Orbit
HEO	Highly Eccentric Orbit
CRTN	Central RTN

Index of Notation (Chapter 1 to Chapter 7)

$\mathbf{x}^{\text{ECI}}(0)$	Cartesian-ECI position at $t = 0$
$\dot{\mathbf{x}}^{\text{ECI}}(0)$	Cartesian-ECI velocity at $t = 0$
$\mathbf{x}^{\text{ECI}}(t)$	Cartesian-ECI position at $t = t_1$
$\dot{\mathbf{x}}^{\text{ECI}}(t)$	Cartesian-ECI velocity at $t = t_1$
t, t_1	time
b	length of the minor axis
a	length of the major axis
e	orbital eccentricity
$T(t)$	true anomaly at time t
$r(t)$	radial distance at time t
$M(t)$	mean anomaly at time t
$E(t)$	eccentric anomaly at time t
$F_{\text{M-to-T}}$	function for computing true anomaly from the mean anomaly
$F_{\text{T-to-M}}$	function for converting mean anomaly from the true anomaly
μ	gravitational constant
$\mathbf{u}, \mathbf{v}, \mathbf{w}$	$\mathbf{u}, \mathbf{v}, \mathbf{w}$ coordinate system, \mathbf{w} is normal to the $\mathbf{u} - \mathbf{v}$ plane
\mathbf{h}, h	angular momentum vector and angular momentum
\mathbf{e}	eccentricity vector
$\square p$	orbital period
n	mean motion
i	inclination angle
\mathbf{N}_{RAAN}	node vector
Ω	RAAN
ω	argument of perigee
θ_p	angle of perigee in true anomaly scale
ϕ_p	angle of perigee in mean anomaly scale
θ	true longitude in true anomaly scale or break angle
ϕ	true longitude in mean anomaly scale or re-invented break angle
$(c), (d)$	superscripts to represent the central and deviated states respectively
$x_1(t), x_2(t), x_3(t)$	propagated Cartesian position vector elements
$\dot{x}_1(t), \dot{x}_2(t), \dot{x}_3(t)$	propagated Cartesian velocity vector elements

Index of Notation (Chapter 1 to Chapter 7)

ECI_1, \dots, ECI_6	Cartesian elements
K_1, \dots, K_6	Keplerian elements
E_1, \dots, E_6	Equinoctial elements
A_1, \dots, A_6	AST elements
$\mathbf{G}^{(c)}$	rotation matrix for computing Cartesian-CRTN state vectors
\mathbf{x}^{CRTN}	Cartesian-CRTN position
$\dot{\mathbf{x}}^{\text{CRTN}}$	Cartesian-CRTN velocity
$\mathbf{x}^{\text{CRTN-unit}}$	unit vector representation of the Cartesian-CRTN position
$\mathbf{A}^{(d)}$	deviated AST coordinate system
r_a, r_p	apogee and perigee distances
v_a, v_p	velocities at apogee and perigee
$P_\sigma \%$	% of geometric mean of r_a and r_p
$P_\tau \%$	% of geometric mean of v_a and v_p
ϵ, δ	small deviations
A, B, C	position (element 1) and velocity values (elements 2 and 3)
ψ	true latitude
ψ_1	standardized true latitude
f_1, f_2	AST elements 4 and 5
$\mathbf{x}_k, \mathbf{z}_k$	state and observation vectors
$\mathbf{w}_k, \mathbf{v}_k$	system and measurement noises
$\mathbf{F}_k, \mathbf{H}_k$	state transition matrix and observation matrix
K_k	optimal Kalman gain
$\mu_x^{\text{Kalman}}, \mu_{x z_{\text{obs}}}^{\text{Kalman}}, x_{\text{obs}}$	prior, posterior and observation means
l, N	dimension and no. of data points in a point cloud
$\alpha^{\text{UKF}}, \beta^{\text{UKF}}, \kappa^{\text{UKF}}$	UKF tuning parameters
$\theta_{\text{obs}}, \psi_{\text{obs}}$	observation angles (observed longitude and latitude)
ϕ_{obs}	observed longitude in mean anomaly scale
obs	subscript “obs” is related to the observation
θ_{true}	true longitude in true anomaly scale (ASP coordinate element)
$\triangleright f(\psi(t), \theta(t)), \triangleright p(\psi(t), \theta(t))$	density function, posterior probability
$\triangleright P(\psi(t), \theta(t))$	tail probability

Theme of the thesis

This thesis deals with three key ideas. They are listed below.

- (1) Representation of the propagated state vector and the associated uncertainty.

Contribution. 6-dimensional “Adapted STructural (AST)” coordinate system to represent the state and the associated uncertainty of an orbiting object at time t .

Note that under Keplerian dynamics only the third AST coordinate ($A_3(t)$) changes with time.

Purpose. Under Keplerian dynamics the propagated orbital uncertainty represented using the AST coordinate system is approximately Gaussian for all values of t .

- (2) Representation of the propagated state vector in the ambient coordinate system.

Contributions.

- 2-dimensional “Adapted SPherical (ASP)” coordinate system to represent the propagated angles-only (the latitude and the longitude or the *true* angles) vector (plus associated uncertainty) of an orbiting object at time t .

Throughout the thesis the word “true” is used in two senses. First, it is the “true state” of nature, i.e., the actual (but unknown) state of the orbiting object. Second, it means the “true anomaly” or the angular position of a moving space object along its orbit (see Chapter 1 for more details).

- Newly developed “Pinched-Normal (PN)” distribution to understand the break-up event scenario and the distribution of the latitude at time t .

Purpose. These two propagated angles (true angles) provide information related to the observation angles. In addition, the propagated angles-only position in ASP coordinates follows the PN distribution, and the standardized propagated angles-only position follows the bivariate normal distribution.

- (3) Filtering or tracking space object using the iterated or newly developed “Observation-Centered (OC)” filters.

Contribution. Newly developed Observation-Centered Kalman filters to tackle space object tracking problem. Performance wise iterated and OC filters are similar (based on the examples provided in this thesis) but OC filters don’t require iteration.

Purpose. Standard non-linear Kalman filters (such as, the EKF and UKF) often perform poorly. The OC filters for the space object tracking problem perform much better than the EKF and UKF under varying conditions.

This Page is Intentionally Left Blank

Contents

1	Introduction	28
1.1	Introduction	28
1.2	Thesis contributions	30
1.3	Two uses of the word Keplerian	33
1.4	Organization of the thesis	33
1.5	Outline of the rest of this chapter (Key contributions)	35
1.6	Relation to other chapters	36
1.7	Mathematics of orbital dynamics	36
1.7.1	Orbital dynamics in 2 dimensions	37
1.7.2	Three angles in orbital dynamics	38
1.7.3	Equations of orbital motion in 3 dimensions	39
1.7.4	Orbital dynamics in 3 dimensions	45
1.7.5	Classification of various orbits	45
1.7.6	Introduction to the standard coordinate systems	47
1.7.6.1	Cartesian coordinate system	47
1.7.6.2	Keplerian coordinate system	48
1.7.6.3	Equinoctial coordinate system	49
1.7.7	Different coordinate systems and reference frames	50
1.8	Statistical variability in orbital dynamics	52
1.8.1	Representing the orbital uncertainty	52
1.8.2	Statistical analysis of propagated distributions	54
1.9	Example 1.1., problems with the standard coordinate systems, simple illustration	55
1.10	Tracking Problem	56
1.11	Association Problem	58

1.12 Thesis summary	58
2 Representing uncertainties associated with the propagated state vector	63
2.1 Introduction	63
2.2 Chapter summary and key contributions	63
2.3 Relation to other chapters	64
2.4 The AST-CRTN coordinate system	64
2.5 Analyzing the AST-CRTN coordinate system	67
2.5.1 A first order representation for initial AST-CRTN coordinates	68
2.5.2 Linearity analysis for initial AST-CRTN coordinates . . .	73
2.5.3 Point cloud propagation	75
3 Representing uncertainties associated with the propagated observation vector	83
3.1 Introduction	83
3.2 Chapter summary and key contributions	84
3.3 Relation to other chapters	85
3.4 The ASP-CRTN coordinate system	86
3.4.1 Example 3.1., distribution of the propagated angles-only elements	87
3.5 Uncertainty representation for the ASP-CRTN coordinate	89
3.5.1 Propagated angles-only positions during break-up event . .	90
3.5.2 Treating the pinching problem and the Pinched-Normal distribution	91
3.6 A brief summary based on the behavior of various propagated angles	92
3.7 Velocity-only sigma points for break-up event analysis	95
3.7.1 Sigma points propagation	96
3.7.2 Limitations of Velocity-only sigma points based system . .	97
3.8 Application of Sigma points	98
3.8.1 Computing the pinching time span	99
3.9 Distribution of the Radial component	102

4	Filtering, part 1	110
4.1	Introduction	110
4.2	Key contributions	111
4.3	Relation to other chapters	111
4.4	The classic Kalman filter	112
4.5	Example 4.1., 1-dimensional linear tracking example	113
4.6	Non-linear Kalman filters	116
4.6.1	The EKF, IEKF and OCKF (1-dimensional setting)	116
4.6.2	The UKF, IUKF and OCUKF (1-dimensional setting)	118
4.7	Intuition behind the iterated and observation-centered filters	119
4.8	Example 4.2., idealized analytic example	120
4.9	Application to 1-dimensional orbital dynamics	121
4.10	Performance analysis	124
5	Filtering, part 2	126
5.1	Introduction	126
5.2	Key contributions	127
5.3	Relation to other chapters	127
5.4	Simulated Tracking example using the AST-IUKF algorithm	128
5.4.1	Example 5.1.	129
5.5	The Observation-Centered Filter for solving higher dimensional tracking problem, approach 1	130
5.5.1	Stage-1, the Observation-Centered filtering stage	131
5.5.2	Stage-2, the non-linear filtering stage	132
5.6	The Observation-Centered Filter, approach 2	133
5.6.1	Stage-1, the Observation-Centered filtering stage	133
5.6.2	Stage-2, the non-linear filtering stage	133
5.7	OCKF example	135
6	Application of the propagated observation vector for solving as- sociation problems	137
6.1	Introduction	137
6.2	Key contributions	138
6.3	Relation to other chapters	139

6.4	Association problem	140
6.5	Discriminant analysis	140
6.6	Tail probability	141
6.7	Solving association problem for non break-up and break-up events	141
6.7.1	Association problem related to the non break-up event . .	141
6.7.2	Association problem related to the break-up event	142
6.7.3	Note on the distribution of longitude and the related density	142
6.8	Association problems	143
6.8.1	Example 6.1. Solving association problem for a non break-up event (association problem)	143
6.8.2	Example 6.2. Solving association problem for a break-up event (association problem)	144
6.8.3	Example 6.3. Solving the association problem for a mixture of break-up and non break-up events (association problem)	146
6.8.4	Example 6.4. When the object custody is ambiguous (filtering-association problem)	147
7	Conclusion and Future directions	155
7.1	Conclusion	155
7.2	Future directions	157
7.3	Observer-centric analysis on the propagated angles-only position vector	157
7.3.1	Example 7.1. Observer-centric analysis based on altitude .	158
7.3.2	Example 7.2. Observer-centric analysis based on the propagation period	159
7.3.3	Remarks	161
7.4	Analyzing sensitivity of various multivariate normality tests . . .	162
A	More on orbital dynamics	164
A.1	Orbital dynamics	164
A.2	More examples (propagation)	167
A.2.1	Cartesian-ECI coordinate system under short term propagation	167
A.2.2	Keplerian coordinate system for a near circular orbit . . .	168

A.2.3	Propagated angles-only position (true angles) vector for a HEO orbit when the propagation period is large	170
A.2.4	Propagated angles-only position vector for a near circular LEO orbit	172
A.3	True anomaly vs. mean anomaly for various eccentricity values ($F_{M \rightarrow \tau \rightarrow T}$ function)	173
A.4	True anomaly and eccentric anomaly (simpler representation)	174
B	Miscellaneous results	175
B.1	The EKF and UKF computing steps	175
B.1.1	The extended Kalman filter	175
B.1.2	The unscented Kalman filter	176
B.2	Rotation matrix	178
B.3	Mahalanobis distance vs. Euclidean distance	178
B.4	The density computation for a bivariate normal distribution	180
B.5	The Gram-Schmidt process	181
B.6	Taylor series expansion	181
B.7	Matrix basics	182
B.8	Key MATLAB functions used in this thesis	183
C	List of objects	185
D	Papers	187
References		197

List of Tables

1.1	Coordinate systems and reference bases	50
2.1	Normality test results. Here $p_{\text{skewness}}, p_{\text{kurtosis}}$ represent p-values for the skewness and kurtosis respectively.	81
4.1	A summary on various non-linear Kalman filters. In this table, the EKF and UKF indicate the Extended Kalman Filter and the Unscented Kalman Filter respectively.	111
4.2	Comparison between various approximations to the posterior distribution for idealized example in Section 4.8. The exact posterior distribution is centered at the value given in the column “Truth”. The IEKF and OCEKF results match the exact result here. However, the EKF gives the wrong value. The exact posterior distribution has zero variance and all three filters (EKF, IEKF and OCEKF) produce the right value.	121
4.3	The prior means μ_x^{Kalman} and its standard deviations ξ_1 , plus the observations z_{obs} and its standard deviations ξ_2 for Examples 4.3. and 4.4. In each case three choice for the error standard deviation ξ_2 are considered. The value of $h_{\text{Kalman}}^{-1}(z_{\text{obs}}) = x_{\text{obs}}$ is also given.	124
4.4	Posterior means and standard deviations (s.d.) from various filters for Examples 4.3. (a,b,c) and 4.4. (a,b,c).	125
5.1	Posterior means and standard deviations for $A_3(t_1)$ in Example 5.2., computed using various filters.	136

LIST OF TABLES

- 7.1 Here “M. p-val. 1” and “M. p-val. 2” denote multivariate p-values for skewness and kurtosis respectively computed using Mardia’s MVN p-value computation method. “Hz p-val” indicates p-value obtained using the Henze-Zerkler’s MVN computation. Finally, “Lon. p-val.” and “Lat. p-val” indicate p-values for the longitude and latitude respectively computed using the Shapiro-Wilk’s test. 163
- B.1 Comparing the Mahalanobis distance and the Euclidean distance. 180

List of Figures

1.1	Representing an orbit in 2 dimensions (Not scaled to size). Various orbital elements in a 2-dimensional orbital plane are shown in this image. Note that only the true anomaly (T) and the radial distance (distance between point f1 to point L) change with time. The perigee and apogee are indicated by points P and A respectively.	37
1.2	The true, mean and eccentric anomalies (Not scaled to size). The true, mean and eccentric anomalies are highlighted in this image. The true anomaly is measured with respect to the actual location of the object (in the ellipse). The object is located at the point L. Also see image A.8	40
1.3	Orbital dynamics in three dimensions (Not scaled to size). An orbiting object in Keplerian dynamics. The plot shows the reference and orbital planes together with their preferred directions and normal directions. The angles ω , Ω , i and $T(t)$ are highlighted.	41
1.4	Classification based on the altitude (Not scaled to size). LEO, MEO and GEO. Note that this image is only for visual illustration, no scaling is applied here.	46
1.5	Classification based on the inclination (Not scaled to size). A is a prograde orbit and B is a retrograde orbit.	47

1.6	Reconstructing the central and deviated state (Not scaled to size). The left panel (A) shows both the central and deviated states <i>before</i> performing the rotation. The right panel (B) shows both the states <i>after</i> performing the rotation. Note that the red dotted ellipse and the red dotted line denote the <i>deviated</i> state and the deviated normal direction respectively, the black ellipse and the black line indicate the <i>central</i> state and the central normal direction.	53
1.7	Example 1.1., bounded range problem, part 1. The unit sphere with two concentrated point clouds are plotted, one near the equator (A) and one near the north pole (B).	56
1.8	Example 1.1., bounded range problem, part 2. Spherical coordinates for both distributions.	57
1.9	Association problem. Two overlapping distributions A and B for the angles-only part of a state vector. The distributions are represented by point clouds in the tangent plane to the unit sphere in terms of the latitude and longitude in degrees. In addition three possible observations, labeled 1,2,3, have been highlighted.	59
1.10	Thesis contributions, part 1. Uncertainty propagation in different coordinate systems.	61
1.11	Thesis contributions, part 2. Applications of newly developed coordinate systems to the filtering and association problems.	62
2.1	Example 2.1., linearity example, part 1. Linearity analysis at time $t = 0$ showing plots of each AST-CRTN coordinate against the first three Cartesian-CRTN coordinates. See also Fig. 2.2.	76
2.2	Example 2.1., linearity example, part 2. Linearity analysis at time $t = 0$ showing plots of each AST-CRTN coordinate against the last three Cartesian-CRTN coordinates.	77
2.3	Example 2.2., propagation example, Cartesian-CRTN coordinates. Propagated point cloud in Cartesian-CRTN coordinates. First three elements represent the propagated position vector (km) and last three elements indicate the propagated velocity vector (km/sec).	78

2.4	Example 2.2., propagation example, Keplerian-CRTN coordinates. Propagated point cloud in Keplerian-CRTN coordinates.	79
2.5	Example 2.2., propagation example, Equinoctial-ECI coordinates. Propagated point cloud in Equinoctial-ECI coordinates.	80
2.6	Example 2.2., propagation example, AST-CRTN coordinates. Propagated point cloud in AST-CRTN coordinates. All the histograms and scatter plots are approximately normal.	81
3.1	Example 3.1., propagated angles-only components. Propagated angles-only elements. Note that the joint distribution of the longitude and the latitude can be approximated using a bivariate normal distribution. Initial conditions are mentioned in Section 3.4.1.	88
3.2	Example 3.2., pinching example, part 1. Angles-only part of the propagated point cloud has been shown for various propagation times (much before, just before, during and just after pinching). Subplot (a) highlights a scenario which is much before the pinching. The propagation period is 0.8 central orbital period. The joint distribution is approximately <i>bivariate normal</i> . Subplot (b) shows the angles-part <i>just before</i> the pinching behavior and the propagation period is 0.98 central orbital period. Subplot (c) illustrates the <i>exact pinching</i> behavior, a “bow-tie” or “butterfly” pattern is clearly visible here. Finally, Subplot (d) displays the propagated point cloud <i>just after</i> the pinching. Note that (b), (c) and (d) are not bivariate normal.	91
3.3	Example 3.2., pinch-corrected distribution, part 2. The first element is the longitude, the second and third elements are original and scaled/standardized latitudes respectively. The joint distribution of the longitude (θ) and the scaled latitude (ψ_1) can be approximated using a bivariate normal distribution. The initial conditions are same as Fig. 3.2 and the propagation time is exactly 1 central orbital period, as in Fig. 3.2, Subplot (c).	93

3.4	Example 3.3., sigma points propagation. Illustration of sigma points after 0.8 central orbital periods (for $\tau_1 = 1, 2, 3$ and 3.5τ respectively). The data are plotted in ASP-CRTN coordinates with the “latitude” $\psi(t)$ and the “longitude” ($[\theta(t) - \theta^{(c)}(t)]$) in degrees. Here, $*$ denotes the base point; squares denote the $\pm\tau_1 e_1$ sigma points, diamonds denote the $\pm\tau_1 e_2$ sigma points, and circles denote the $\pm\tau_1 e_3$ sigma points. Plus perturbations are indicated by an open symbol; minus perturbations by a closed symbol.	97
3.5	Example 3.4., sigma points during a pinching event. Representation of sigma points during a pinching event. Clearly, scales for the longitude are approximately same (or close) in both the point cloud and sigma points. However, sigma points are unable to mimic the point cloud behavior for the latitude. The rectangle located just above the pinching location is the zoomed in version of the small (dashed) rectangle situated exactly at the center of the image.	99
3.6	Example 3.5., approximate pinching duration computation. Subplot (a) indicates the approximate beginning of the pinching effect and Subplot (b) shows the approximate ending of the pinching effect. From this analysis it can be concluded that sigma points works fairly well in computing the pinching duration.	103
3.7	Example 3.6., distribution of the radial component, part 1. This plot shows distribution of the radial component based on the propagation time and the starting location. The first plot (a) shows the distribution when the starting location is the perigee ($T = 0^\circ$) and the propagation period is small (0.5 central orbital period). Next, plot (b) shows the distribution of the radial component for the same set-up but for a higher number of propagation period (10 central orbital period). For generating plots (c) and (d) we use the same set-up except the starting location is apogee ($T = 180^\circ$).	104

3.8 **Example 3.6., distribution of the inverse radial component, part 2.** This plot is similar to the plot mentioned previously in Fig. 3.7. The only difference is that in this plot inverse of the radial distributions are highlighted. However, both plots (Figs. 3.7 and 3.8) convey the same message. 108

3.9 **Example 3.6., distribution of the *standardized* inverse radial component, part 3.** This plot represents standardized (inverse) radial components. As it can be seen all the radial distances are approximately univariate normal. 109

4.1 **Example 4.1., variance plot, $\xi_2^2 \ll \xi_1^2$.** In this example, total number of observations are 5 and $\xi_2^2 \ll \xi_1^2$. The posterior variance values are displayed in the plot (next to each plot marker) only for the visualization purpose. This plot shows that the rate at which the variances are decaying is $\propto O(1/k)$ 115

4.2 **Example 4.1., variance plot, $\xi_1^2 = \xi_2^2 = 1$.** In this example, total number of observations are 5 (same as before). This plot shows that the rate of change of variance is $\propto O(1/k)$ 116

4.3 **Mapping F_{M-to-T} function when $e = 0.7$.** True anomaly as a function of mean anomaly, for eccentricity $e = 0$ (diagonal straight line) and $e = 0.7$ (curved line). Angles are given in degrees. The points indicated by circles, after projection onto the horizontal axis, give the prior means μ_x^{Kalman} for Examples 4.3. and 4.4. The points indicated by boxes, after projection onto the vertical axis, give the observations z_{obs} , and after projection onto the horizontal axis, give the values of $x_{obs} = h_{Kalman}^{-1}(z_{obs})$, for Examples 4.3. and 4.4. 123

5.1 **Example 5.1., log scaled variance plots.** The log scaled updated AST-CRTN variances vs. time for A1-A6. 131

5.2 **Example 5.1., log scaled absolute difference plots.** The log scaled absolute differences between the true AST-CRTN values and the updated AST-CRTN means vs. time for A1-A6. 132

6.1	Example 6.1., solving the association problem. The association problem for two overlapping distributions 1 and 2. Observations are highlighted using red markers, a total of 4 observations are made.	145
6.2	Example 6.2., solving the association problem for a break-up event. The upper plot is the same (in terms of the propagation period) as panel (b) in Fig. 3.2, with two observations superimposed. The lower plot (with scaled/standardized latitude representing the vertical axis) shows the transformation to bivariate normality. Point A is compatible with this distribution; point B is not.	146
6.3	Example 6.3., solving the association problem for for a mixture of break-up and non break-up events. Two distributions and one single observation where the first object suffers from the pinching problem. The observation is located just outside the pinching zone or the center of the distribution 1. However, the observation is clearly part of the second distribution.	147
6.4	Example 6.4., joint distribution in the Cartesian (CRTN) coordinate system at $t = 0$, part 1. Initial point clouds ($N_A = 2000$ and $N_B = 2000$) for objects 1 and 2 represented in ECI coordinates.	149
6.5	Example 6.4., joint distribution in the Keplerian (CRTN) coordinate system at $t = 0$, part 2. Initial point clouds ($N_A = 2000$ and $N_B = 2000$) for objects 1 and 2 represented in Keplerian coordinates.	150
6.6	Example 6.4., joint distribution in the Equinoctial (CRTN) coordinate system at $t = 0$, part 3. Initial point clouds ($N_A = 2000$ and $N_B = 2000$) for objects 1 and 2 represented in Equinoctial coordinates.	151
6.7	Example 6.4., joint distribution in the AST (CRTN) coordinate system at $t = 0$, part 4. Initial point clouds ($N_A = 2000$ and $N_B = 2000$) for objects 1 and 2 represented in AST coordinates.	152

6.8 **Example 6.4., various filtering stages for ambiguity in custody problem, part 5.** Angles-only representation of the point cloud at $t = 0$. The blue cluster indicates the distribution associated with the first object (object 1) and the green cluster represents the second object (object 2). The red dot is the observation. Subplot (a), at $t = 0$, note the high degree of overlapping between the two distributions. Subplot (b), at $t = 200$ minutes, two distributions are still very much overlapped. Subplot (c), at $t = 400$ minutes, the observation is connected with the first distribution. Subplot (d), at $t = 600$ minutes, clearly the observation can be associated with the first distribution. 153

7.1 **Example 7.1., observer-centric propagation analysis for a LEO object.** In this example, a LEO object is propagated and the propagated angular uncertainties are represented using the observer-centric frame of reference (or observation). The joint distribution is clearly non-normal. 159

7.2 **Example 7.1., observer-centric propagation analysis for a GEO object.** In this example, a GEO object is propagated for 1 central orbital period and the propagated angular uncertainties are represented using the observer-centric frame of reference. The joint distribution is approximately normal. 160

7.3 **Example 7.2., observer-centric propagation analysis for a LEO object with short propagation time.** In this example, we use the same LEO object which we used in Fig. 7.1. However, the propagation period is reduced. In this example the propagation period is 0.1 orbital period (equivalent to 13.1 minutes). Clearly, the joint distribution of the latitude and the longitude is approximately a bivariate normal. 161

7.4	Example 7.3., multivariate sensitivity analysis. Analyzing sensitivity of different multivariate normality tests. In both subplots, the plot at the upper left shows a spherical representation of the point cloud. The remaining plots show histograms (true angles) and a scatter plot for the longitude (unit - degree) and latitude (unit - degree). Note that we use unwrapped longitude in both subplots. The term unwrapped means we are treating the longitude as a number rather than an angle. Notice that both subplots are non-normal. Results are discussed in Table 7.1	163
A.1	Examples to show various values of the RAAN and the argument of Perigee (Not scaled to size). (a) For the first image both the ω and Ω values are $< 180^\circ$ and the direction of motion is anti-clock wise. For the second image $\Omega > 180^\circ$ but $\omega < 180^\circ$ and the direction of motion is clock-wise. (c) For the third image $\omega > 180^\circ$ but $\Omega < 180^\circ$ and the direction of motion is anti-clock wise like the first image.	166
A.2	Propagated Cartesian-ECI coordinates for small-term propagation. All the coordinates are approximately normal.	168
A.3	Keplerian-CRTN coordinates for a near circular orbit at $t = 0$. Most of the elements are non-normal.	169
A.4	AST-CRTN coordinates for a circular orbit at $t = 0$. All the coordinates are approximately normal.	170
A.5	Propagated angles-only position vector for a HEO orbit when the propagation period is large. Notice that the distribution of the unwrapped ϕ is approximately normal. However, unwrapped θ is not normal. Further, look at the scatter plot (1,4), it exactly shows the non-linear pattern which we discussed in the Chapter 5.	171

A.6 **Propagated angles-only position vector for a circular LEO orbit.** Since the perigee is ill-defined for a circular orbit, distributions of the true and mean anomaly are no longer behave as normal. However, notice that both $\phi(t)$ and $\theta(t)$ are approximately normal. The orbit is not exactly circular ($e = 9e^{-05}$) but a near circular orbit and distributions of θ and ϕ are nearly the same. 172

A.7 **True anomaly vs mean anomaly for varying eccentricity values.** Relationship between the true anomaly (T) and the mean anomaly(M) is highlighted in this plot. A total of 10 different eccentricity(e) values are considered. Note that when $e = 0$, both true and mean anomalies are same. 173

A.8 **The true and eccentric anomalies (Not scaled to size).** This plot provides a brief idea on the true and eccentric anomalies. . . 174

B.1 **Euclidean distance vs. Mahalanobis distance.** Of course, x_1 is part of the distribution $D_{\text{bivariate}}$ but x_2 is not. However, the Euclidean distances are same for both the points. 179

Chapter 1

Introduction

1.1 Introduction

Sputnik 1 was launched in 1957. In the last 63 years around 9500 satellites have been launched and based on a report published by the European Space Agency (ESA), more than 128 million space debris are orbiting the earth now and most of them are of size less than 1 mm (ESA, 2020a). Out of these 128 million space objects, only around 23,000 objects are traceable (ESA, 2020a) due to the size limitation. Space debris can arise from anything related to a man-made space mission such as rocket bodies, solar panels, unused thermal blankets of astronauts and much more. Space debris can be extremely dangerous for spacecraft and satellite operations. Due to the high population and large relative velocities of space debris, it is extremely difficult to track them accurately using optical observations and to associate them with past observations. A major challenge is to represent the uncertainty in predicted location and velocity of debris more precisely for tracking and association purposes.

Consider a space object in an elliptical orbit about the earth. If the initial location and velocity, $\mathbf{x}^{\text{ECI}}(0)$ and $\dot{\mathbf{x}}^{\text{ECI}}(0)$ (represented using the Cartesian-ECI coordinate system), are known 3-dimensional vectors at time $t = 0$, then the laws of Newtonian motion can be used to propagate the motion using the Keplerian (without perturbations) or non-Keplerian (with perturbations) dynamics, i.e. to compute $\mathbf{x}^{\text{ECI}}(t)$ and $\dot{\mathbf{x}}^{\text{ECI}}(t)$ for all $t > 0$. If measurements for the position and velocity at an initial time ($t = 0$) are available up to Gaussian noise in the Cartesian

Earth-centered Inertial (ECI) coordinate system, a point cloud is typically used to describe the propagated uncertainty at later times. As the propagation time (t) increases, the shape of the point cloud for position in \mathbb{R}^3 becomes more “banana-shaped” (curved) (Junkins *et al.*, 1996; Kent *et al.*, 2016; Valli *et al.*, 2013) in the Cartesian-ECI coordinate system (see the propagation example in Chapter 2, Fig. 2.3). Similar issues arise for the propagated distribution in other coordinate systems such as the Keplerian-ECI (and Keplerian-CRTN) or the Equinoctial-ECI and such distributions are awkward to work with. In addition, the Keplerian-ECI (and Keplerian-CRTN) and Equinoctial-ECI coordinate systems also have singularities (see propagation examples in Chapters 2 and in the Appendix, Figs. 2.4, 2.5, A.3). Here “CRTN” indicates “central Radial-Tangential-Normal” basis, see Chapter 2 for more details. In this thesis, we mention a coordinate system by combining its name and the reference basis in which it is represented. For instance, the term “Keplerian-CRTN” indicates the Keplerian coordinate system represented using the CRTN basis.

This thesis talks about two new coordinate systems and illustrates their various uses. First, it discusses the “Adapted SStructural (AST)” coordinate system (AST-CRTN) to represent the 6-dimensional orbital state (Chapter 2). The propagated uncertainty represented using the AST-CRTN coordinate system is approximately Gaussian under a wide range of conditions. Second, it discusses the “Adapted SPHERical (ASP)” coordinate system (ASP-CRTN) to represent the uncertainty associated with the 2-dimensional angles-only position of the propagated point cloud (Chapter 3). The term “point cloud” refers to a state and the surrounding uncertainty (“uncertainty cloud”). Further, we also discuss the distribution of the radial component (or the altitude). The ASP-CRTN coordinates along with the radial component can be used to represent the position of an orbiting object in terms of the Cartesian-CRTN coordinate system. Suitable examples are provided to show effectiveness of both the AST-CRTN and ASP-CRTN coordinate systems.

This introductory chapter discusses both the mathematics and the statistics of orbital dynamics. In addition, this chapter also summarizes some of the basic concepts which will help the reader to understand the thesis.

1.2 Thesis contributions

Orbital uncertainty propagation and orbital object tracking are key themes in the Space Situational Awareness (SSA) and a number of papers have been published in recent years to deal with the non-linearity of the system equation when expressed in Cartesian-ECI coordinates. There are two basic strategies to deal with non-linearity: (i) transform the coordinate system to remove the non-linearity, or (ii) develop sophisticated methods to accommodate it. This thesis uses the first approach.

However, many papers have taken the second approach. For example, Park and Scheeres used a mixture (hybrid approach) of a simplified dynamic system (SDS) model and the state transition tensor (STT) model to propagate and model the uncertainty with higher order Taylor series terms (Park & Scheeres, 2018, 2006, 2012). Vittaldev, Russell and Linares (Vittaldev *et al.*, 2016) proposed a mixture of polynomial chaos expansion (PCE) and Gaussian Mixture Models (GMMs) based on Hermite polynomials. Several other papers (Bhusal & Subbarao, 2019; Fenfena *et al.*, 2014) also used the polynomial chaos model (PCM) and PCE for representing the orbital uncertainty.

The space object tracking problem is nonlinear (more details can be found in Chapter 4 and Chapter 5). Standard nonlinear Kalman filters are the Unscented Kalman filter (UKF) and the Extended Kalman filter (EKF). However, these two filters are often unreliable. In order to overcome limitations of these two filters, a number of new filters have been proposed for the space object tracking problem. For instance, Raihan and Chakravorty proposed a hybrid filter (Raihan A & Chakravorty, 2018) by mixing concepts of the UKF and particle filter together. McCabe and DeMars showed the usefulness of a particle filter (McCabe & DeMars, 2014) for the space object tracking purpose. Sigges and Baum discussed the usefulness of the ensemble Kalman filter (EnKF) (Sigges & Baum, 2017) in their paper. However, all these methods can be computationally expensive. The tracking algorithm proposed in this thesis is fast and performance wise similar to a particle filter.

Note that in order to test our proposed coordinate systems under extreme conditions (Chapter 2 and Chapter 3), we consider a high amount of initial uncer-

tainties (both in position and velocity) and show that the propagated point cloud is able to preserve normality under such conditions. However, in reality these error values are huge (at least 50 times higher) compared to the standard values (Hussein *et al.*, 2015; Woodburn & Tanygin, 2014; Yang *et al.*, 2018). In addition, to test various coordinates both two-line-element (TLE) data (*standard*) (Vallado & Cefola, 2012) and computer simulated data are used. Computer simulated data allows us to test our algorithms under a wide range of conditions (such as, circular orbit vs. extremely high elliptical orbit, LEO vs. GEO etc.) compared to the TLE data. Our proposed methods and algorithms turn out to be widely applicable and can deal effectively with a wide variety of initial conditions that can cause problems for other methods, including (a) long propagation times, (b) high eccentricity, (c) large initial uncertainties and (d) specialized situations such as break-up events.

My key contributions related to this project are listed below.

- (a) Standard astrodynamics coordinate systems are often non-Gaussian under propagation; to address this issue a *local* “Adapted SStructural (AST)” coordinate system (AST-CRTN) is developed in which the uncertainty is represented in terms of deviations from the “central state” (provided that we have information about the state and the associated uncertainty at time $t = 0$). In this coordinate system initial Gaussian uncertainty remains Gaussian for all propagation times under Keplerian dynamics. A number of statistical tests have been carried out to confirm the quality of Gaussian approximation. The “central state” does not need to be the mean but locates near the center of the uncertainty point cloud for the AST-CRTN coordinate system at $t = 0$.
- (b) The problem of object tracking can be viewed as an example of Bayesian filtering (Chen, 2003). Examples of such filters include the classic Kalman filter (Bhaumik & Paresh, 2019; Hongbin *et al.*, 2020; Youngjoo & Hyochoong, 2018), together with non-linear variants such as the extended (Bhaumik & Paresh, 2019) and unscented Kalman filters (Julier, 2002; Julier & Uhlmann, 2004; Wan & Merwe, 2000), and computationally more expensive particle

filters (Chen, 2003; Gustafsson *et al.*, 2002). The unscented (UKF) or extended (EKF) Kalman filters are (sometimes) unable to approximate the posterior mean and the variance accurately (Havlík & Straka, 2015; Zhan & Wan, 2007). The iterated (“I”) Kalman filters such as the IEKF (Kent *et al.*, 2019a) and IUKF (Kent *et al.*, 2019a) often perform well. Two new “Observation-Centred Kalman filters (OCKF)” have been developed (Kent *et al.*, 2019a,b). Performance wise the OCKF, IEKF, OCUKF and IUKF are similar (Kent *et al.*, 2019a,b) for the orbital tracking examples mentioned in this thesis (Chapters 4 and 5). However, one advantage of the Observation-Centred filters over the IEKF/IUKF is that they do not require iteration.

- (c) The AST-CRTN coordinate system along with the OCKF (or with the IEKF/IUKF) can be used to treat ambiguity or the filtering-association problem. The term “ambiguity” refers to a situation when the object custody is ambiguous. Ambiguity in custody occurs when an angles-only observation at a particular time say $t = 0$, can be associated with the states for two or more objects in a catalog or library (see Chapter 6, Section. 6.8.4).
- (d) The AST-CRTN coordinate system represents the 6-dimensional orbital uncertainty. Another coordinate system is developed to represent the 2-dimensional uncertainty associated with the angles-only part of the propagated point cloud and the name of the newly developed coordinate system is the “Adapted SPherical (ASP)” coordinate system (ASP-CRTN). Note that both the AST-CRTN and ASP-CRTN coordinate systems represent the propagated uncertainty associated with the state vector but in two different forms. The AST-CRTN coordinate system represents the 6-dimensional orbital state vector but the ASP-CRTN coordinate system deals with the 2 or 3-dimensional position vector. In addition, the ASP-CRTN coordinate system can be constructed from the AST-CRTN coordinate system but the opposite cannot be done. However, both the AST-CRTN and ASP-CRTN are of use in filtering, the first to represent the state and the second to link the state to the observation.

- (e) One of the major concerns with representing the orbital uncertainty in a two-dimensional coordinate system is that if the uncertainty associated with the position of the object is 0 (or extremely small compared to the velocity uncertainty) at time $t = 0$ (such as during a break-up event where the initial position is known nearly exactly), then the propagated point cloud often displays a “bow-tie” or “pinching” pattern in the ASP-CRTN coordinate system. Such a distribution cannot be approximated using a multivariate normal distribution. A new distribution, named the “Pinched-Normal (PN)” distribution has been developed to investigate this issue. Further, we assess the approximate pinching duration using “*velocity-only sigma points*”. Here, the term “sigma points” indicates points generated using weighted standard deviations (or “ σ ”) and provide a discrete approximation to a distribution. Further details can be found in Chapter 3.

1.3 Two uses of the word Keplerian

In this thesis, we use the term “Keplerian” for mainly two different purposes, (i) Keplerian coordinate systems (Keplerian-ECI coordinate system and Keplerian-CRTN coordinate system) and (ii) Keplerian dynamics. The Keplerian coordinate system is made of six orbital elements and they are used to represent the state of an orbiting object at time t . Further information on the Keplerian coordinate system can be found in Subsection 1.7.6.2. The term Keplerian dynamics indicates a situation when we do not incorporate any perturbation forces in our system. On the other hand, the term *non-Keplerian dynamics* means when we consider various deterministic (such as the oblateness of the earth, solar radiation pressure, atmospheric drag etc.) (Roy, 2004) and non-deterministic perturbations. We perform all our analyses using *Keplerian dynamics* in this thesis.

1.4 Organization of the thesis

Much of the thesis is based on work that has appeared in a series of conference papers. However, the underlying unity of the ideas has only become fully apparent

when combining the material together. More details are listed below for each chapter.

- (a) **Chapter 1** is the current chapter and also works as an introductory chapter. Apart from discussing my key contributions, this chapter also illustrates various coordinate systems. Parts of this chapter are taken directly or indirectly from my some of my papers ([Kent *et al.*, 2019a,b](#)).
- (b) **Chapter 2** introduces the AST-CRTN coordinate system. Further, this chapter lists a number of statistical tests which confirm the approximate Gaussian behavior in the AST-CRTN coordinate system. Parts of this chapter are taken directly or indirectly from some of my papers ([Bhattacharjee *et al.*, 2019b](#); [Kent *et al.*, 2019b](#)). Note that several other versions of the AST-CRTN coordinate system have been proposed and developed in various conference papers ([Bhattacharjee *et al.*, 2017a,b, 2018a,b,c](#); [Kent *et al.*, 2017b, 2018a,c](#)) but the version mentioned in this chapter is the most upgraded version.
- (c) **Chapter 3** discusses the uncertainty associated with the propagated angles-only position. This chapter introduces the ASP-CRTN coordinate system. Further, this chapter also discusses the distribution of the propagated radial component. Parts of this chapter are taken directly or indirectly from one of my papers ([Bhattacharjee *et al.*, 2019a](#)). Note that we mentioned about the ASP-CRTN coordinate system in some of our previous papers ([Bhattacharjee *et al.*, 2017a, 2018b](#); [Kent *et al.*, 2017a,c, 2018b](#)).
- (d) **Chapter 4** introduces the filtering problem and highlights limitations of the UKF and EKF, it also discusses benefits of using the IUKF, IEKF, OCUKF and OCEKF using suitable 1-dimensional examples. The main purpose behind developing the AST-CRTN coordinate system is to facilitate the filtering problem. Recall the previous section, the UKF, EKF, IUKF, IEKF, OCUKF and OCEKF stand for the unscented Kalman filter, the extended Kalman filter, the iterated unscented Kalman filter, the iterated extended Kalman filter, the observation-centered unscented Kalman filter

1.5 Outline of the rest of this chapter (Key contributions)

and the observation-centred extended Kalman filter. Parts of this chapter are taken directly or indirectly from two of my papers ([Kent *et al.*, 2019a,b](#)).

- (e) **Chapter 5** discusses the 6-dimensional filtering problem. First, we illustrate the usefulness of the AST-CRTN coordinate system by discussing the AST-IUKF algorithm. Next, we discuss the OCKF algorithm for tackling the 6-dimensional orbital tracking problem. Parts of this chapter are taken directly or indirectly from two of my papers ([Kent *et al.*, 2019a,b](#)).
- (f) **Chapter 6** highlights how the ASP-CRTN coordinate system with/without some modifications can be used for handling various association problems. In addition, this chapter also discusses the filtering-association problem using a suitable example. Parts of this chapter are taken directly or indirectly from one of my papers ([Bhattacharjee *et al.*, 2019a](#)).
- (g) **Chapter 7** lists related and future work. In addition, this chapter also discusses key conclusions.
- (h) **The Appendix** is divided into four subparts. The first part provides further details on orbital dynamics. The second part explains various statistical concepts. The third part lists orbital parameters for various orbiting objects that are used throughout the thesis to illustrate key ideas. The final portion lists my papers.

1.5 Outline of the rest of this chapter (Key contributions)

The key contributions (related to this chapter) are summarized below.

- (1) First, we discuss the mathematics of orbital dynamics. This section contains information related to the representation of an orbit in 2-dimensional and 3-dimensional planes, various angles associated with orbital dynamics, equations of orbital motion, classification of various orbits and different coordinate systems (Section [1.7](#)).

- (2) Second, we mention the statistics of orbital dynamics. This section illustrates the uncertainty representation model. In addition, this section also talks about the statistical analysis of propagated distributions (Section 1.8).
- (3) Third, we provide one example (Example 1.1.) to highlight limitations of standard coordinate systems. The example, which is discussed in this section, is not related to astrodynamics but the purpose of this example is to introduce the problem through a known coordinate system (Section 1.9).
- (4) Fourth, we discuss the tracking and association problems (Sections 1.10 and 1.11).
- (5) Finally, we provide a brief summary of this thesis and illustrate key contributions (Section 1.12).

1.6 Relation to other chapters

This chapter introduces various orbital elements to the reader. In addition, this chapter also discusses standard astrodynamics coordinate systems. The next chapter shows why these coordinate systems are unreliable for statistical analysis using suitable propagation examples (Section 2.5.3). The AST-CRTN coordinate system, mentioned in the Chapter 2, has been developed to deal with the limitations of the standard coordinate systems. Besides, this chapter briefly discusses the association problem. The association problem is investigated in detail in Chapter 6.

1.7 Mathematics of orbital dynamics

This section discusses various orbital elements, representation of an orbit in both 2-dimensional and 3-dimensional planes and various astrodynamics coordinate systems.

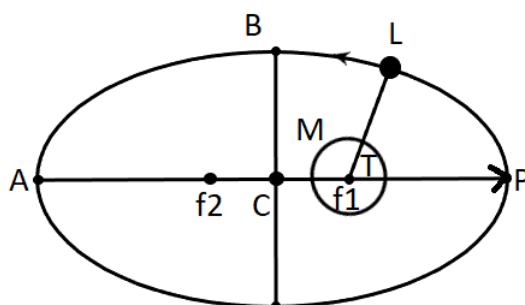


Figure 1.1: **Representing an orbit in 2 dimensions (Not scaled to size).** Various orbital elements in a 2-dimensional orbital plane are shown in this image. Note that only the true anomaly (T) and the radial distance (distance between point f_1 to point L) change with time. The perigee and apogee are indicated by points P and A respectively.

1.7.1 Orbital dynamics in 2 dimensions

An object orbiting the earth follows an exact elliptical orbit under Keplerian dynamics, with the center of the earth at one of the focal points of the ellipse. Fig. 1.1 represents an orbiting object and the orbit (ellipse). In this image f_1 , f_2 and C indicate two focal (or foci) points and the center of the ellipse respectively. Further, points P and A denote the perigee and the apogee respectively and the direction of motion is anti-clockwise. The distance between the rotating object and the earth is the smallest at the perigee and largest at the apogee. The distance between point C to point P (same as the distance between point A to point C) is called the length of the major axis (a) whereas the distance between point C to point B is the length of the minor axis (b). The relationship between the major axis (a) and minor axis (b) can be mathematically written as,

$$b = a\sqrt{(1 - e^2)},$$

where, e is the eccentricity. Note that $e = 0$, $0 < e < 1$ (Fig. 1.1), $e = 1$, $e > 1$ denote circle, ellipse, parabola, hyperbola (Curtis, 2006; Roy, 2004) respectively. For a circular orbit ($e = 0$) f_1 , f_2 and C will be one single point.

The angular position ($\angle Pf_1L$) is shown using the letter T and the distance between point f_1 to point L is called the radial distance (r).

Recall Kepler's first law (Planets are rotating around the sun in an elliptical orbit and the sun is located at one of the two focal points), in our case, the "sun" and "planet" are replaced by the "earth" and "satellite/debris" respectively. In Fig. 1.1, point M (located at the foci f_1) is the main body (earth) and the rotating object (satellite or debris) is located at the point L.

Finally, using the representation mentioned in this subsection, only the angular position and the radial distance change with time.

An orbit in the 2-dimensional plane can be represented using following elements,

- (1) **Size of the orbit, 2 elements:** Length of the major axis (a) and eccentricity (e).
- (2) **Location of the moving object, 2 elements:** Angular displacement ($T(t)$, equivalent to the true anomaly measured from the perigee) and radial distance ($r(t)$)

The concept of the true anomaly is mentioned in the next subsection. However, before describing the orbital dynamics in 3 dimensions, several related concepts are mentioned. These information (related to various orbital elements) will help the reader to understand the Section 1.7.4.

1.7.2 Three angles in orbital dynamics

There are three angles of mathematical interest in orbital dynamics setting to describe the angular position of the object along its orbit are (see Fig. 1.2): the *eccentric anomaly* ($E(t)$)($\angle PCL2$), the *mean anomaly* ($M(t)$)($\angle PCL1$) and the *true anomaly* ($T(t)$)($\angle Pf_1L$), where all three angles are measured from the perigee (Point P in Fig. 1.2). The true anomaly describes the actual angular position of the object, as measured from the center of the earth (Point f_1 in Fig. 1.2). The mean anomaly simplifies the mathematical development because it changes at a constant rate in time, and the eccentric anomaly is an intermediate angle of no direct interest.

The relation between the angles is given as follows (Curtis, 2006; Roy, 2004), where e is the ellipticity, $0 \leq e < 1$ (for this thesis):

$$\tan \frac{1}{2}T = \sqrt{\frac{1+e}{1-e}} \tan \frac{1}{2}E, \quad (1.1)$$

$$M = E - e \sin E, \quad (1.2)$$

$$\tan E = \frac{\sqrt{1-e^2} \sin T}{e + \cos T}. \quad (1.3)$$

The calculations are all straightforward, except that a numerical iteration is needed to solve for E from M . Equation (1.2) is also called the Kepler's equation and has no *closed-form* solution for E given M and can only be solved using Newton-Raphson method (Roy, 2004).

All three angles are defined on the same interval $-\pi < E, M, T \leq \pi$. These three angles agree at the midpoint (apogee) and endpoints (perigee). That is, if $E = 0, \pi$ or $-\pi$, then M and T also equal to $0, \pi$ or $-\pi$, respectively. Further the identification between angles is symmetric about the origin. That is, if E corresponds to M and T , then $-E$ corresponds to $-M$ and $-T$. Finally, by periodic extension, the mapping between the three angles can be extended to any interval $-\pi + 2\pi k \leq E, M, T \leq \pi + 2\pi k$, $k \in \mathbb{Z}$.

The notation $E = F_{M\text{-to-}E}(M, e)$ is used to describe the transformation between M and E and similar notation for the transformations between other pairs of angles. Fig. 1.2 shows all three anomalies in one picture and Fig. A.8 visually illustrates the true and eccentric anomalies for further clarification.

1.7.3 Equations of orbital motion in 3 dimensions

Consider the *state* of an object orbiting the earth. The state at time t can be described in Cartesian-ECI coordinates by three-dimensional position and three-dimensional velocity vectors $\mathbf{x}^{\text{ECI}}(t)$, $\dot{\mathbf{x}}^{\text{ECI}}(t)$. Note that as the name suggests, for this coordinate system the origin is located at the center of mass of the earth (Vallado, 2001; Wikipedia contributors, 2019). Further, the term inertial indicates this coordinate system remains unaffected by the rotation of earth and various other acceleration forces.

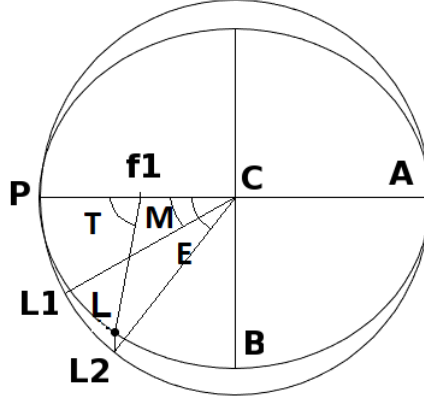


Figure 1.2: **The true, mean and eccentric anomalies (Not scaled to size).** The true, mean and eccentric anomalies are highlighted in this image. The true anomaly is measured with respect to the actual location of the object (in the ellipse). The object is located at the point L. Also see image [A.8](#).

In this thesis the term “ECI” includes three ideas: an inertial representation of objects around the earth, location of the observer (“centered”) and the idea of a specific basis. Later, AST coordinates (Chapter 2) will still use an inertial representation (the location of the observer/origin is still at the center of the earth), but with a different basis (the CRTN basis).

The state at the initial time ($t = 0$) determines the state at all other times as the object follows an elliptical orbit. Various features ([Curtis, 2006](#); [Roy, 2004](#)) can be extracted from the state to help describe this elliptical orbit (see Fig. [1.3](#)). Here μ is the gravitational constant for the earth.

- (a) In general, a *frame* is a basis of orthonormal vectors in \mathbb{R}^3 . In the current setting, a useful frame is the *RTN* (*radial-tangential-normal*) frame at an initial time $t = 0$, defined as follows ([Vallado, 2001](#)):

$$\mathbf{u} = \mathbf{u}^{\text{RTN}} \propto \mathbf{x}^{\text{ECI}}(0), \quad (1.4)$$

$$\mathbf{v} = \mathbf{v}^{\text{RTN}} \propto \dot{\mathbf{x}}^{\text{ECI}}(0) - \{\dot{\mathbf{x}}^{\text{ECI}}(0)^T \mathbf{u}\} \mathbf{u}, \quad (1.5)$$

$$\mathbf{w} = \mathbf{w}^{\text{RTN}} = \mathbf{u} \times \mathbf{v} \propto \mathbf{x}^{\text{ECI}}(0) \times \dot{\mathbf{x}}^{\text{ECI}}(0), \quad (1.6)$$

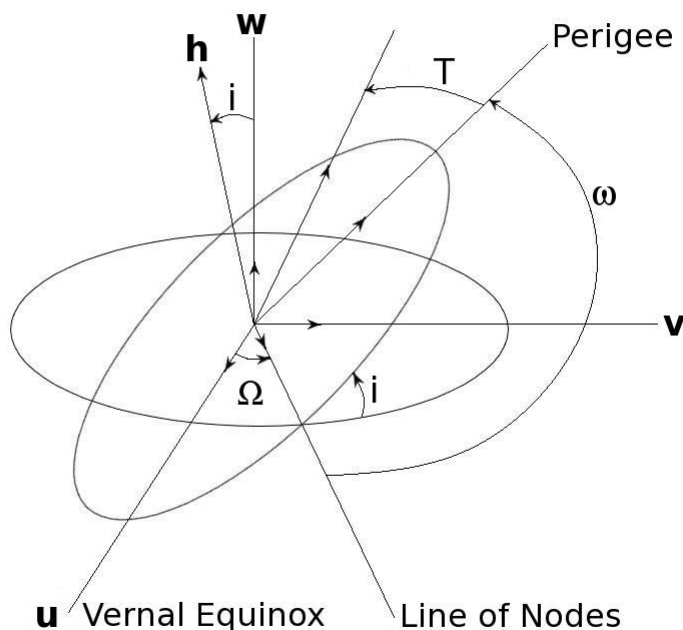


Figure 1.3: **Orbital dynamics in three dimensions (Not scaled to size)**. An orbiting object in Keplerian dynamics. The plot shows the reference and orbital planes together with their preferred directions and normal directions. The angles ω , Ω , i and $T(t)$ are highlighted.

so that \mathbf{u} points in the radial direction, \mathbf{v} points in the tangential direction (after orthogonalizing with respect to the radial direction) and \mathbf{w} is normal to the $\mathbf{u} - \mathbf{v}$ plane.

Next, we discuss how to compute various orbital elements. Note that we use $\mathbf{x}(0)$ and $\dot{\mathbf{x}}(0)$ (rather than $\mathbf{x}^{\text{ECI}}(0)$ and $\dot{\mathbf{x}}^{\text{ECI}}(0)$ or $\mathbf{x}^{\text{CRTN}}(0)$ and $\dot{\mathbf{x}}^{\text{CRTN}}(0)$) to represent the state of an orbiting object as the choice of basis does not change these formulas but change values of various orbital angles (such as, the inclination angle).

(b) The *angular momentum vector* is given by

$$\mathbf{h} = \mathbf{x}(0) \times \dot{\mathbf{x}}(0). \quad (1.7)$$

1.7 Mathematics of orbital dynamics

Its magnitude $h = |\mathbf{h}|$ is called the *angular momentum*.

(c) The *eccentricity vector* is given by

$$\mathbf{e} = \frac{1}{\mu}(\dot{\mathbf{x}}(0) \times \mathbf{h}) - \mathbf{u}. \quad (1.8)$$

Its magnitude $e = |\mathbf{e}|$ is called the *eccentricity*.

(d) The (*semi-major axis*) of the ellipse is given by

$$a = \frac{h^2/\mu}{1 - e^2}, \quad (1.9)$$

(e) The *period* ($\square p$) and the *mean motion* (n) are

$$\square p = 2\pi\sqrt{a^3/\mu}, \quad n = 2\pi/\square p = \sqrt{\mu/a^3}. \quad (1.10)$$

(f) The *inclination angle* is given by

$$i = \cos^{-1} \frac{h_z}{h}. \quad (1.11)$$

(g) The *node vector* (also defines the node line) and its magnitudes are,

$$\mathbf{N}_{\text{RAAN}} = \mathbf{w} \times \mathbf{h}, \quad N_{\text{RAAN}} = \sqrt{\mathbf{N}_{\text{RAAN}} \cdot \mathbf{N}_{\text{RAAN}}}. \quad (1.12)$$

Further, the node vector lies on the intersection of the orbital and reference planes.

(h) The *Right Ascension of the Ascending Node (RAAN)* angle is computed as,

$$\Omega = \cos^{-1} \frac{N_x}{N_{\text{RAAN}}}. \quad (1.13)$$

Note. $N_x = \mathbf{N}_{\text{RAAN}}(1)$.

(i) The *argument of perigee* is,

$$\omega = \cos^{-1} \frac{\mathbf{N}_{\text{RAAN}} \cdot \mathbf{e}}{N_{\text{RAAN}}e}. \quad (1.14)$$

(j) The *true anomaly (from the perigee)* is,

$$T = \cos^{-1} \frac{\mathbf{e} \cdot \mathbf{x}}{ex}. \quad (1.15)$$

Note that Ω and ω and T lie in $[0,360)$, Ω is an angle in the reference plane and ω and T are angles in the orbital plane. Subsections 1.7.6.1 and 1.7.6.2 provide more information on the reference plane and the orbital plane.

(k) Finally, the *direction of perigee* (in the RTN basis) is given by

$$\theta_p = \text{atan2}(\mathbf{e}^T \mathbf{v}, \mathbf{e}^T \mathbf{u}) \quad (1.16)$$

and defines the angle in the $\mathbf{u} - \mathbf{v}$ plane at which the orbiting object is closest to the earth. Here atan2 is the two-argument arctan function found in many computing languages. For example, $\theta_p = 0$ points towards the positive \mathbf{u} axis and $\theta_p = \pi/2$ points towards the positive \mathbf{v} axis.

The ellipticity vector lies in the $\mathbf{u} - \mathbf{v}$ plane and can be written in the form

$$\mathbf{e} = f_1 \mathbf{u} + f_2 \mathbf{v}, \quad (1.17)$$

where $f_1 = e \cos \theta_p$ and $f_2 = e \sin \theta_p$.

These pieces of information can be used to describe the evolution of an orbiting object in time under Keplerian dynamics. Of course the frame $\mathbf{u}, \mathbf{v}, \mathbf{w}$ is defined at time $t = 0$ and so does not change with time. In addition, the features f_1, f_2, n , and hence also h, e, n, θ_p are also constant in time.

(l) The state equation of the orbiting object can be expressed as

$$\mathbf{x}(t) = r(t) \{ \cos \theta(t) \mathbf{u} + \sin \theta(t) \mathbf{v} \}, \quad (1.18)$$

in terms of a radial function $r(t)$ and an angular function $\theta(t)$ (Curtis, 2006;

Vallado, 2001), where

$$\begin{aligned}
 r(t) &= \frac{(h^2/\mu)}{1 + e \cos T(t)} \\
 &= \frac{(h^2/\mu)}{1 + e \cos(\theta(t) - \theta_p)} \\
 &= \frac{(h^2/\mu)}{1 + f_1 \cos \theta(t) + f_2 \sin \theta(t)} \tag{1.19}
 \end{aligned}$$

$$\theta(t) = \theta_p + T(t), \quad T(t) = F_{\text{M-to-T}}(M(t), e), \tag{1.20}$$

$$\begin{aligned}
 \phi(t) &= \phi_p + F_{\text{T-to-M}}(\theta(0) - \theta_p, e) + nt \\
 &= \phi(0) + nt. \tag{1.21}
 \end{aligned}$$

Here $T(t)$ and $M(t)$ denote the usual (measured from the perigee) true anomaly and the mean anomaly, with the relation between them is expressed using a function $M(t) = F_{\text{T-to-M}}(T(t), e)$ and its inverse $T(t) = F_{\text{M-to-T}}(M(t), e)$ (also see Subsection 1.7.2).

Equation (1.21) shows that on the mean anomaly scale the angular speed n is constant. However, non-linear mappings, centered at the direction of perigee, are needed to move back and forth between the mean anomaly and true anomaly scales (Equation (1.20)).

Here $\phi(t)$ denotes the propagated angle on the mean anomaly scale, and $\theta(t)$ denotes the propagated angle on the true anomaly scale, initialized so that $\phi(0) = \theta(0) = 0$. Similarly, $\phi_p = F_{\text{T-to-M}}(\theta_p, e)$ denotes the direction of perigee on the mean anomaly scale where θ_p denotes the corresponding value on the true anomaly scale. Fig. A.7 shows the relationship between the true anomaly and the mean anomaly for varying eccentricity values.

This section has provided a quick details on various orbital elements. Note that Appendix A (Section A.1) provides some extra information on orbital dynamics and orbital elements (some of the elements are already discussed in this subsection).

Note on the naming convention. In this thesis we typically use superscripts (c) and (d) to represent the “central state” (such as, $\mathbf{x}^{(c)}$) and a “deviated state” (such as, $\mathbf{x}^{(d)}$) (deviated state indicates a point/state to represent

the uncertainty of a specific location or a state in the uncertainty point cloud) respectively. However, in some cases we don't use any superscript (such as, \mathbf{x}) and it means that we indicate both the central and deviated states.

1.7.4 Orbital dynamics in 3 dimensions

Subsections 1.7.1 and 1.7.3 have discussed orbital dynamics in 2-d and orbital equations respectively. This section summarizes orbital elements in a 3-dimensional plane. Note that these six unique elements determine the state of an object at time t . These elements are also called “Keplerian orbital elements” (see Subsection 1.7.6.2 for more details).

- (1) **Size of the orbit, 2 elements:** Length of the major axis (a) and eccentricity (e).
- (2) **Orientation of the orbit, 3 elements:** Inclination angle (i), RAAN (Ω) and argument of perigee (ω).
- (3) **Location of the moving object, 1 element:** True anomaly measured from the perigee (T).

Fig. 1.3 shows various orbital elements represented in a 3-dimensional plane.

Note that the 2-dimensional representation of an orbit is the simplest way to represent an orbit and such a representation does not contain information related to the reference plane or the orientation of the orbit. One key assumption associated with this representation (2-dimensional) is that the orbital plane and the reference plane are same (or superimposed). Subsections 1.7.6 discusses more on the orbital plane, reference plane and 3-dimensional representation of an orbit.

1.7.5 Classification of various orbits

An orbit of a satellite is mainly classified using 3 parameters.

- (1) **Altitude/radial distance, $r(t)$:** Based on the altitude, an orbit can be classified into three different categories, namely, a) Low Earth Orbit (LEO, altitude 200 km to 2000 km), b) Medium Earth Orbit (MEO, altitude 2000 km to 35000 km) and, c) Geosynchronous Equatorial Orbit (GEO, altitude

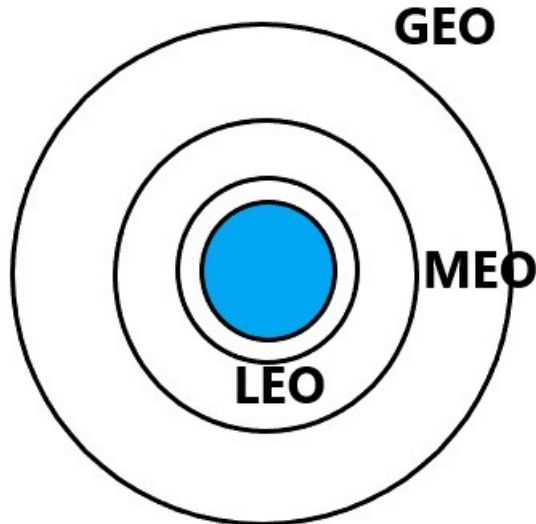


Figure 1.4: **Classification based on the altitude (Not scaled to size)**. LEO, MEO and GEO. Note that this image is only for visual illustration, no scaling is applied here.

≥ 35000 km) (Curtis, 2006; ESA, 2020b; Wikipedia contributors, 2020c). Note that an object located at the LEO, MEO or GEO orbit typically has low eccentricity. See Fig. 1.4 for visual illustration.

- (2) **Eccentricity, e** : For an artificial satellite or space debris the eccentricity (e) lies between 0 and 1 (i.e. $0 \leq e < 1$). As mentioned previously, an orbit with $e = 0$ is called circular orbit and for such orbits the length of the major axis is always same as the length of the minor axis. On the other hand, an orbit with high eccentricity (generally $e \geq 0.3$) is called “Highly Eccentric Orbit (HEO)”. Note that GEO are generally circular ($e = 0$) or near circular orbits and the radial distance or altitude remains always (almost) fixed (Curtis, 2006; ESA, 2020b; Wikipedia contributors, 2020c).
- (3) **Inclination angle, i** : The inclination angle $i \in [0^\circ, 180^\circ]$. An Orbit with inclination angle $\leq 90^\circ$ is called prograde orbit and an orbit with inclination angle $> 90^\circ$ but $\leq 180^\circ$ is called retrograde orbit. See Fig. 1.5 for visual

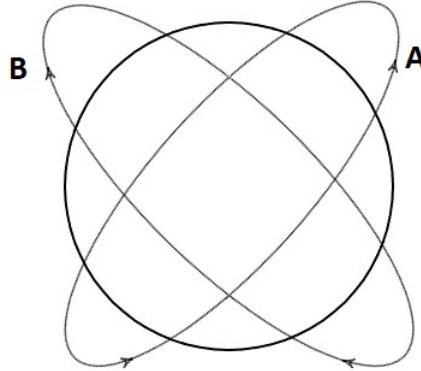


Figure 1.5: **Classification based on the inclination (Not scaled to size).** A is a prograde orbit and B is a retrograde orbit.

illustration. An orbit with inclination angle $i = 90^\circ$ is called a polar orbit (Curtis, 2006; ESA, 2020b; Wikipedia contributors, 2020c).

1.7.6 Introduction to the standard coordinate systems

Various astrodynamics coordinate systems are briefly introduced in this section. These coordinates are defined with respect to a specific basis (such as ECI or CRTN basis), see Section 1.7.7 for more details.

1.7.6.1 Cartesian coordinate system

The Cartesian coordinate system is the simplest coordinate system to represent the state of an orbiting object and consists of 6 elements where the first 3 elements (namely, $x_1(t)$, $x_2(t)$, $x_3(t)$) represent the position ($\mathbf{x}(t)$) of an object in the sky and the last three elements (namely, $\dot{x}_1(t)$, $\dot{x}_2(t)$, $\dot{x}_3(t)$) represent the velocity ($\dot{\mathbf{x}}(t)$) of the object. These are Cartesian coordinates with respect to a *reference basis* where,

$$\mathbf{u} = \begin{bmatrix} 1 \\ 0 \\ 0 \end{bmatrix}, \quad \mathbf{v} = \begin{bmatrix} 0 \\ 1 \\ 0 \end{bmatrix}, \quad \mathbf{w} = \begin{bmatrix} 0 \\ 0 \\ 1 \end{bmatrix}, \quad (1.22)$$

where \mathbf{u} and \mathbf{v} define the *reference plane* (also called the “equatorial” plane). In this plane a *preferred reference direction* is given by \mathbf{u} and angles in the reference plane can be measured counter-clockwise (i.e. moving from \mathbf{u} to \mathbf{v}) from the preferred reference direction. Similarly, \mathbf{w} can be termed the *normal reference direction*.

In many ways Cartesian (both the Cartesian-ECI and Cartesian-CRTN) coordinates are the easiest coordinates to work with, but they have two main drawbacks. First, the propagation equations are non-linear, leading to non-Gaussian distributions under propagation (see Section 2.5.3). Secondly, the Cartesian-ECI coordinate system does not use orbital elements (mentioned in the Section 1.7.3) directly.

Time varying elements: Using Keplerian dynamics, under propagation all six Cartesian-ECI elements change with time.

1.7.6.2 Keplerian coordinate system

The Keplerian elements use orbital elements directly. Conventionally, the *standard reference basis* (ECI reference basis) from (1.22) is used for the definition of Keplerian-ECI elements.

The *orbital plane* is the second plane and it represents the orbit of the rotating object (the *reference plane* is the first plane). If the orbital inclination is zero then the orbital plane and the reference plane (or the equatorial plane) are exactly same. Within the orbital plane, a *preferred orbital direction* can be defined by the direction of perigee, and angles in the orbital plane can be measured counter-clockwise (i.e. in the direction of orbital motion) from the preferred orbital direction.

The Keplerian elements for a state $(\mathbf{x}(t), \dot{\mathbf{x}}(t))$, defined with respect to the specified reference basis, are given as follows (Curtis, 2006; Shin *et al.*, 2015; Vallado, 2001):

- e , the eccentricity, $0 \leq e < 1$.
- i , the inclination of the orbital plane with respect to the reference plane.
- $T(t)$, the true anomaly (an angle in the orbital plane).

- $\Omega \in [0, 360^\circ)$, the angle in the reference plane from the preferred reference direction (vernal equinox) to the RAAN direction.
- $\omega \in [0, 360^\circ)$, the angle in the orbital plane from the RAAN direction to the preferred orbital direction.
- a , the major semi-axis, $a > 0$.

Three of these elements, i, Ω, ω , depend on the choice of reference plane. The Keplerian coordinate system has drawbacks for statistical analysis because it has two singularities. First, if the orbital plane is equatorial then the RAAN angle becomes undetermined. Second, if the orbit is circular ($e = 0$) then the argument of perigee is ill-defined. In addition, the inclination angle (i) and eccentricity (e) suffer from the bounded range problem (see Section 1.9 for more details on the bounded range problem, Fig. A.3 shows the propagated Keplerian coordinates when both the initial eccentricity and inclination angle are 0).

Time varying elements: Using Keplerian dynamics, under propagation only the true anomaly ($T(t)$) changes with time.

1.7.6.3 Equinoctial coordinate system

The problems of Keplerian elements are partly resolved by using the Equinoctial coordinate system (Cefola, 1972; Roy, 2004), *Equinoctial elements*, denoted E_1, \dots, E_6 and defined as follows (with respect to the same standard reference basis that is used conventionally for Keplerian elements):

$$\begin{aligned} E_1 &= 2 \tan(i/2) \cos(\Omega), & E_2 &= 2 \tan(i/2) \sin(\Omega), & E_3(t) &= \Omega + \omega + T(t), \\ E_4 &= e \cos(\Omega + \omega), & E_5 &= e \sin(\Omega + \omega), & E_6 &= a. \end{aligned} \quad (1.23)$$

Even though Ω and/or ω may be undetermined in certain circumstances, the Equinoctial elements remain well-defined except for a retrograde equatorial orbit ($i = 180^\circ$) where Equinoctial coordinates break down (see Section 2.5.3).

Time varying elements: As indicated in the notation, all the coordinates are fixed in time except the third (under Keplerian dynamics). The third coordinate $E_3(t)$ can be termed as the *remapped angular position* or *break angle*, since these three angles (Ω, ω and $T(t)$) are located at two different planes.

1.7.7 Different coordinate systems and reference frames

The last three subsections discussed various astrodynamics coordinate systems. In general this thesis discusses three key concepts related to a coordinate system and they are listed below.

- (a) Location of the observer/origin - Earth-centered rather than the sun-centered or observer centered. Although a brief discussion on the observer centered reference frame is provided in the Chapter 7.
- (b) Basis - The ECI basis or the CRTN basis.
- (c) Coordinate System - Either 6 dimensional or 2 (or 3) dimensional. Choices include,
 - (c.1) 6 dimensional - The Cartesian, Keplerian, Equinoctial and AST coordinate systems.
 - (c.2) 2 dimensional - The spherical and ASP coordinate systems. Typically these two coordinate systems are two dimensional but 3 dimensional if the radial component is added.

As mentioned before, this thesis identifies a coordinate system by its name and a basis. Table 1.1 provides a brief summary on various coordinate systems and basis.

Table 1.1: Coordinate systems and reference bases

Coordinate system/basis	ECI	CRTN
Cartesian	Cartesian-ECI (or classic Cartesian)	Cartesian-CRTN
Keplerian	Keplerian-ECI (or classic Keplerian)	Keplerian-CRTN
Equinoctial	Equinoctial-ECI (or classic Equinoctial)	AST-CRTN ⁽¹⁾
Spherical	Spherical-ECI (or classic Spherical)	ASP-CRTN ⁽²⁾

¹ Equinoctial-CRTN is essentially the same as AST-CRTN (with some minor modifications).

² Spherical-CRTN is essentially the same as ASP-CRTN.

Note that spherical coordinates only define the angles-only part of the position vector and so are only two-dimensional (3-dimensional if the radial part is included).

Remarks

- (1) The Cartesian-CRTN, Keplerian-CRTN and Equinoctial-CRTN are special versions of the Cartesian-ECI, Keplerian-ECI and Equinoctial-ECI coordinate systems respectively. Further details on these three coordinate systems are given below.
 - (a) All six Cartesian-CRTN coordinates change with time (similar to the Cartesian-ECI) and the propagated joint distribution becomes non-normal after a moderate term propagation.
 - (b) For the Keplerian-CRTN coordinate system, only the true anomaly ($T(t)$) changes with time (similar to the Keplerian-ECI). However, due to the construction the inclination angle suffers from the bounded range problem.
 - (c) For the Equinoctial-CRTN coordinate system, only $E_3(t)$ changes with time (similar to the Equinoctial-ECI). However, due to the construction Equinoctial-CRTN coordinate system is always prograde.
- (2) The AST-CRTN coordinate system is the *local* version of the Equinoctial-ECI coordinate system and improved version (in terms of statistical analysis) of the Equinoctial-CRTN coordinate system. Only one AST coordinate element ($A_3(t)$) changes with time (more details can be found in Chapter 2).
- (3) The ASP-CRTN coordinate system is the *local* version of the spherical coordinate system (i.e., spherical coordinate system represented using the CRTN basis). Under Keplerian dynamics, both the ASP-CRTN elements change with time, more details can be found in Chapter 3.

1.8 Statistical variability in orbital dynamics

The previous section has discussed the mathematics of orbital dynamics and this section will discuss the statistics of orbital dynamics.

1.8.1 Representing the orbital uncertainty

Imagine a point cloud of deviated states about a central state. Next, find a 3×3 rotation matrix (say, $\mathbf{G}^{(c)}$) which rotates the coordinate system so that the central orbital plane is horizontal and the central initial position is proportional to $[1, 0, 0]^T$. The matrix $\mathbf{G}^{(c)}$ can be computed using the Gram-Schmidt process. Note that in (1.24) and (1.25), $A > 0$, $B \in \mathbb{R}$ and $C > 0$ are positive constants for the central state (and $AC > 0$). Section B.5 briefly discusses key steps related to the Gram-Schmidt process. Superscripts (c) and (d) indicate central and deviated states respectively. Fig. 1.6 shows a visual illustration. The position and velocity vectors for the central state take the form,

$$\mathbf{x}^{\text{CRTN}(c)}(0) = \mathbf{G}^{(c)} \mathbf{x}^{\text{ECI}(c)}(0) = \begin{bmatrix} A \\ 0 \\ 0 \end{bmatrix}, \quad (1.24)$$

$$\dot{\mathbf{x}}^{\text{CRTN}(c)}(0) = \mathbf{G}^{(c)} \dot{\mathbf{x}}^{\text{ECI}(c)}(0) = \begin{bmatrix} B \\ C \\ 0 \end{bmatrix}, \quad (1.25)$$

and the deviated states in the point cloud can be represented in terms of departures from the central state,

$$\mathbf{x}^{\text{CRTN}}(0) = \mathbf{x}^{\text{CRTN}(d)}(0) = \mathbf{G}^{(c)} \mathbf{x}^{\text{ECI}(d)}(0) = \begin{bmatrix} A + \epsilon_1 \\ \epsilon_2 \\ \epsilon_3 \end{bmatrix}, \quad (1.26)$$

$$\dot{\mathbf{x}}^{\text{CRTN}}(0) = \dot{\mathbf{x}}^{\text{CRTN}(d)}(0) = \mathbf{G}^{(c)} \dot{\mathbf{x}}^{\text{ECI}(d)}(0) = \begin{bmatrix} B + \delta_1 \\ C + \delta_2 \\ \delta_3 \end{bmatrix}, \quad (1.27)$$

where, $\boldsymbol{\epsilon}$ ($\boldsymbol{\epsilon} = [\epsilon_1, \epsilon_2, \epsilon_3]^T$) and $\boldsymbol{\delta}$ ($\boldsymbol{\delta} = [\delta_1, \delta_2, \delta_3]^T$) are typically “small” deviations.

Note. Previously we discussed the Cartesian and Keplerian coordinates. The Cartesian-CRTN position (unit vector representation, denoted by $\mathbf{x}^{\text{CRTN-unit}}(t)$ in

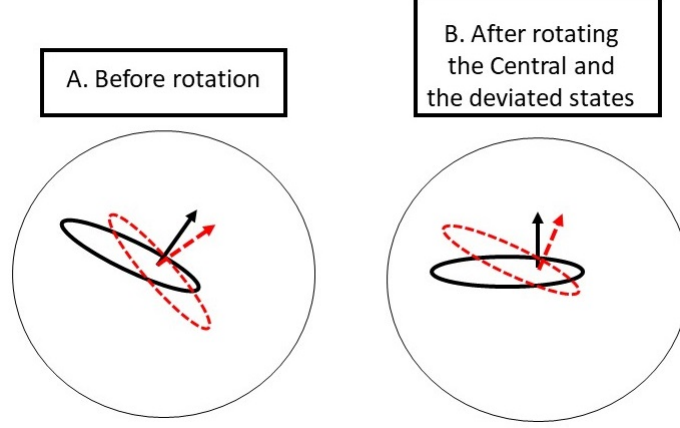


Figure 1.6: **Reconstructing the central and deviated state (Not scaled to size)**. The left panel (A) shows both the central and deviated states *before* performing the rotation. The right panel (B) shows both the states *after* performing the rotation. Note that the red dotted ellipse and the red dotted line denote the *deviated* state and the deviated normal direction respectively, the black ellipse and the black line indicate the *central* state and the central normal direction.

Equation (1.28)) of an space object can be written in terms of the Keplerian elements (Fitzpatrick, 2012),

$$\mathbf{x}^{\text{CRTN-unit}}(t) = \frac{\mathbf{x}^{\text{CRTN}}(t)}{r(t)} = \begin{bmatrix} \cos \Omega \cos(\omega + T(t)) - \sin \Omega \sin(\omega + T(t)) \cos i \\ \sin \Omega \cos(\omega + T(t)) + \cos \Omega \sin(\omega + T(t)) \cos i \\ \sin i \sin(\omega + T(t)) \end{bmatrix}. \quad (1.28)$$

Further, if i (inclination angle) is very small or 0 (due to the change of basis) then $\mathbf{x}^{\text{CRTN-unit}}(t)$ can be written as,

$$\begin{aligned} \mathbf{x}^{\text{CRTN-unit}}(t) &\approx \begin{bmatrix} \cos \Omega \cos(\omega + T(t)) - \sin \Omega \sin(\omega + T(t)) \\ \sin \Omega \cos(\omega + T(t)) + \cos \Omega \sin(\omega + T(t)) \\ \sin i \sin(\omega + T(t)) \end{bmatrix} \\ &\approx \begin{bmatrix} \cos(\Omega + \omega + T(t)) \\ \sin(\Omega + \omega + T(t)) \\ \sin i \sin(\omega + T(t)) \end{bmatrix} \\ &\approx \begin{bmatrix} \cos \theta(t) \\ \sin \theta(t) \\ \sin i \sin(\theta(t) - \Omega) \end{bmatrix}, \end{aligned}$$

where, $\theta(t)$ ($\theta(t) = \Omega + \omega + T(t) = E_3(t)$ using the CRTN basis) denotes the propagated angle in the true anomaly scale (we also mention this angle as the propagated true longitude in Chapters 2 and 3).

1.8.2 Statistical analysis of propagated distributions

An important criterion for a “good” coordinate system is that a propagated point cloud at time $t = t_1$ should look approximately Gaussian, given an initial Gaussian distribution in Cartesian-CRTN coordinates at $t = 0$. Apart from judging Gaussianity visually, we judge approximate Gaussianity using the multivariate p-value tests developed by Mardia (Mardia *et al.*, 1979). Note that in Chapter 7 (Section 7.4), we perform an explorative study between various normality tests for the reliability (i.e., able to detect the slightest non-normality) analysis.

For simplicity attention is restricted to testing the full 6-dimensional point cloud for Gaussianity under each of our coordinate systems. The approximate multivariate normality is summarized by two p-values (one for the skewness and another for the kurtosis). If Gaussianity holds, the p-value will be uniformly distributed between 0 and 1. However, if normality fails, then the p-value will tend to be close to 0. To carry out a formal statistical test, a small threshold ν is chosen (e.g. $\nu = 0.05$) and if the p-value is below the threshold, then the hypothesis of Gaussianity is rejected. For each pairs plot in this thesis, a total of 2 p-values are computed. Further, in some places we also compute the Shapiro-Wilk’s univariate p-value (one p-value for each coordinate element) to check the univariate normality (Korkmaz *et al.*, 2014; MIT, 2010; Shapiro & Wilk, 1965).

Caution- The power of a statistical test depends on the sample size (here the number of simulated points in the point cloud). If the underlying distribution is even slightly non-normal, then for a large enough sample size, the hypothesis of normality will be eventually rejected.

Examples are listed in Chapters 2, 3 and 7.

1.9 Example 1.1., problems with the standard coordinate systems, simple illustration

Most of the standard coordinate systems suffer from two major issues. They are,

- (a) Bounded range problem
- (b) Curvature.

Bounded range: For some of the parameters, there may be a natural finite range. For example, the eccentricity of an ellipse lies between 0 and 1. Similarly, the latitude of a point on the sphere ranges between -90° and 90° . Further, these endpoints are often achievable: an ellipse with zero ellipticity is a circle, and latitude 90° corresponds to the north pole. If uncertainty is concentrated near one of these endpoints, then the resulting distribution cannot be normal and often the behavior is even more complicated to describe statistically.

Curvature: This problem is best illustrated in Cartesian coordinates, where the uncertainty spreads out along a curved path (see Chapter 2 for more details).

Next a simple example is provided to discuss the bounded range problem. Note that this example is not related to the orbital dynamics and the purpose of this example is to introduce the bounded range problem using the spherical coordinate system. An example of a bounded range problem in orbital dynamics settings can be found in the Appendix A (Fig. A.3).

Example 1.1. Bounded range problem

A problem with the bounded range is given by the unit sphere, where points can be represented either in Cartesian coordinates $(x_1^{\text{unit}}, x_2^{\text{unit}}, x_3^{\text{unit}})$ or in spherical coordinates, θ (longitude) and ψ (latitude),

$$x_1^{\text{unit}} = \cos \psi \cos \theta; \quad x_2^{\text{unit}} = \cos \psi \sin \theta; \quad x_3^{\text{unit}} = \sin \psi.$$

Here $\psi \in [-90^\circ, 90^\circ]$ denotes the latitude and $\theta \in [-180^\circ, 180^\circ]$ is the longitude. Consider a highly concentrated distribution on the sphere (more specifically, a Fisher distribution with concentration parameter $\kappa = 2500$, number of data points $N = 2000$), with two possible centers.

- (a) The first center lies on the **equator** with $\psi = 0^\circ$; $\theta = 0^\circ$ (Fig. 1.8).
- (b) The second center lies at the **north pole** with $\psi = 90^\circ$ and θ is undefined (Fig 1.8).

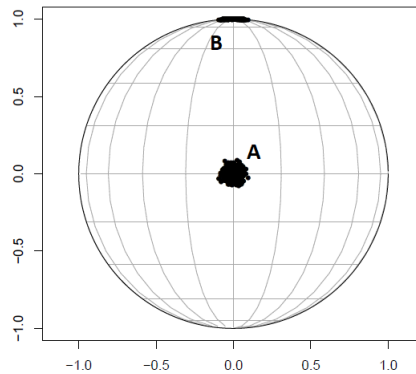


Figure 1.7: **Example 1.1., bounded range problem, part 1.** The unit sphere with two concentrated point clouds are plotted, one near the equator (A) and one near the north pole (B).

Point clouds for simulated values of θ and ψ are plotted in Fig. 1.7. For the first distribution (A), ψ lies a long way from its endpoints, and the distributions of θ and ψ look normal (Fig. 1.8). For the second distribution (B), $\psi = 90^\circ$ lies at the endpoint of possible values. In this case the distribution of ψ suffers from *bounded range* problem and approximately follows an exponential distribution and θ is uniformly distributed on the circle (Fig. 1.8), both of which are very non-normal.

For parameters lying on a sphere, a good strategy is to orient the coordinate system to be like the first case rather than the second case.

1.10 Tracking Problem

As mentioned in Section 1.2, the problem of space debris tracking can be treated by using a Kalman filter. Typically, Kalman filters can be classified into two categories, (i) linear and (ii) non-linear. As the name suggests, for the linear or

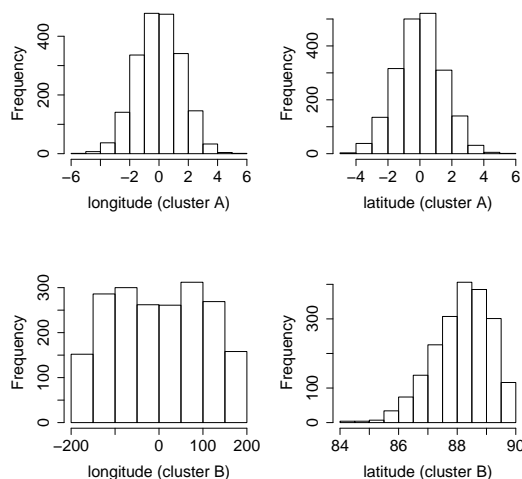


Figure 1.8: **Example 1.1., bounded range problem, part 2.** Spherical coordinates for both distributions.

classic Kalman filter, the transformation from the state vector to the observation vector is linear. One example of such a problem is the 2-dimensional position and velocity tracking problem, where the state vector consists of the position and velocity and the observation vector is made of the position ($u_{\text{loc}}(t) = u_{\text{loc}}(0) + v_{\text{vel}}t$. Here, $u_{\text{loc}}(t)$, $u_{\text{loc}}(0)$, v_{vel} and t indicate position at time t , position at time 0, velocity and time respectively).

However, most of the real world tracking problems are non-linear. The term “non-linear” indicates that the transformation from the state vector to the observation vector is non-linear. One example of a non-linear filtering is the aircraft range tracking problem. In this problem the state vector consists of the velocity (v_{vel}) and the altitude (r) (assuming that the initial location at time $t = 0$ is 0) and the observation vector contains the slant range (y_{slant}), $y_{\text{slant}}(t) = \sqrt{v_{\text{vel}}^2 t^2 + r^2}$. The space object tracking problem is non-linear, Chapters 4 and 5 discuss it.

Two commonly used non-linear Kalman filters are the EKF and UKF. The EKF uses first order Taylor series expansion. The UKF uses $2l + 1$ (l is the dimension) weighted sigma points. The term “sigma” refers to the standard deviation, these points are generated by computing the standard deviation (and

the mean) of a distribution. For instance, assume a univariate normal distribution with mean y and standard deviation ξ_1 , then three sigma points will be located at y , $y + W\xi_1$ and $y - W\xi_1$. Note that W denotes the weight. Further details on the EKF and UKF can be found in Chapter 4. Note that $l = 6$ (6-dimensional state vector and 2-dimensional observation vector) for the orbital tracking problem.

1.11 Association Problem

Suppose that for a library of space objects, their predicted angular positions (2-dimensional angular position, the latitude and the longitude measured with respect to the ECI or CRTN reference frame using the spherical coordinate system) at the current time are available from previous observations, including an assessment of the errors. Given a new angles-only observation at the current time, the objective is to decide which object, if any, in the library corresponds to the observed object.

Fig 1.9 illustrates some of the issues that can arise. Assume a library of two objects (A and B) and three potential observations (1, 2 and 3).

Point 1 lies in the main body of the distribution for object A , but not for object B . Hence the posterior probability that point 1 comes from object A is large. Point 2 is more closely associated with B than A , but lies far enough from B that it might be considered incompatible with either object. Point 3 lies midway between the two principal axes, but is close enough to the common mode to be compatible with both distributions. In particular, the posterior probabilities will be nearly equal.

1.12 Thesis summary

This thesis first discusses the 6-dimensional propagated state vector and introduces the AST-CRTN coordinate system. Second, the ASP-CRTN coordinate system (propagated 2-dimensional state vector in the ambient space) and the PN distribution are introduced. Further, suitable examples are provided to illustrate their various usages. Finally, the tracking problem is discussed.

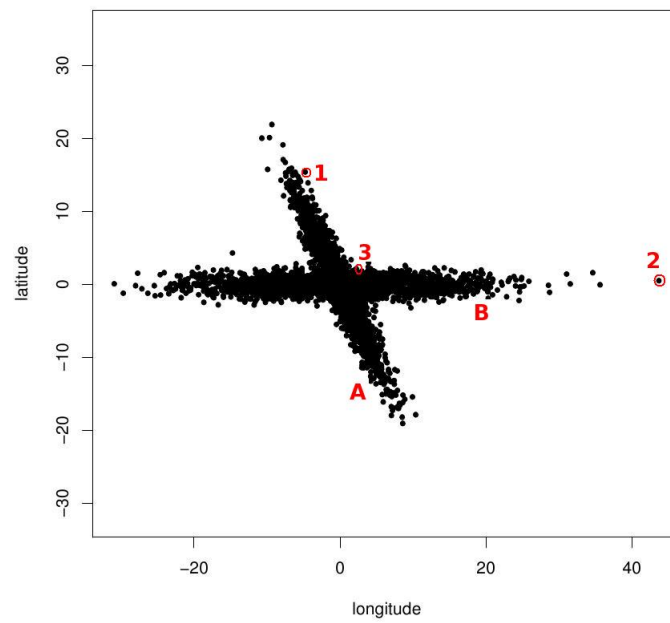


Figure 1.9: **Association problem.** Two overlapping distributions A and B for the angles-only part of a state vector. The distributions are represented by point clouds in the tangent plane to the unit sphere in terms of the latitude and longitude in degrees. In addition three possible observations, labeled 1,2,3, have been highlighted.

- (a) *The propagated 6-dimensional state vector:* use the AST-CRTN coordinate system as it is able to preserve approximate normality under a wide range of conditions. See Chapter 2 for more details.
- (b) *Propagated 2-dimensional angles-only position:* the angles-only position is measured in terms of the longitude and the latitude and the angles-only observation vector may suffer from the pinching effect. During the pinching (break-up event) scenario the propagated angles-only distribution cannot be approximated using a bivariate normal distribution. This thesis investigates the reason and discusses the PN or “Pinched-Normal” distribution. See Chapter 3 for more details.
- (c) *Filtering:* the UKF and EKF are sometimes unable to approximate the posterior mean and the variance accurately. However, the IUKF, IEKF, OCUKF and OCEKF are able to approximate the posterior distribution accurately. This thesis discusses application of these filters for solving the space object tracking problem. See Chapters 4, 5 and 6 for more details.

Thesis contributions are visualized using Figs. 1.10 and 1.11.

Note that spherical coordinates (spherical-ECI and ASP-CRTN) are either 2 or 3 dimensional. In a sense, these two coordinates are incomplete as they only deal with the position of an orbiting object.

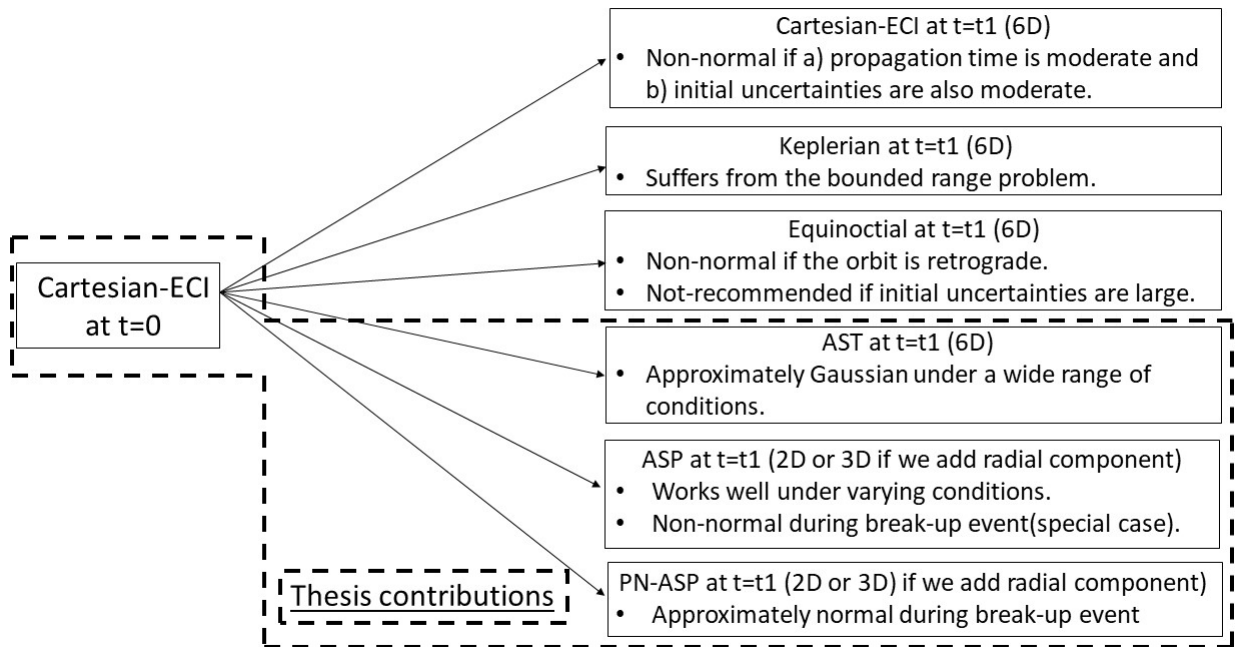


Figure 1.10: **Thesis contributions, part 1.** Uncertainty propagation in different coordinate systems.

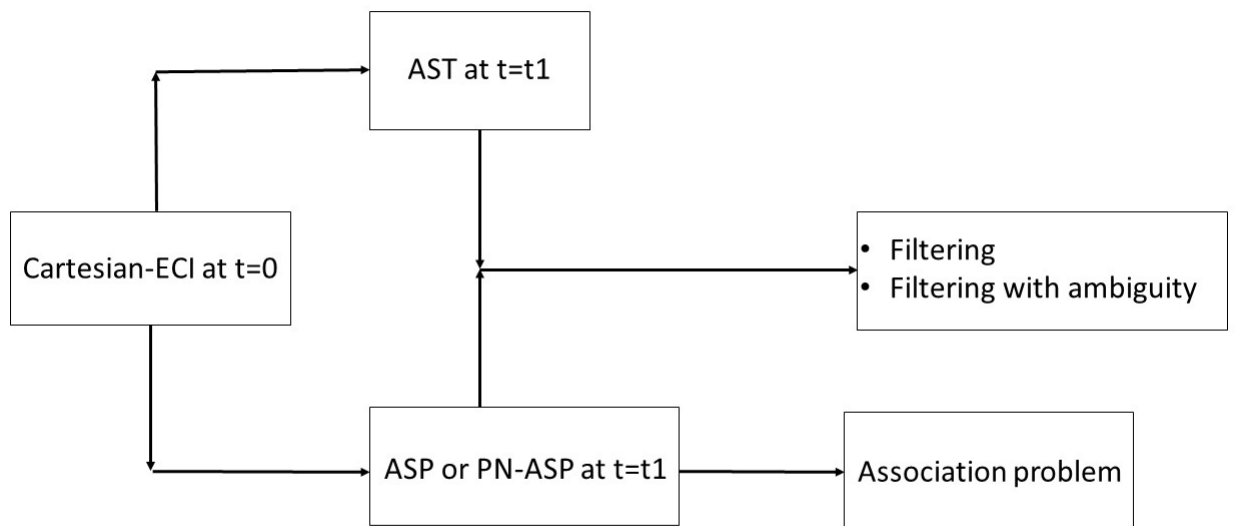


Figure 1.11: **Thesis contributions, part 2.** Applications of newly developed coordinate systems to the filtering and association problems.

Chapter 2

Representing uncertainties associated with the propagated state vector

2.1 Introduction

In this chapter we discuss the distribution of the propagated 6-dimensional state vector. Previously, we discussed the Cartesian-ECI, Keplerian-ECI and Equinoctial-ECI coordinate systems and highlighted some of the limitations of these coordinates. In this chapter the “Adapted STructural (AST)” coordinate system (AST-CRTN) is introduced. A number of statistical tests are carried out to judge the quality of Gaussianity in the AST-CRTN coordinate system. The first portion of this chapter introduces the AST-CRTN coordinate system and highlights its key differences with the Equinoctial-ECI (and Equinoctial-CRTN) coordinate system. The second portion deals with various statistical tests, which are performed to test approximate Gaussian behavior in the AST-CRTN coordinate system.

2.2 Chapter summary and key contributions

Key contributions are listed below.

- (1) The AST-CRTN coordinate system is introduced in this chapter and key differences with the Equinoctial-ECI/CRTN coordinate system (and other coordinate systems) are also listed (Section [2.4](#)).

- (2) A number of investigations are performed to analyze the quality of approximate Gaussian behavior in the AST-CRTN coordinate system (Section 2.5). These tests are listed below.
- (a) Representing AST-CRTN elements using the first order Taylor series expansion (Subsection 2.5.1).
 - (b) Linearity analysis (Subsection 2.5.2).
 - (c) Point cloud propagation under high initial uncertainties (Subsection 2.5.3).

2.3 Relation to other chapters

The previous chapter introduced various coordinate systems (Subsection 1.7.6) and briefly talked about their limitations. This chapter provides further evidences using suitable examples. The theme of this chapter is the AST-CRTN coordinate system and the representation of the propagated uncertainty at the AST-CRTN coordinate system (at $t = t_1, t_1 > 0$) depends on the uncertainty at the Cartesian-ECI state vectors at $t = 0$.

$$\text{Cartesian-ECI}(0) \longrightarrow \text{Cartesian-CRTN}(0) \longrightarrow \text{AST-CRTN}(t)$$

Further, mappings between the Cartesian-ECI/CRTN, Keplerian-ECI/CRTN, Equinoctial-ECI/CRTN coordinate systems to the AST-CRTN coordinate system are bijective. The AST-CRTN coordinate system can be used to construct the ASP-CRTN coordinate system (discussed in the next chapter). Application of the AST-CRTN coordinate system for solving tracking problem is illustrated in the Chapters 5 and 6 using suitable examples.

2.4 The AST-CRTN coordinate system

This chapter discusses the *Adapted STructral (AST-CRTN) coordinate system*. The logic here is somewhat different to the *fixed* coordinate systems (such as the Cartesian-ECI, Keplerian-ECI and Equinoctial-ECI) described in the previous chapter. The term *fixed* means that these coordinate systems are developed on

2.4 The AST-CRTN coordinate system

the fixed frame of reference. The AST-CRTN coordinate system uses a *local* or *adapted* frame of reference, so that the uncertainty in the state can generally be represented using the Gaussian distribution. The term *local* means that the coordinate system depends on the central state and it is designed based on the rotating frame (or local to the rotated central state) of reference.

The starting point for AST-CRTN coordinates is a known approximate value for the state of an orbiting object at time $t = 0$. This value is called the *central state* ($\mathbf{x}^{\text{CRTN}(c)}(0), \dot{\mathbf{x}}^{\text{CRTN}(c)}(0)$) and the central state provides a *reference basis*. Like the previous chapter, features related to the central and deviated states will be indicated with a superscript (c) and (d) . The *deviated state* is assumed to lie near the central state

Let CRTN stand for the *central RTN basis*, that is, the RTN basis (see Equations (1.4) to (1.6), Subsection 1.7.3) determined from the central state at the initial time $t = 0$. Then AST coordinates, denoted A_1, \dots, A_6 , are defined to be a local version of Equinoctial coordinates (Equinoctial-ECI), i.e., the Equinoctial coordinates defined with respect to the CRTN basis, with some small adjustments:

$$\begin{aligned} A_1 &= 2 \tan(i^{\text{CRTN}}/2) \cos(\Omega^{\text{CRTN}}), & A_2 &= 2 \tan(i^{\text{CRTN}}/2) \sin(\Omega^{\text{CRTN}}), \\ A_3(t) &= \phi^{\text{CRTN}}(t), & A_4 &= e \cos(\theta_p^{\text{CRTN}}), \\ A_5 &= e \sin(\theta_p^{\text{CRTN}}), & A_6 &= n. \end{aligned} \tag{2.1}$$

Time varying elements: Note that under Keplerian dynamics only $A_3(t)$ changes with time. Various angles in Equation (2.1) can be computed same as in Subsection 1.7.3, but using the CRTN reference basis.

The AST-CRTN coordinates differ from Equinoctial-ECI coordinates in three ways. The most important difference is the choice of reference basis (the central RTN or CRTN basis for AST-CRTN coordinates instead of the standard ECI basis for Equinoctial-ECI coordinates). The other two differences are that the angular position of the orbiting object, $A_3(t)$, is represented on the mean anomaly scale rather than the true anomaly scale (and is treated as a number rather than an angle) using the reinvented break angle (or the CRTN break angle), A_6 , is

2.4 The AST-CRTN coordinate system

defined by the mean motion n instead of the major semi-axis a . These last two choices are made to linearize the propagation equation. The term *reinvented* indicates that we redefined the original break angle ($E_3(t)$) for the AST-CRTN coordinate system.

A detailed examination of AST-CRTN coordinates will be given in the next section. Key differences between the AST-CRTN coordinate system and the Equinoctial-ECI coordinate system are summarized below.

- (a) **Retrograde orbits.** Standard Equinoctial (Equinoctial-ECI) coordinates (E_1, E_2 , see Subsection 1.7.6.3) generally break down for a nearly retrograde equatorial orbit (for which the inclination approaches π). For AST-CRTN coordinates the problem does not arise. The inclination of the central state always equals 0° and the inclinations for the deviated states are always close to 0° .
- (b) **Linear propagation and winding number.** The system equation is a linear function of $\phi^{\text{CRTN}}(0)$ and n for time t (Equation (1.21)). Thus if the initial values of $\phi^{\text{CRTN}}(0)$ and n are Gaussian, the propagated value of $\phi^{\text{CRTN}}(t)$ remains Gaussian for all future times t .

Further, the use of this representation makes it straightforward to keep track of the *winding number*, that is, how many times the orbiting object has gone around its orbit. More specifically, without any knowledge of the history of the orbiting object, the initial angle $\phi^{\text{CRTN}}(0)$ only makes sense as an angle; that is $\phi^{\text{CRTN}}(0)$ and $\phi^{\text{CRTN}}(0) + 2\pi k$ represent the same angle for any integer k . The initial angle can be turned into a number by restricting it to the interval $[-\pi, \pi]$. Once $\phi^{\text{CRTN}}(0)$ has been turned into a number, $\phi^{\text{CRTN}}(t)$ also makes sense as a number, and the integer part of $(\phi^{\text{CRTN}}(t) - \phi^{\text{CRTN}}(0))/2\pi$ records the whole number of orbits which have occurred by time t .

- (c) **Effects of change of basis due to rotation.** Consider a situation where the CRTN basis equals the standard ECI basis. Hence the central orbital plane is equatorial and the initial central state points towards the standard reference direction, $\mathbf{x}^{\text{ECI}(e)}(0) \propto \mathbf{u}$ (Equation (1.4)). Then the Equinoctial-ECI and AST-CRTN coordinates are identical except for small differences

in elements 3 and 6. Next rotate the central and deviated orbital planes by 90° (polar orbit, see Subsection 1.7.5) or more. The AST-CRTN coordinates remain unchanged. However, since the reference plane for Equinoctial coordinates remains equatorial, most (except E_6) of the Equinoctial coordinates undergo major changes.

2.5 Analyzing the AST-CRTN coordinate system

This section discusses approximate Gaussian behavior in the AST-CRTN coordinate system and three tests are performed to judge the Gaussianity.

- (1) First, we show that deviations represented using AST-CRTN coordinates can be approximated using the *first order* Taylor series expansion from the initial ($t = 0$) Cartesian-CRTN deviations. Since initial deviations are approximately normally distributed (at $t = 0$), the AST-CRTN coordinates of the deviations are also approximately normal. Hence, we can conclude that the transformation from the Cartesian-CRTN ($t = 0$) to the AST-CRTN ($t = t_1$) coordinate system is approximately linear.
- (2) Second, we perform linearity analysis and show that the transformation from the Cartesian-CRTN to the AST-CRTN coordinate system at time $t = 0$ is approximately linear.
- (3) Finally, we discuss a point cloud propagation example and show that the propagated point cloud in the AST-CRTN coordinate system can be approximated using a multivariate normal distribution. The key assumption in this example is initial uncertainty (at $t = 0$) is approximately Gaussian in the Cartesian-CRTN coordinate system. Similar to the previous two test results, this test also confirms that the transformation from the Cartesian-CRTN (at $t = 0$) to the propagated AST-CRTN ($t = t_1$) is approximately linear.

2.5.1 A first order representation for initial AST-CRTN coordinates

From Section 1.8.1, the Cartesian-CRTN representation of a central state and a deviated state at time $t = 0$ take the form,

$$\begin{aligned} \mathbf{x}^{\text{CRTN}(c)}(0) &= \begin{bmatrix} A \\ 0 \\ 0 \end{bmatrix}, & \dot{\mathbf{x}}^{\text{CRTN}(c)}(0) &= \begin{bmatrix} B \\ C \\ 0 \end{bmatrix} \\ \mathbf{x}^{\text{CRTN}(d)}(0) &= \begin{bmatrix} A + \epsilon_1 \\ \epsilon_2 \\ \epsilon_3 \end{bmatrix}, & \dot{\mathbf{x}}^{\text{CRTN}(d)}(0) &= \begin{bmatrix} B + \delta_1 \\ C + \delta_2 \\ \delta_3 \end{bmatrix}. \end{aligned}$$

In this section, a first order Taylor series expansion (see Section B.6 for more details on Taylor series expansion) is used to show how the difference in AST-CRTN coordinates between the deviated and the central state can be approximated by linear expressions of ϵ and δ ,

$$\mathbf{A}^{(d)} - \mathbf{A}^{(c)} = J \begin{bmatrix} \epsilon_1 \\ \epsilon_2 \\ \epsilon_3 \\ \delta_1 \\ \delta_2 \\ \delta_3 \end{bmatrix}, \quad (2.2)$$

where, J is the 6×6 Jacobian matrix from Cartesian-CRTN to AST-CRTN coordinates and $\mathbf{A}^{(d)} = \mathbf{A}$.

The formula for J is given below. The quality of this linear approximation is explored in the next section.

Computing the Jacobian matrix

2.5 Analyzing the AST-CRTN coordinate system

The Jacobian $\mathbf{J} = \partial(\text{AST-CRTN})/\partial(\text{Cartesian-CRTN}^T)$ takes the form

$$\mathbf{J} = \begin{array}{cccccc} & \epsilon_1 & \epsilon_2 & \epsilon_3 & \delta_1 & \delta_2 & \delta_3 & & \\ \left[\begin{array}{cccccc} 0 & 0 & -B/AC & 0 & 0 & 0 & 1/C \\ 0 & 0 & -1/A & 0 & 0 & 0 & 0 \\ 0 & D^{\text{coeff}}/A & 0 & 0 & 0 & 0 & 0 \\ C^2/\mu - 1/A & -BC/\mu & 0 & 0 & 0 & 2AC/\mu & 0 \\ -BC/\mu & B^2/\mu - 1/A & 0 & -AC/\mu & -AB/\mu & 0 & 0 \\ P_1C + P_2Q_1 & -P_1B + P_2Q_2 & 0 & P_1A + 2P_2A^2BC^2 & P_2Q_3 & 0 & 0 \end{array} \right] & \begin{array}{l} A1 \\ A2 \\ A3 \\ A4 \\ A5 \\ A6 \end{array} \end{array} \quad (2.3)$$

where

$$\begin{aligned} D^{\text{coeff}} &= \frac{(1 - e^{(c)2})^{3/2}}{(1 + e^{(c)} \cos T^{(c)})^2} \\ P_1 &= -\frac{3}{2} \frac{n^{(c)}}{h^{(c)2}} 2AC \\ P_2 &= -\frac{3}{2} \frac{n^{(c)} a^{(c)}}{h^{(c)2} \mu} \\ Q_1 &= \{(2C^2 - \frac{2\mu}{A})(AC^2 - \mu) + 2AB^2C^2\} \\ Q_2 &= \{-2BC(AC^2 - \mu) - 2AB^3C + BC\mu\} \\ Q_3 &= \{4AC(AC^2 - \mu) + 2A^2B^2C\}. \end{aligned}$$

Here is the derivation, with all expansions taken to first order in ϵ and δ . As mentioned in the previous section, the superscript (c) denotes the value of a parameter for the central state.

Expansion for $A_1(0)$ and $A_2(0)$. The angular momentum vector can be expressed as

$$\mathbf{h} = \mathbf{x}^{\text{CRTN}} \times \dot{\mathbf{x}}^{\text{CRTN}} = \begin{bmatrix} \epsilon_2\delta_3 - \epsilon_3(C + \delta_2) \\ \epsilon_3(B + \delta_1) - (A + \epsilon_1)\delta_3 \\ (A + \epsilon_1)(C + \delta_2) - \epsilon_2(B + \delta_1) \end{bmatrix} \approx \begin{bmatrix} -\epsilon_3C \\ \epsilon_3B - A\delta_3 \\ AC + A\delta_2 + C\epsilon_1 - \epsilon_2B \end{bmatrix},$$

with squared norm,

$$h^2 \approx A^2C^2 + 2AC(A\delta_2 + C\epsilon_1 - B\epsilon_2).$$

2.5 Analyzing the AST-CRTN coordinate system

That is,

$$h^2 \approx h^{(c)2} + \Delta_{h^2},$$

where $h^{(c)} = AC$ and

$$\Delta_{h^2} = 2AC(A\delta_2 + C\epsilon_1 - B\epsilon_2).$$

The first two components of $\mathbf{w}^{\text{unit}} = \mathbf{h}/h$ (\mathbf{w}^{unit} is a unit vector) simplify to

$$w_1^{\text{unit}} \approx -\epsilon_3 C, \quad w_2^{\text{unit}} \approx \epsilon_3 B - A\delta_3.$$

In terms of Keplerian elements,

$$w_1^{\text{unit}} = \sin i \sin \Omega \approx i \sin \Omega, \quad w_2^{\text{unit}} = -\sin i \cos \Omega \approx -i \cos \Omega$$

since the inclination angle i is small. Further, the first two AST-CRTN coordinates are given by

$$2 \tan(i/2) \sin(\Omega) \approx i \sin(\Omega) \approx w_1^{\text{unit}}, \quad 2 \tan(i/2) \cos(\Omega) \approx i \cos(\Omega) \approx -w_2^{\text{unit}},$$

thus confirming the first two rows of J .

Expansion for $A_3(0)$. For this section, write the first order representation of the deviated basis at time $t = 0$ in more concise notation. Using the spherical coordinate representation,

$$\mathbf{x}^{\text{CRTN}}(0) = \begin{bmatrix} A + \epsilon_1 \\ \epsilon_2 \\ \epsilon_3 \end{bmatrix} = r(0) \begin{bmatrix} \cos \psi(0) \cos \theta(0) \\ \cos \psi(0) \sin \theta(0) \\ \sin \psi(0) \end{bmatrix} \quad (2.4)$$

Note that $r(0), \theta(0)$ and $\psi(0)$ indicate the radial distance, longitude and latitude at time $t = 0$. From Equation (2.4), $\theta(0)$ can be written as,

$$\theta(0) = \text{atan2}(\epsilon_2, A + \epsilon_1) \approx \frac{\epsilon_2}{A}. \quad (2.5)$$

The final step is to transform from the true anomaly scale to the mean anomaly scale. The value of $\theta(0)$ is related to the true anomaly by $\theta(0) = \theta_p + T(0)$ and

$$\begin{aligned} \phi(0) &= F_{\text{T-to-M}}(\theta_p, e) + F_{\text{T-to-M}}(T(0), e) \\ &= F_{\text{T-to-M}}(\theta(0) - T(0), e) - F_{\text{T-to-M}}(-T(0), e) \\ &\approx F_{\text{T-to-M}}(-T(0), e) + \theta(0) F'_{\text{T-to-M}}(-T(0), e) - F_{\text{T-to-M}}(-T(0), e) = \theta(0) F'_{\text{T-to-M}}(-T(0), e) \\ &= \theta(0) F'_{\text{T-to-M}}(T(0), e) \\ &\approx \theta(0) F'_{\text{T-to-M}}(T^{(c)}(0), e^{(c)}). \end{aligned}$$

2.5 Analyzing the AST-CRTN coordinate system

Note. F' means derivative with respect to the first argument.

The derivative is well-known,

$$(\delta/\delta T)F_{\mathbf{T-to-M}}(T, e) = \frac{(1 - e^2)^{3/2}}{(1 + e \cos T)^2} \quad (2.6)$$

It does not matter to first order whether the deviated or central value is used since f_1 and e are close to $f_1^{(c)}$ and $e^{(c)}$.

Expansion for $A_4(0)$ and $A_5(0)$. After a bit of calculation, the expression for the eccentricity vector \mathbf{e} simplifies to

$$\mathbf{e} \approx \frac{1}{\mu} \begin{bmatrix} AC^2 + 2\delta_2 AC + \epsilon_1 C^2 - \epsilon_2 BC - \mu - \mu\epsilon_1/A \\ -ABC - \delta_1 AC - \epsilon_1 BC - \delta_2 AB + \epsilon_2 B^2 - \mu\epsilon_2/A \\ -\delta_3 AB - \epsilon_3 B^2 - \epsilon_3 C^2 - \mu\epsilon_3/A \end{bmatrix},$$

and since $\mathbf{e} = f_1 \mathbf{u}^{(e)} + f_2 \mathbf{v}^{(e)}$,

$$\begin{aligned} f_1 &\approx \frac{1}{\mu} (AC^2 + 2\delta_2 AC + \epsilon_1 C^2 - \epsilon_2 BC - \mu - \mu\epsilon_1/A), \\ f_2 &\approx \frac{1}{\mu} (-ABC - \delta_1 AC - \epsilon_1 BC - \delta_2 AB + \epsilon_2 B^2 - \mu\epsilon_2/A). \end{aligned}$$

The first order error terms determine rows 4 and 5 of J .

Expansion for $A_6(0)$. From \mathbf{e} , compute its squared norm

$$\begin{aligned} e^2 &= \frac{1}{\mu^2} \{ (AC^2 - \mu)^2 \\ &\quad + 2(2\delta_2 AC + \epsilon_1 C^2 - \epsilon_2 BC - \mu\epsilon_1/A)(AC^2 - \mu) \\ &\quad + (ABC)^2 \\ &\quad + 2(\delta_1 AC + \epsilon_1 BC + \delta_2 AB - \epsilon_2 B^2 + \mu\epsilon_2/A)(ABC) \}. \end{aligned}$$

Write

$$e^2 = e^{(c)2} + \Delta_e^2,$$

where $e^{(c)2}$ denotes the eccentricity for the central state.

$$h^2 = h^{(c)2} + \Delta_h^2,$$

2.5 Analyzing the AST-CRTN coordinate system

where $h^{(c)}$ denotes the magnitude of the central angular momentum vector. Then we can write (true to a certain extent),

$$\begin{aligned}
 e^{(c)2} &= \frac{1}{\mu^2} \{(AC^2 - \mu)^2 + (ABC)^2\}, \\
 \Delta_e^2 &\approx \frac{1}{\mu^2} \{2(2\delta_2 AC + \epsilon_1 C^2 - \epsilon_2 BC - \mu\epsilon_1/A)(AC^2 - \mu) \\
 &\quad + 2(\delta_1 AC + \epsilon_1 BC + \delta_2 AB - \epsilon_2 B^2 + \mu\epsilon_2/A)(ABC)\}, \\
 h^{(c)2} &= A^2 C^2, \\
 \Delta_h^2 &= 2AC(A\delta_2 + C\epsilon_1 - B\epsilon_2).
 \end{aligned}$$

Then a takes the form

$$\begin{aligned}
 a &= \frac{h^2}{\mu} \frac{1}{1 - e^2} \\
 &\approx \frac{h^{(c)2}}{\mu} \frac{1}{1 - e^{(c)2}} \left(1 + \frac{\Delta_h^2}{h^{(c)2}} + \frac{\Delta_e^2}{1 - e^{(c)2}}\right) \\
 &= a^{(c)} + \Delta_a,
 \end{aligned}$$

where,

$$a^{(c)} = \frac{h^{(c)2}}{\mu} \frac{1}{1 - e^{(c)2}} \text{ and } \Delta_a = a^{(c)} \left(\frac{\Delta_h^2}{h^{(c)2}} + \frac{\Delta_e^2}{1 - e^{(c)2}} \right).$$

$$\begin{aligned}
 a^{(c)} &= \frac{h^{(c)2}}{\mu} \frac{1}{1 - e^{(c)2}} \\
 &= - \frac{A^2 C^2}{\frac{A^2 B^2 C^2}{\mu} + \frac{A^2 C^4}{\mu} - 2AC^2} \\
 &= \frac{A\mu}{2\mu - AB^2 - AC^2}
 \end{aligned}$$

2.5 Analyzing the AST-CRTN coordinate system

Finally, writing $n = \sqrt{\mu/a^3}$ in the form $n = n^{(c)} + \Delta_n$, it follows that

$$\begin{aligned}
 n &= \sqrt{\frac{\mu}{(a^{(c)} + \Delta_a)^3}} \\
 &\approx \sqrt{\frac{\mu}{a^{(c)3}} \left(1 - \frac{3\Delta_a}{2a^{(c)}}\right)} \\
 &\approx n^{(c)} \left(1 - \frac{3\Delta_a}{2a^{(c)}}\right) \\
 &\approx n^{(c)} - \frac{3\Delta_a}{2a^{(c)}} n^{(c)} \\
 &\approx n^{(c)} + \Delta_n, \text{ say.}
 \end{aligned}$$

Finally,

$$\begin{aligned}
 \Delta_n &= -\frac{3\Delta_a}{2a^{(c)}} n^{(c)} \\
 &= -\frac{3n^{(c)}}{2a^{(c)}} (\Delta_a) \\
 &= -\frac{3n^{(c)}}{2a^{(c)}} \left(a^{(c)} \left(\frac{\Delta_h^2}{h^{(c)2}} + \frac{\Delta_e^2}{1 - e^{(c)2}} \right) \right) \\
 &= -\frac{3}{2} n^{(c)} \left(\frac{\Delta_h^2}{h^{(c)2}} + \frac{\Delta_e^2}{1 - e^{(c)2}} \right) \\
 &= -\frac{3}{2} n^{(c)} \left(\frac{\Delta_h^2}{h^{(c)2}} \right) - \frac{3}{2} n^{(c)} \left(\frac{\Delta_e^2}{1 - e^{(c)2}} \right) \\
 &= -\frac{3}{2} n^{(c)} \left(\frac{\Delta_h^2}{h^{(c)2}} \right) - \frac{3}{2} n^{(c)} \left(\frac{\Delta_e^2 \mu a^{(c)}}{h^{(c)2}} \right) \\
 &= -\frac{3}{2} \frac{n^{(c)}}{h^{(c)2}} (\Delta_h^2 + \Delta_e^2 \mu a^{(c)}).
 \end{aligned}$$

2.5.2 Linearity analysis for initial AST-CRTN coordinates

This section explores the extent to which AST-CRTN coordinates at the initial time $t = 0$ depend linearly on ϵ and δ . In order to simplify the study to its mathematical essentials, suppose the length and time units are scaled so that the gravitational constant is $\mu = 1$ and the central orbital period is $\square p = 2\pi$. Then an initial central state can be specified by giving the eccentricity e and the initial

2.5 Analyzing the AST-CRTN coordinate system

true anomaly $T(0)$. The corresponding values of A, B, C are given by

$$A = \frac{h^2}{1 + e \cos T(0)}, \text{ where } h^2 = 1 - e^2,$$

$$C = \frac{h}{A}, \quad B = \frac{e}{AC} \sin T(0).$$

The error variances are most conveniently specified in terms of relative errors. For this study set the position standard error σ to be a specified percentage $P_\sigma\%$ of the geometric mean of the radius at perigee and apogee. Similarly set the velocity standard error τ to be a specified percentage $P_\tau\%$ of the geometric mean of the speed at the perigee and the apogee. In standardized units, these geometric means for position and velocity reduce to h and 1, respectively.

Note that

$$h^2 = a\mu(1 - e^2),$$

$$r_a = \frac{h^2}{\mu} \frac{1}{1 + e \cos(\pi)} = \frac{h^2}{\mu} \frac{1}{1 - e},$$

$$r_p = \frac{h^2}{\mu} \frac{1}{1 + e \cos(0)} = \frac{h^2}{\mu} \frac{1}{1 + e},$$

$$v_a = \sqrt{\frac{(1 - e) \mu}{(1 + e) a}},$$

$$v_p = \sqrt{\frac{(1 + e) \mu}{(1 - e) a}}.$$

The radii of an elliptical orbit at apogee (r_a) and perigee (r_p) are given by $(h^2/\mu)/(1 - e)$ and $(h^2/\mu)/(1 + e)$, where $h^2 = 1 - e^2$. Hence if the length and time units are chosen so that $\mu = 1$, the geometric mean reduces to $\sqrt{1 - e^2}$.

Similarly, it can be shown that the velocities at apogee (v_a) and perigee (v_p) are given by $\sqrt{\frac{(1-e)}{(1+e)}}$ and $\sqrt{\frac{(1+e)}{(1-e)}}$, respectively, so the geometric mean reduces to 1.

For each component of ϵ and δ , 5 equally spaced values were chosen from -2σ to $+2\sigma$ and -2τ to $+2\tau$, respectively. Then for each AST-CRTN coordinate and each coordinate of ϵ and δ a plot is constructed. The plot shows how each

2.5 Analyzing the AST-CRTN coordinate system

AST-CRTN coordinate varies as the corresponding coordinate of ϵ or δ takes its 5 possible values (with the other components of ϵ and δ fixed at 0). Also superimposed on the plot is a straight line with slope given by the corresponding element of the Jacobian matrix J . Thus a total of 36 plots are generated. If the mapping from ϵ and δ is exactly linear, then the 5 “test values” in each of the 36 plots should lie exactly on the straight line.

Example 2.1. To judge the quality of the linear approximation for AST-CRTN coordinates, a challenging set of parameters are chosen, with a high eccentricity, $e = 0.7$, and high relative standard error, $P_\sigma = 2.5\%$, $P_\tau = 10\%$. This eccentricity is at the high end of what is observed in practice. The error rates are far higher than usually found in practice, but are kept small enough to ensure that deviated eccentricity is always less than 1.

Various choices were tried for the initial true anomaly; the choice $T(0) = 45^\circ$ is shown here, but the choice of $T(0)$ has little effect.

Figs. 2.1-2.2 show that even under these extreme conditions, most of the plots are visually very close to linearity. The worst one is plot (1,6) in Fig. 2.1 with a squared correlation coefficient of $R^2 = 0.977$; even this plot is acceptably linear for most purposes. The quality of the linear approximation improves with a) lower standard errors and b) lower eccentricity.

Note that in Figs. 2.1-2.2, within each row one Cartesian-CRTN coordinate varies over an interval with the other Cartesian-CRTN coordinates held fixed. The rows in Fig. 2.1 correspond to the three Cartesian-CRTN position coordinates. The rows in Fig. 2.2 correspond to the three Cartesian-CRTN velocity coordinates.

2.5.3 Point cloud propagation

Previous sections emphasized the initial behavior of deviated states under the Cartesian-CRTN and AST-CRTN coordinate systems. This section looks at the propagated distributions after a given propagation time t say, under Cartesian-CRTN, Keplerian-CRTN, Equinoctial-ECI (to show limitations of the Equinoctial-ECI coordinate system) and AST-CRTN coordinates. More propagation examples can be found in Section A.2.

2.5 Analyzing the AST-CRTN coordinate system

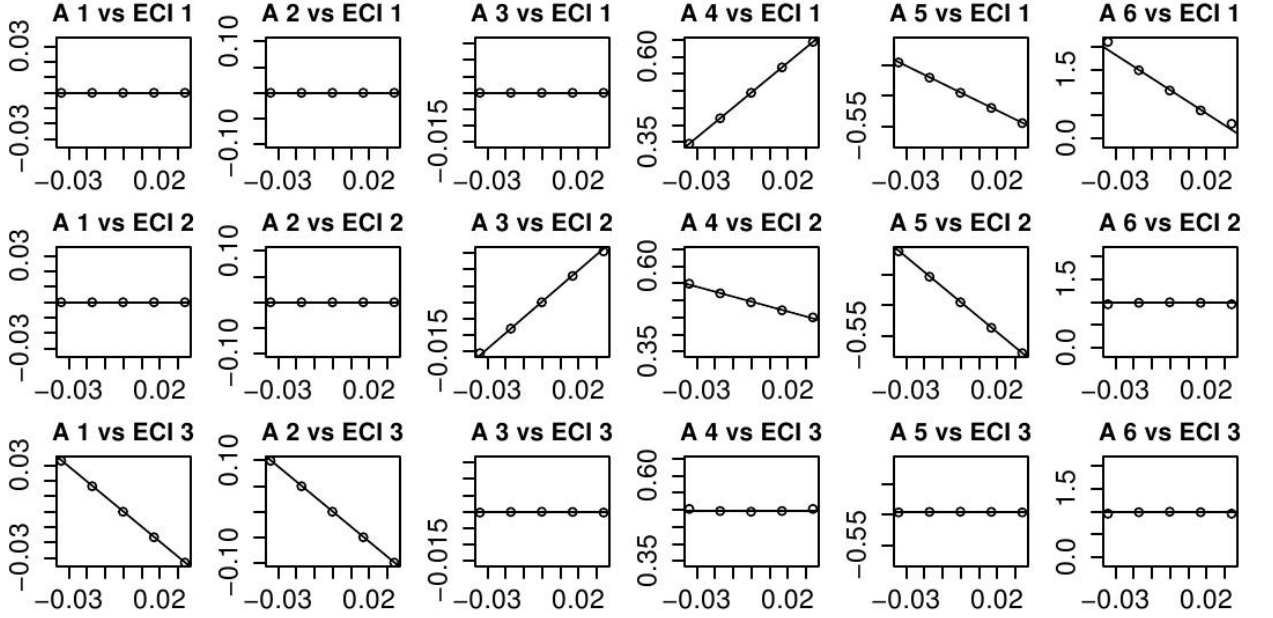


Figure 2.1: **Example 2.1., linearity example, part 1.** Linearity analysis at time $t = 0$ showing plots of each AST-CRTN coordinate against the first three Cartesian-CRTN coordinates. See also Fig. 2.2.

Recall Chapter 1, in Cartesian coordinates all 6 coordinates vary with time and some of the scatter-plots show distinct amount of curvature. However, for the Keplerian coordinate system only the third element ($T(t)$) changes with time. Similarly, for the Equinoctial and AST-CRTN coordinate systems only the third coordinate element ($E_3(t)$ and $A_3(t)$ respectively) varies with time.

The following example illustrates some of the problems with Cartesian-CRTN, Keplerian-CRTN and Equinoctial-ECI coordinates. Each 6-dimensional propagated distribution is simulated and the resulting point cloud is visualized using a pairs plots. Each pairs plot includes a histogram for each variable and a scatter plot for each pair of variables. The point clouds are based $N = 2000$ simulated initial states. This value of N is more than sufficient to see the patterns of variability in the propagated distributions. Indeed the same patterns can be identified using a much smaller value of N , e.g. $N = 500$.

Example 2.2. Consider a central orbit with eccentricity $e^{(c)} = 0.7$ (an important parameter) and initial true anomaly $T^{(c)}(0) = 45^\circ$ (a minor parameter).

2.5 Analyzing the AST-CRTN coordinate system

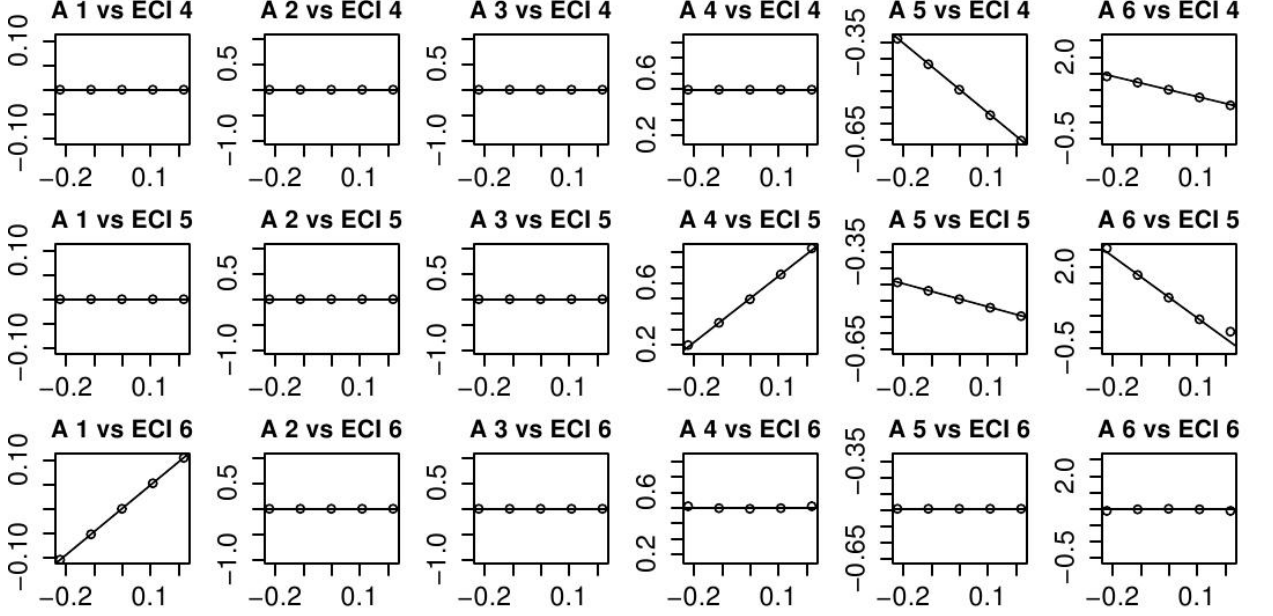


Figure 2.2: **Example 2.1., linearity example, part 2.** Linearity analysis at time $t = 0$ showing plots of each AST-CRTN coordinate against the last three Cartesian-CRTN coordinates.

Suppose the relative initial standard deviations are P_σ, P_τ , the same as before. For Equinoctial coordinates, the inclination is also an important parameter. If $i^{(c)} = 0$, then Equinoctial-ECI (same as Equinoctial-CRTN) and AST-CRTN coordinates are very similar; here let $i^{(c)} = 175^\circ$ to illustrate the problems that can arise for retrograde orbits.

In terms real world situations, if the period is 12 hours (equivalent to $a = 26610$ km), these parameters correspond to a highly eccentric orbit (HEO) (see Subsection 1.7.5 for more information on different orbits) with $A = 9078$ km, $B = 2.6$ km/sec and $C = 8.1$ km/sec. Further, $r_a = 45237$ km, $r_p = 7983$ km, $v_a = 1.6$ km/sec and $v_p = 9.21$ km/sec, where r_a, r_p, v_a and v_p indicate radius at the apogee, radius at the perigee, velocity at the apogee and velocity at the perigee respectively.

The state of the object has been propagated for 0.5 central orbital periods. Propagated point clouds have represented as 6-dimensional pairs plot in Cartesian-CRTN coordinates (Fig. 2.3), Keplerian-CRTN coordinates (Fig. 2.4),

2.5 Analyzing the AST-CRTN coordinate system

Equinoctial-ECI coordinates (Fig. 2.5) and AST-CRTN coordinates (Fig. 2.6). Note that more propagation examples are listed in the Appendix (Section A.2).

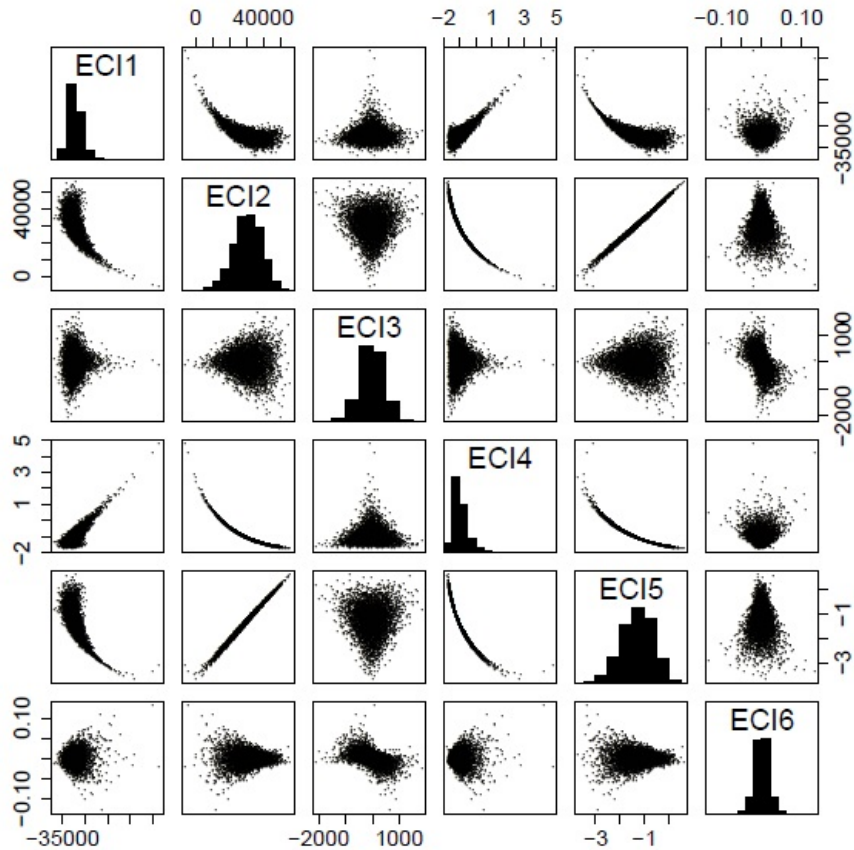


Figure 2.3: **Example 2.2., propagation example, Cartesian-CRTN coordinates.** Propagated point cloud in Cartesian-CRTN coordinates. First three elements represent the propagated position vector (km) and last three elements indicate the propagated velocity vector (km/sec).

From Figs. 2.3 to 2.6, the following conclusions can be made.

- (a) In **Cartesian-CRTN coordinates** (Fig. 2.3), there is extreme non-Gaussianity. E.g. the scatter plot (1,5) shows severe curvature. Even with much lower standard deviation, there would still often be appreciable curvature in such plots.

2.5 Analyzing the AST-CRTN coordinate system

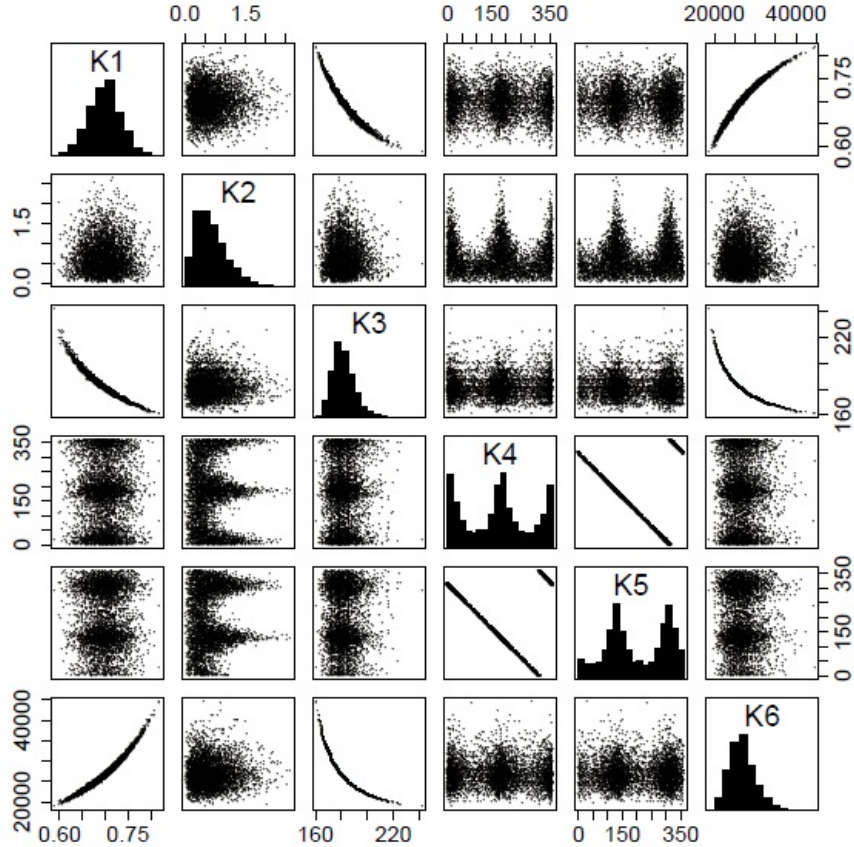


Figure 2.4: **Example 2.2., propagation example, Keplerian-CRTN coordinates.** Propagated point cloud in Keplerian-CRTN coordinates.

- (b) In **Keplerian-CRTN coordinates** (Fig. 2.4), there is extreme non-Gaussianity. E.g. the scatter plot (1,3) shows severe curvature. Notice the range for inclination (K2).
- (c) In **Equinoctial-ECI coordinates** (Fig. 2.5), there is also noticeable non-Gaussianity, e.g. the skewness in E1 and E2. The non-Gaussianity in this example is due to the high inclination of the orbital plane and demonstrates the problems with Equinoctial coordinates in this setting.
- (d) In **AST-CRTN coordinates** (Fig. 2.6), all the scatter plots are approximately normally distributed. Notice the perfect linear relation between

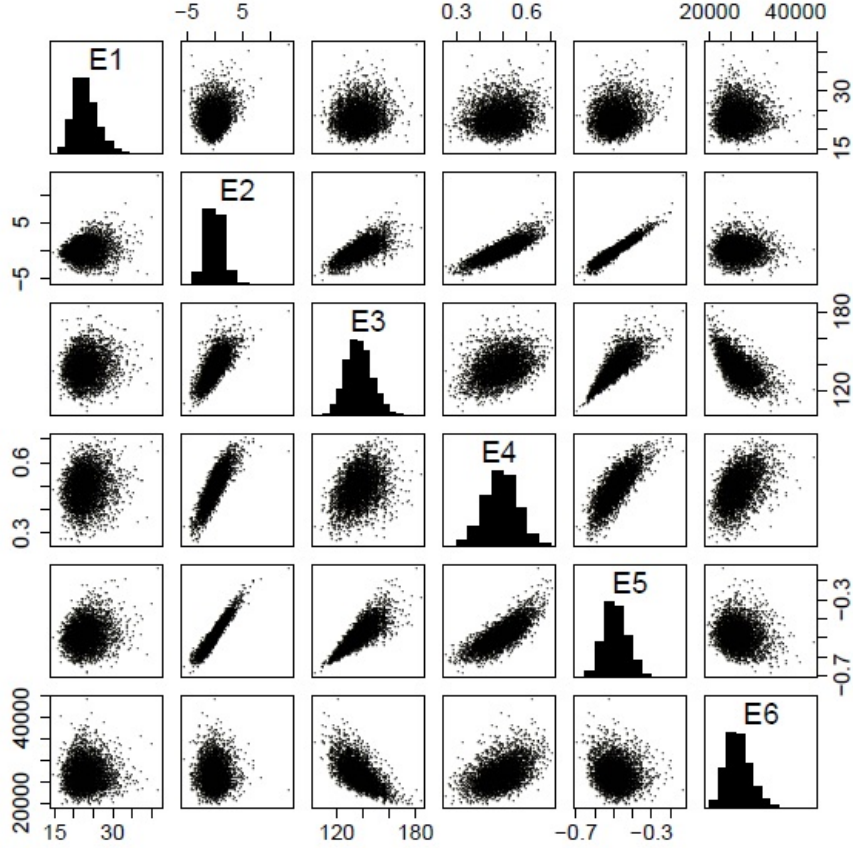


Figure 2.5: **Example 2.2., propagation example, Equinoctial-ECI coordinates.** Propagated point cloud in Equinoctial-ECI coordinates.

elements 3 and 6 ($\phi(t)$ and n) in scatter plot (3,6), which is due to the fact that the uncertainty in $\phi(t)$ is dominated by the variability in n for large t .

Multivariate test results

Section 1.8.2 discussed the p-value test in judging multivariate normality. In Figs. 2.3 to 2.6, we judge the approximate normality using Mardia's normality test. From visual inspection, it can be clearly stated that the propagated point cloud is approximately Gaussian only in the AST-CRTN coordinate system. The statistical test results are summarized in Table 2.1. For the Cartesian-CRTN, Keplerian-CRTN and Equinoctial-ECI coordinate systems very small p-values ($<$

2.5 Analyzing the AST-CRTN coordinate system

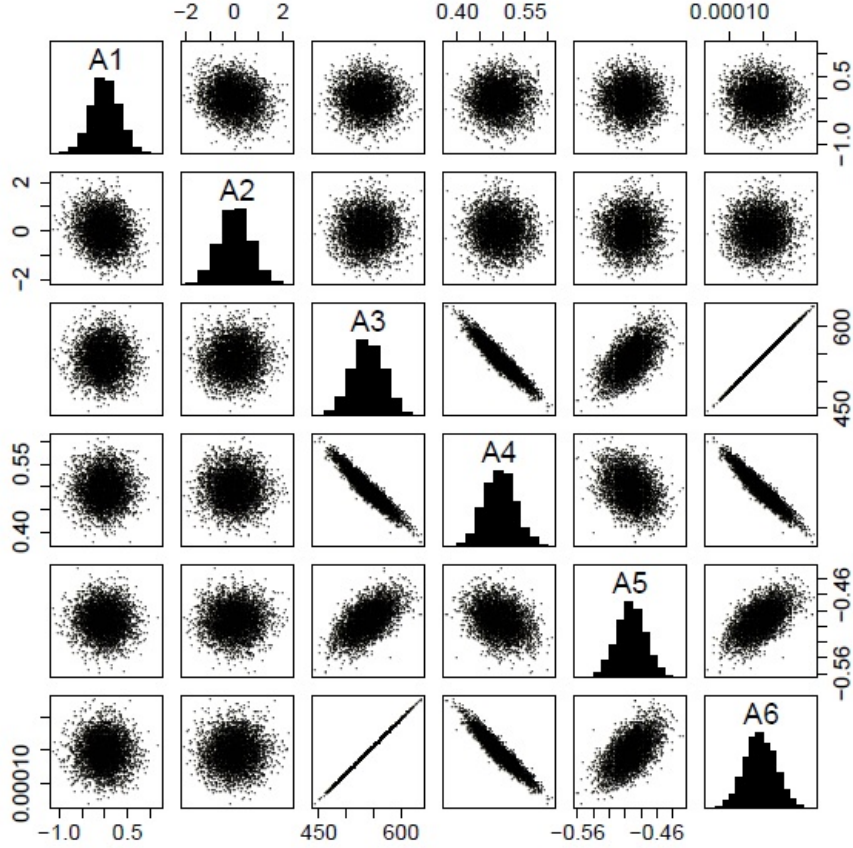


Figure 2.6: **Example 2.2., propagation example, AST-CRTN coordinates.** Propagated point cloud in AST-CRTN coordinates. All the histograms and scatter plots are approximately normal.

$2e^{-16}$) are effectively 0 and indicate the distribution is extremely non-Gaussian.

Table 2.1: Normality test results. Here $p_{\text{skewness}}, p_{\text{kurtosis}}$ represent p-values for the skewness and kurtosis respectively.

Coordinate system/p-value	p_{skewness}	p_{kurtosis}
Cartesian (Fig. 2.3)	$< 2e^{-16}$	$< 2e^{-16}$
Keplerian (Fig. 2.4)	$< 2e^{-16}$	$< 2e^{-16}$
Equinoctial (Fig. 2.5)	$< 2e^{-16}$	$< 2e^{-16}$
AST (Fig. 2.6)	0.07	0.09

2.5 Analyzing the AST-CRTN coordinate system

Note. Note that Mardia's p-value test judges the multivariate normality. In order to judge the univariate normality, we use the Shapiro-Wilk's univariate normality test. The test result confirms that all six AST coordinate elements are approximately univariate normal. However, none of the ECI or Keplerian coordinates are approximately univariate normal and for the Equinoctial coordinate system only E_4 is univariate normal.

Chapter 3

Representing uncertainties associated with the propagated observation vector

3.1 Introduction

The previous chapter discussed the propagated 6-dimensional state vector or the AST-CRTN coordinate system. In this chapter we investigate the behavior of the 2-dimensional state vector or the propagated angles-only uncertainty. The AST-CRTN coordinate system represents the 6-dimensional propagated orbital uncertainty and contains information related to the position and the velocity of an object. However, the “Adapted SPHERical (ASP)” coordinate (ASP-CRTN) system represents the 2-dimensional angles-only position vector (or 3-dimensional, if we add the radial component). It includes information about the position of an object. During the filtering or tracking, the AST-CRTN coordinate system is used to describe the whole 6-dimensional propagated state vector, whereas the ASP-CRTN coordinate system deals with the propagated observation vector (as the observation is measured using the angles-only position). Various features of the propagated angles-only distribution are listed below.

The distribution of the propagated longitude is approximately Gaussian for a small propagation time. As the propagation time increases, the distribution becomes more spread out, eventually wrapping around the circle. It is then better described by the wrapped normal distribution. The distribution of the

3.2 Chapter summary and key contributions

latitude is approximately normal apart from few special cases.

In the case of a break-up (due to a collision) event, where the initial position is known nearly exactly, but the initial velocity shows high uncertainty the joint distribution shows a pronounced “pinching” or “bow-tie” effect in a scatter plot of latitude vs. longitude whenever the propagation time is an integer multiple of the half-period for the initial state. However, this is a special case. This chapter discusses it in details.

The pinching effect starts and ends a little before and after (respectively) the half orbital propagation. In this chapter with the use of weighted sigma points, we compute the approximate pinching duration.

The distribution of the radial component is approximately normally distributed if the propagation time is small. However, if the propagation time is moderate then distribution of the radial component becomes more complicated to work with. We discuss the distribution of the radial component here. In addition, we also provide the conditional distribution of the radial component given the longitude.

3.2 Chapter summary and key contributions

The aim of this chapter is to analyse the uncertainty associated with the angles-only position of the propagated point cloud. Previous chapter showed that the propagated uncertainty in the Cartesian-CRTN coordinate system is non-normal (Section 2.5.3) and suffers from the “banana” effect (Cartesian-ECI coordinate system also suffers from the same effect). Such a distribution is not ideal to work with as it is not possible to use a Kalman filter. Uncertainty represented using the ASP-CRTN coordinate system (or the modified ASP-CRTN coordinate system) is approximately Gaussian. Next, key contributions are summarized below.

- (a) A modified spherical coordinate system (or the spherical coordinate system represented using the CRTN basis), namely the “Adapted Spherical (ASP)” coordinate (ASP-CRTN) system, is introduced in this chapter. Under Keplerian dynamics the propagated angles-only uncertainty can be approximated using a bivariate normal distribution in the ASP-CRTN coordinate

system if the propagation time is not too large and both uncertainties (position and velocity uncertainties at $t = 0$) are present (Section 3.4).

- (b) The transformation from the initial central state to the propagated deviated state is presented using the analytic derivation. The analytic expansion shows that for a break-up event (i.e., uncertainty in position is zero) if the propagation period is close to a multiple of half central orbital period then the propagated uncertainty represented using the ASP-CRTN coordinate system suffers from the “pinching” effect. However, the conditional distribution of the latitude given the longitude is approximate normal (Sections 3.5 and 3.6).

Note that during the break-up event, a single object splits into many objects. The individual objects initially lie at the same position, but move apart with different velocity vectors.

- (c) We use weighted *velocity-only* sigma points to compute the approximate pinching duration (Section 3.7).
- (d) The final portion of this chapter discusses the distribution of the radial component (Section 3.9).

3.3 Relation to other chapters

This chapter discusses the ASP-CRTN coordinate system. The ASP-CRTN coordinate system can be constructed in several ways, such as, from the AST-CRTN (t) coordinate system or from the Cartesian-CRTN (t) coordinate system (or other 6-dimensional coordinate systems). Information related to the Cartesian-ECI/CRTN coordinate system and the AST-CRTN coordinate system can be found in Chapters 1 and 2. In this thesis, we use the ASP-CRTN coordinate system to discuss the break-up event. Further, we also use the ASP-CRTN coordinate system to solve various association problems (Chapter 6).

- (a) **Construction of the ASP-CRTN coordinate system using the AST-CRTN (t) coordinate system** (see Equations (3.11) and (3.12) to un-

3.4 The ASP-CRTN coordinate system

derstand the relation between the AST-CRTN (t) system and the ASP-CRTN(t) system).

$$\text{Cartesian-ECI}(0) \longrightarrow \text{Cartesian-CRTN}(0) \longrightarrow \text{AST-CRTN}(t) \longrightarrow \text{ASP-CRTN}(t).$$

- (b) **Construction of the ASP-CRTN coordinate system using the Cartesian-CRTN (t) coordinate system.**

$$\begin{aligned} \text{Cartesian-ECI}(0) &\longrightarrow \text{Cartesian-CRTN}(0) \longrightarrow \text{Cartesian-CRTN}(t)^* \\ &^* \longrightarrow \mathbf{r}(t), \text{ (unit-vector) CRTN-position}(t) \longrightarrow \text{ASP-CRTN}(t). \end{aligned}$$

3.4 The ASP-CRTN coordinate system

The formation of the ASP-CRTN coordinate system is mentioned below. Note that the central-state is represented using the CRTN reference basis and as mentioned before, the ASP-CRTN coordinate system is actually the spherical representation a state (position) of an orbiting object using the CRTN basis.

- (1) Recall Section 1.8.1, the central state (Cartesian-CRTN) in the CRTN reference basis takes the following form,

$$\mathbf{x}^{\text{CRTN}(c)}(0) = \begin{bmatrix} A \\ 0 \\ 0 \end{bmatrix} \quad (3.1)$$

$$\dot{\mathbf{x}}^{\text{CRTN}(c)}(0) = \begin{bmatrix} B \\ C \\ 0 \end{bmatrix}. \quad (3.2)$$

Further, the deviated states can be represented in terms of departures from the central state,

$$\mathbf{x}^{\text{CRTN}}(0) = \mathbf{x}^{\text{CRTN}(d)}(0) = \begin{bmatrix} A + \epsilon_1 \\ \epsilon_2 \\ \epsilon_3 \end{bmatrix} \quad (3.3)$$

$$\dot{\mathbf{x}}^{\text{CRTN}}(0) = \dot{\mathbf{x}}^{\text{CRTN}(d)}(0) = \begin{bmatrix} B + \delta_1 \\ C + \delta_2 \\ \delta_3 \end{bmatrix}. \quad (3.4)$$

3.4 The ASP-CRTN coordinate system

- (2) Propagate the point cloud using Keplerian dynamics.
- (3) Let $\mathbf{x}^{\text{CRTN-unit}}(t) = \mathbf{x}^{\text{CRTN}}(t)/|\mathbf{x}^{\text{CRTN}}(t)|$, $j = 1, \dots, N$ denote the projections of the positions of the point cloud on the unit sphere.
- (4) Spherical coordinates for a vector $\mathbf{x}^{\text{CRTN-unit}} = [x_1^{\text{CRTN-unit}}, x_2^{\text{CRTN-unit}}, x_3^{\text{CRTN-unit}}]^T$ can be written in terms of the unit vector by

$$x_1^{\text{CRTN-unit}}(t) = \cos \psi(t) \cos \theta(t), \quad x_2^{\text{CRTN-unit}}(t) = \cos \psi(t) \sin \theta(t), \quad x_3^{\text{CRTN-unit}}(t) = \sin \psi(t). \quad (3.5)$$

Here $\psi(t)$ (equivalent to $\psi^{\text{CRTN}}(t) \in [-\pi/2, \pi/2]$) denotes the “latitude”, $\theta(t)$ (equivalent to $\theta^{\text{CRTN}}(t) \in [-\pi, \pi]$) is the “longitude”, and $[0, 0, 1]^T$ points towards the “north pole” or “central normal direction” in the unit sphere. In these coordinates, $\psi = 0$, $\theta = 0$, corresponds to the intersection of the “prime meridian” and the “equator” in the unit sphere.

- (5) Finally, plot the data, $\psi(t)$ vs. $[\theta(t) - \theta^{(c)}(t)]$ for various t . The reason for using these spherical (or spherical like) coordinates is that the banana-shape in Euclidean coordinates turns into an approximate bivariate normal in the ASP-CRTN coordinate system. Note that $[\theta(t) - \theta^{(c)}(t)]$ (treated as an angle) is used to center the propagated central state at the (0,0) location.

Note. In this chapter $\psi(t)$ and $\theta(t)$ are same as $\psi^{\text{CRTN}}(t)$ and $\theta^{\text{CRTN}}(t)$ respectively.

3.4.1 Example 3.1., distribution of the propagated angles-only elements

The purpose of the example is to illustrate the usefulness of the ASP-CRTN coordinate system. Consider an orbital object (“central state”) with eccentricity = 0.13, orbital period = 131.013 minutes and true anomaly measured from the perigee = 99.41° (with A = 8582 km, B = 0.88 km/sec and C = 6.74 km/sec). Further, initial uncertainties are $P_\sigma = 1\%$ for Cartesian-CRTN position elements and

3.4 The ASP-CRTN coordinate system

$P_\tau = 1\%$ for Cartesian-CRTN velocity elements. The point cloud has been propagated for 1 central orbital period. Final angles-only positions are summarized in Fig. 3.1. Notice that both the longitude and the latitude are approximately univariate normal and their joint distribution is approximately bivariate normal. Further, the approximate normality can be confirmed using p-values obtained using Mardia's p-value test. In this set-up p-values are 0.09 for the skewness and 0.95 for the kurtosis using Mardia's tests. Note that since $e = 0.13$, the function F_{M-t_0-T} (Section 1.7.3) is almost linear (also see A.7, this plot describes the relationship between the true anomaly and the mean anomaly for different eccentricity values).

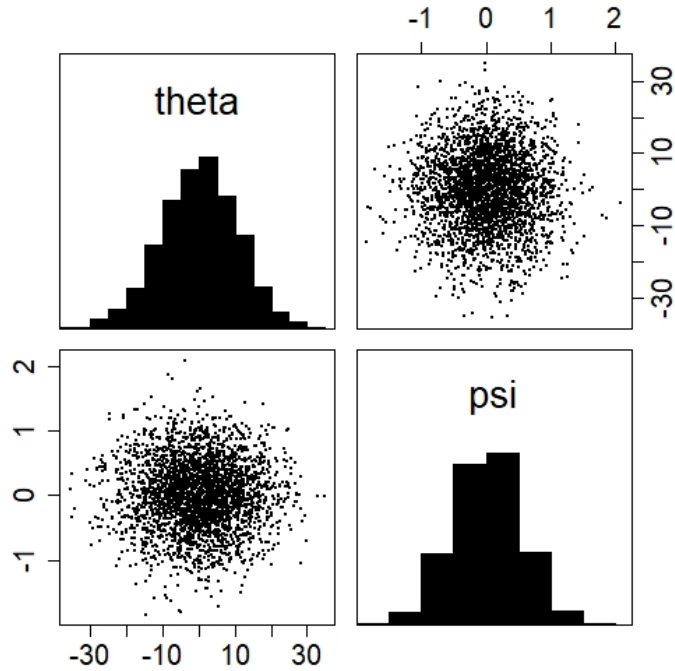


Figure 3.1: **Example 3.1., propagated angles-only components.** Propagated angles-only elements. Note that the joint distribution of the longitude and the latitude can be approximated using a bivariate normal distribution. Initial conditions are mentioned in Section 3.4.1.

Note. Note that if the eccentricity (central eccentricity) is small and the

3.5 Uncertainty representation for the ASP-CRTN coordinate

propagation period is not extreme then $[\theta - \theta^{(c)}] \approx [\phi - \phi^{(c)}]$. Further, under such circumstances the distribution of the $\theta(t)$ or $\theta - \theta^{(c)}$ is approximately normal. Since e (or $e^{(c)}$) is small, the choice of θ or ϕ makes almost no difference in terms of normality assessment. Appendix (Section A.2) lists more propagation examples, where we show behavior of various angles under propagation based on orbital eccentricity and period. In addition, Section 3.6 summarizes various angular components used in this thesis.

3.5 Uncertainty representation for the ASP-CRTN coordinate

From the previous chapter (Section 2.5.1), the Jacobian matrix for converting the Cartesian-CRTN to the AST-CRTN coordinate system $\mathbf{J} = \partial(\text{AST-CRTN})/\partial(\text{Cartesian-CRTN}^T)$ (at time $t = 0$) takes the form,

$$\mathbf{J} = \begin{array}{ccccccc} & \epsilon_1 & \epsilon_2 & \epsilon_3 & \delta_1 & \delta_2 & \delta_3 & \\ \left[\begin{array}{ccccccc} 0 & 0 & -B/AC & 0 & 0 & 0 & 1/C \\ 0 & 0 & -1/A & 0 & 0 & 0 & 0 \\ 0 & D^{\text{coeff}}/A & 0 & 0 & 0 & 0 & 0 \\ C^2/\mu - 1/A & -BC/\mu & 0 & 0 & 2AC/\mu & 0 & 0 \\ -BC/\mu & B^2/\mu - 1/A & 0 & -AC/\mu & -AB/\mu & 0 & 0 \\ P_1C + P_2Q_1 & -P_1B + P_2Q_2 & 0 & P_1A + 2P_2A^2BC^2 & P_2Q_3 & 0 & 0 \end{array} \right] & \begin{array}{l} A1 \\ A2 \\ A3 \\ A4 \\ A5 \\ A6 \end{array} \end{array}$$

The latitude can be written as (see Chapter 1, Equation (1.28)),

$$\begin{aligned} \psi(t) &\approx \sin(i) \sin(\theta(t) - \Omega) \\ &\approx i \sin \theta(t) \cos \Omega - i \cos \theta(t) \sin \Omega \\ &\approx A_1 \sin \theta(t) - A_2 \cos \theta(t). \end{aligned} \tag{3.6}$$

Note. All these angles ($\psi(t)$, i , $\theta(t)$, Ω) are defined with respect to the CRTN basis.

In this setting three scenarios are possible. Note that (a) and (b) are special cases.

3.5 Uncertainty representation for the ASP-CRTN coordinate

(a) (Break-up event) If $\sigma^2 = 0$ so that ϵ vanishes, then

$$\psi(t) \approx (\delta_3/C) \sin \theta(t). \quad (3.7)$$

At the break-up time, a single object splits into many objects. The individual objects initially lie at the same position, but move apart with different velocity vectors.

(b) The opposite situation is perhaps mainly of mathematical interest. If $\tau^2 = 0$ so that δ vanishes, then

$$\begin{aligned} \psi(t) &\approx (-\epsilon_3 B/(AC)) \sin \theta(t) - (-\epsilon_3/A) \cos \theta(t) \\ &\approx (\epsilon_3/A) \cos \theta(t) + [-\epsilon_3 B/(AC)] \sin \theta(t). \end{aligned} \quad (3.8)$$

(c) Finally, when both $\sigma^2 > 0$ and $\tau^2 > 0$, then

$$\psi(t) \approx (\epsilon_3/A) \cos \theta(t) + [-\epsilon_3 B/(AC) + \delta_3/C] \sin \theta(t). \quad (3.9)$$

3.5.1 Propagated angles-only positions during break-up event

Example 3.2., part 1. Consider the same object which was considered previously in Example 3.1., the initial position of the object is known exactly ($\sigma^2 = 0$, $\epsilon = \mathbf{0}$) and the initial velocity is normally distributed with standard deviation $P_\tau = 1\%$ in each direction. Further, the uncertainties in all 3 velocity coordinates are independent. The state of the object has been propagated for various time intervals and propagated angles-only positions are summarized in Fig. 3.2.

Fig. 3.2 shows various stages of the pinching. First, the plot located at the upper-left panel (say, (a)) indicates the joint distribution of the latitude and the longitude when propagation time is 0.8 central orbital periods. Note that the joint distribution is approximately a bivariate normal. Second, the plot located at the upper-right panel (say, (b)) exhibits the propagated point cloud after 0.98 central orbital periods. The pinching behavior is visible here. Third, the plot located at the lower-left panel (say, (c)) displays the point cloud exactly after 1 central orbital period and the “bow-tie” pattern is clearly visible here. Finally, the last plot (say, (d)) shows the propagated point cloud after 1.02 orbital periods. The pinching effect is still visible in this plot.

3.5 Uncertainty representation for the ASP-CRTN coordinate

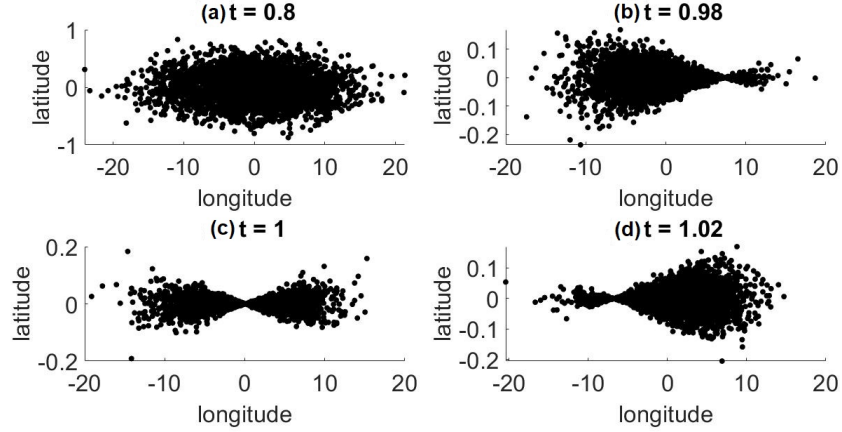


Figure 3.2: **Example 3.2., pinching example, part 1.** Angles-only part of the propagated point cloud has been shown for various propagation times (much before, just before, during and just after pinching). Subplot (a) highlights a scenario which is much before the pinching. The propagation period is 0.8 central orbital period. The joint distribution is approximately *bivariate normal*. Subplot (b) shows the angles-part *just before* the pinching behavior and the propagation period is 0.98 central orbital period. Subplot (c) illustrates the *exact pinching* behavior, a “bow-tie” or “butterfly” pattern is clearly visible here. Finally, Subplot (d) displays the propagated point cloud *just after* the pinching. Note that (b), (c) and (d) are not bivariate normal.

3.5.2 Treating the pinching problem and the Pinched-Normal distribution

The distribution of $(\psi(t), \theta(t))$ during a break-up event can be turned into a bivariate normal distribution by re-scaling the latitude $\psi(t)$ to

$$\psi_1(t) = \psi(t) \left[\frac{C}{(\sin \theta(t) \sigma_{\delta_3})} \right] \quad (3.10)$$

and by transforming from $\theta(t)$ on the true anomaly scale to $\phi(t)$ on the mean anomaly scale. Then $(\psi_1(t), \phi(t))$ follows a bivariate normal distribution with independent components (for a break-up event $\phi(t) = \phi(0) + nt = f(\delta_1, \delta_2)$). We describe the distribution of the $(\psi_1(t), \phi(t))$ as the “*Pinched-Normal (PN)*” distribution. As mentioned before, if e is small then the choice of θ or ϕ makes very little difference ($f(\psi_1(t), \phi(t)) \approx f(\psi_1(t), \theta(t))$). In Equation (3.10) σ_{δ_3} denotes

3.6 A brief summary based on the behavior of various propagated angles

the standard deviation associated with the δ_3 deviation.

Example 3.2., treating the pinching, part 2. In Fig. 3.3, the first element is the longitude $\theta(t)$, the second element is the original latitude $\psi(t)$ and the final element is re-scaled/standardized latitude $\psi_1(t)$ (with mean 0 and standard deviation 1). The initial conditions are kept same as Fig. 3.2 and the propagation time is exactly 1 central orbital period (same as Fig. 3.2, Subplot (c)). Since the central eccentricity $e^{(c)}$ and the propagation period are small, $\theta(t) \approx \phi(t)$.

The resulting point cloud (joint distribution of θ and ψ_1) can be tested for approximately normality using Mardia's multivariate normality test. The resulting p-values are 0.09 (for the skewness) and 0.52 (for the kurtosis) indicating no incompatibility with the Gaussian distribution.

3.6 A brief summary based on the behavior of various propagated angles

- (1) *True angles.* The term “True angles” indicates the latitude (ψ) and the longitude (θ). These two propagated angles provide information related to the observation angles. The term “True” also means that these two angles are *real* and directly related to the observation vector (or observed angles, observed latitude and longitude). Note that if the measurement error is 0 then true and observation angles are exactly the same. Typically true angles are unknown but with a well-specified propagated distribution. However, observation angles are distributed about the true values with measurement errors.
 - (a) *Distribution of the latitude.* Compared to the longitude, the distribution of the latitude is typically much more tightly concentrated. In addition, the distribution of the latitude is generally approximately normal apart from a break-up event.
 - (b) *Distribution of the longitude.* If the propagation period is small/moderate and orbital eccentricity is not huge then the distribution of the longitude is approximately normal or wrap-normal (becomes normal if we

3.6 A brief summary based on the behavior of various propagated angles

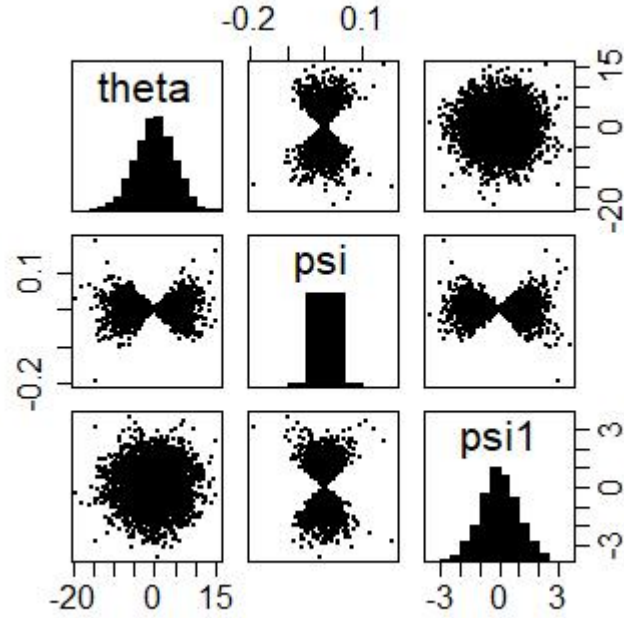


Figure 3.3: **Example 3.2., pinch-corrected distribution, part 2.** The first element is the longitude, the second and third elements are original and scaled/standardized latitudes respectively. The joint distribution of the longitude (θ) and the scaled latitude (ψ_1) can be approximated using a bivariate normal distribution. The initial conditions are same as Fig. 3.2 and the propagation time is exactly 1 central orbital period, as in Fig. 3.2, Subplot (c).

use the correct winding number). However, if initial uncertainties are huge and/or propagation period is large and the orbital eccentricity is high then the distribution of the unwrapped longitude cannot be approximated using a normal distribution. See Appendix, Section A.2, for an example.

- (2) *Pseudo true angles.* The term “Pseudo true angles” refers to the ϕ or the modified break-angle (re-invented) and ψ_1 or the standardized latitude. These two angles are not real (they are artificial, that’s why the term “pseudo” is used) but they are developed to deal with the non-normal

3.6 A brief summary based on the behavior of various propagated angles

behavior of the propagated true angles or distributions related to the propagated true angles (θ and ψ).

- (a) *Distribution of the standardized latitude.* The standardized latitude is (*always*) approximately normal with mean 0 and standard deviation (s.d.) 1.
- (b) *Distribution of the modified/re-invented break-angle.* The distribution of ϕ is also (*always*) approximately normal.

For solving space object tracking or association problems, the propagation period is typically not huge and uncertainties are not extreme ($< 1\%$ for both) and the use of θ is justified as under such conditions θ is approximately a univariate normal. However, to deal with non-normal uncertainty generated due to a break-up event, we need to use ψ_1 or the standardized latitude, see Sections 6.8.2 and 6.8.3 (Chapter 6) for examples. However, if the propagation period is large and the orbital uncertainty is also not small then it is recommended to use (ψ, ϕ) or (ψ_1, ϕ) in place of (ψ, θ) .

The AST coordinate system was discussed in Chapter 2. Next, a brief discussion is provided to show the relation between AST coordinate elements and true angles (discussed earlier this section). Recall Chapter 1, Equation (1.28),

$$\begin{aligned}\theta(t) &= \Omega + \omega + T(t) = \theta_p + T(t) = \text{atan2}(A_5, A_4) + T(t) \\ &= \text{atan2}(A_5, A_4) + F_{\text{M-to-T}} \left(A_3(t) - \phi_p, \sqrt{A_4^2 + A_5^2} \right) \\ &= \text{atan2}(A_5, A_4) + F_{\text{M-to-T}} \left(A_3(t) - L_3, \sqrt{A_4^2 + A_5^2} \right)\end{aligned}\quad (3.11)$$

$$\psi(t) = \sin(i) \sin(\omega + T(t)) = \sin^{-1}(\sin(L_1) \sin(L_2(t))), \quad (3.12)$$

where,

$$\begin{aligned}L_1 &= 2 \tan^{-1} \left(\frac{\sqrt{A_1^2 + A_2^2}}{2} \right), \\ L_2(t) &= F_{\text{M-to-T}} \left(A_3(t), \sqrt{A_4^2 + A_5^2} \right) - \text{atan2}(A_2, A_1), \\ L_3 &= F_{\text{T-to-M}} \left(\text{atan2}(A_5, A_4), \sqrt{A_4^2 + A_5^2} \right).\end{aligned}$$

3.7 Velocity-only sigma points for break-up event analysis

- (1) The function F_{M-to-T} (also F_{T-to-M}) is nonlinear, if the orbital eccentricity e is 0 (or small) then it becomes linear and $\theta(t) = \phi(t) = A_3(t)$.
- (2) If $\theta(t)(= \theta)$ is fixed at time t , then we can represent latitude using linear combinations of A_1 and A_2 (Equation 3.6). Further, we can also write,

$$\mathbf{J}_1 = \begin{matrix} & A_1 & A_2 & A_3 & A_4 & A_5 & A_6 \\ \begin{bmatrix} \sin \theta & -\cos \theta & 0 & 0 & 0 & 0 \\ 0 & 0 & 1 & 0 & 0 & 0 \end{bmatrix} & \psi & \cdot & & & & \\ & \phi & & & & & \end{matrix} \quad (3.13)$$

Note that J_1 is a transformation matrix which computes ASP coordinates from AST (or AST-CRTN) coordinates when θ is fixed.

In addition, we can also represent ASP coordinate elements using ϵ and δ terms using (2.3) and (3.14).

- (a) The longitude (modified/re-invented break-angle) can be written as,

$$\begin{aligned} \phi(t) &= \phi(0) + nt \\ &\approx \frac{D^{\text{coeff}} \epsilon_2}{A} + \epsilon_1(P_1C + P_2Q_1) + \epsilon_2(-P_1B + P_2Q_2) \\ &\quad + \epsilon_4(P_1A + 2P_2A^2BC^2) + (P_2Q_3)\epsilon_5 \\ &\approx \epsilon_1(P_1C + P_2Q_1) + \epsilon_2(-P_1B + P_2Q_2 + \frac{D^{\text{coeff}}}{A}) \\ &\quad + \epsilon_4(P_1A + 2P_2A^2BC^2) + \epsilon_5(P_2Q_3). \end{aligned}$$

- (b) The latitude can be written as,

$$\begin{aligned} \psi(t) &\approx (\epsilon_3/A) \cos \theta(t) + [-\epsilon_3B/(AC) + \delta_3/C] \sin \theta(t) \\ &\approx \epsilon_3 \left(\frac{\cos \theta(t)}{A} - \frac{B \sin \theta(t)}{AC} \right) + \delta_3 \left(\frac{\sin \theta(t)}{C} \right). \end{aligned}$$

3.7 Velocity-only sigma points for break-up event analysis

In order to study the propagated orbital uncertainty in a more idealized form for a break-up event, it is helpful to use a small set of carefully selected deviated

3.7 Velocity-only sigma points for break-up event analysis

initial points. We represent the point cloud using seven ($N = 2l + 1 = 7$, l is the dimension and $l = 3$ for a velocity-only uncertainty analysis, $\epsilon = 0$) carefully chosen velocity-only sigma points which can mimic the point cloud behavior both qualitatively and quantitatively. Further, the point cloud based uncertainty propagation method can be computationally expensive but sigma points based propagation method is much faster. Basically, sigma points are the discrete approximation of the point cloud. Note that the concept of using a sigma points based system to represent the propagated orbital uncertainty is motivated by the UKF sigma points (see Chapter 4 for more details).

Recall Section 3.5, if $\epsilon = \mathbf{0}$, then a deviated state can be represented in the Cartesian-CRTN coordinate system as,

$$\mathbf{x}^{\text{CRTN}(d)}(0) = \mathbf{x}^{\text{CRTN}(c)}(0) = \begin{bmatrix} A \\ 0 \\ 0 \end{bmatrix}, \quad \dot{\mathbf{x}}^{\text{CRTN}(d)}(0) = \begin{bmatrix} B + \delta_1 \\ C + \delta_2 \\ \delta_3 \end{bmatrix}. \quad (3.14)$$

Consider 6 perturbation vectors for the velocity, $\pm\tau_1\mathbf{e}_1$, $\pm\tau_1\mathbf{e}_2$, $\pm\tau_1\mathbf{e}_3$, where,

$$\mathbf{e}_1 = \begin{bmatrix} 1 \\ 0 \\ 0 \end{bmatrix}, \quad \mathbf{e}_2 = \begin{bmatrix} 0 \\ 1 \\ 0 \end{bmatrix}, \quad \text{and} \quad \mathbf{e}_3 = \begin{bmatrix} 0 \\ 0 \\ 1 \end{bmatrix}$$

denote three coordinate axes.

Label the deviated initial conditions by $\pm\tau_1\mathbf{e}_1$, $\pm\tau_1\mathbf{e}_2$, $\pm\tau_1\mathbf{e}_3$, respectively, giving a collection of $N = 7$ ($N =$ total number of data points) initial conditions.

The perturbations $\pm\tau_1\mathbf{e}_1$ lie in the “radial” direction, $\pm\tau_1\mathbf{e}_2$ lie in the “in-track” direction, and $\pm\tau_1\mathbf{e}_3$ lie perpendicular to these directions, i.e the “cross-track” direction.

The perturbations $\pm\tau_1\mathbf{e}_2$ mainly affect the period of the orbit. Similarly, the perturbations $\pm\tau_1\mathbf{e}_3$ mainly affect the direction of the orbit but not its period.

3.7.1 Sigma points propagation

Example 3.3. To illustrate the use of sigma points, consider the same setting as in Examples 3.1. and the propagation period is 0.8 central orbital period.

3.7 Velocity-only sigma points for break-up event analysis

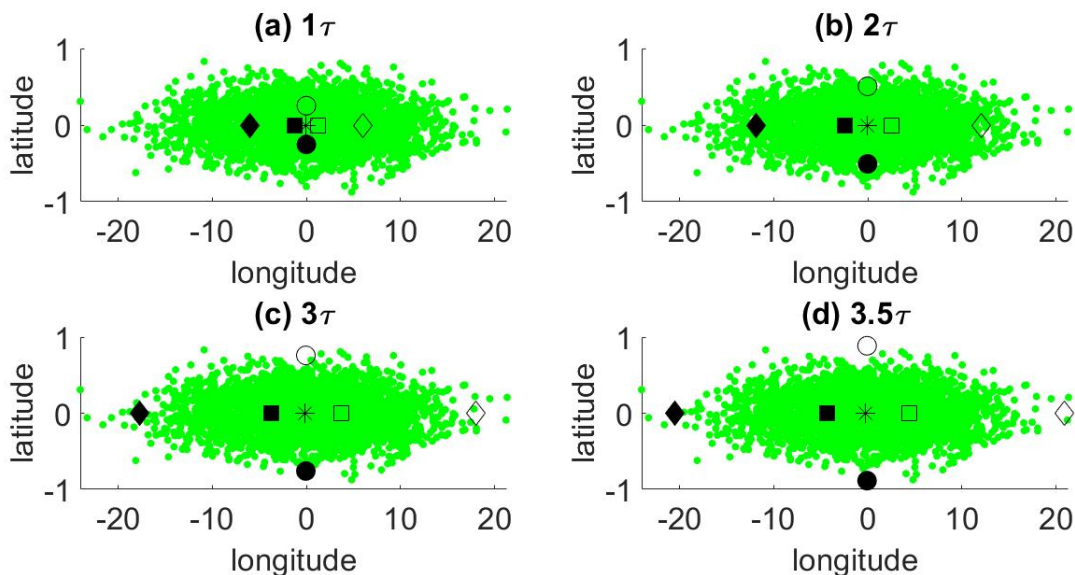


Figure 3.4: **Example 3.3., sigma points propagation.** Illustration of sigma points after 0.8 central orbital periods (for $\tau_1 = 1, 2, 3$ and 3.5τ respectively). The data are plotted in ASP-CRTN coordinates with the “latitude” $\psi(t)$ and the “longitude” ($[\theta(t) - \theta^{(c)}(t)]$) in degrees. Here, * denotes the base point; squares denote the $\pm\tau_1\mathbf{e}_1$ sigma points, diamonds denote the $\pm\tau_1\mathbf{e}_2$ sigma points, and circles denote the $\pm\tau_1\mathbf{e}_3$ sigma points. Plus perturbations are indicated by an open symbol; minus perturbations by a closed symbol.

Fig. 3.4 (Example 3.4.) describes four scenarios for different values of sigma. From these examples, we can conclude that $\tau_1 = 3.5\tau$ is a sensible choice (scales are approximately same for both the latitude and the longitude for the sigma points based system and a propagated point cloud).

3.7.2 Limitations of Velocity-only sigma points based system

Sigma points (or velocity-only sigma points, these two terms are used interchangeably in this chapter) and a point cloud behave in a similar way for orbital uncertainty representation under certain circumstances (see the previous example). This section describes a situation where sigma points are unable to mimic a point cloud.

The main intention behind developing the sigma points is to provide a discrete approximation of distributions of the two angular components (the latitude and the longitude) of the propagated point cloud. Further, using a sigma points based system is a sensible choice if both the latitude and the longitude are univariate normal and their joint distribution is a bivariate normal. However, if the joint distribution is non-normal then sigma points fail to replicate the point cloud. Consider an example where the error variances describe a break-up event and where the propagation time is a multiple of a half orbital period, the propagated angular distribution displays a “bow-tie” or “pinching” pattern in the ASP-CRTN coordinate system for a point cloud (Example 3.2., Fig. 3.2). As discussed earlier, the distribution of the latitude (for a point cloud during a pinching event) is not normal and sigma points fail to approximate the joint distribution (as the joint distribution is not a bivariate normal), see Fig. 3.5 for more details.

Example 3.4. Consider the same orbital object which we considered previously in Example 3.1. In this example, we propagate velocity-only sigma points for exactly 1 central orbital period and plot the propagated angles-only components in ASP-CRTN coordinates. As expected, the angles-only part of the propagated point cloud shows a “pinching” pattern and sigma points are unable to capture this feature both quantitatively and qualitatively (Fig. 3.5).

To summarize, during a break-up event, the distribution (for point cloud propagation) of the longitude is approximately normal but the the distribution (for point cloud propagation) of the latitude is non-normal and the joint distribution is also not a bivariate normal. As a result, sigma points are unable to approximate the point cloud properly.

3.8 Application of Sigma points

If the propagation time is moderate and not close to a multiple of half orbital period then sigma points are very similar to a point cloud based system for representing the propagated angular position. However, if the propagation period is close to a multiple of half orbital period, then sigma points are unable to mimic the propagated point cloud. Our velocity-only sigma points can be used for

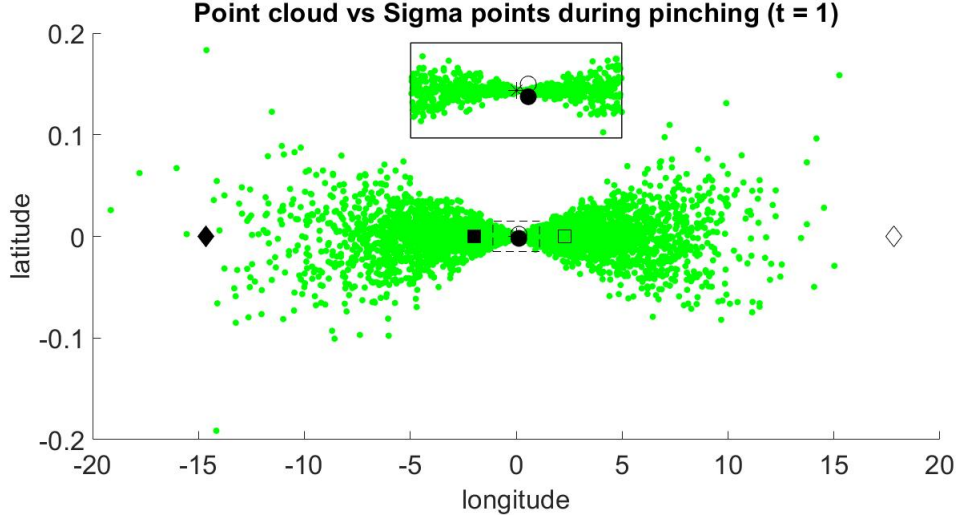


Figure 3.5: **Example 3.4., sigma points during a pinching event.** Representation of sigma points during a pinching event. Clearly, scales for the longitude are approximately same (or close) in both the point cloud and sigma points. However, sigma points are unable to mimic the point cloud behavior for the latitude. The rectangle located just above the pinching location is the zoomed in version of the small (dashed) rectangle situated exactly at the center of the image.

computing the approximate pinching duration and the next subsection provides a detailed description.

3.8.1 Computing the pinching time span

Recall the pinching scenario mentioned using the Fig. 3.2, the pinching effect is maximum during the multiple of the half orbital period but pinching starts and ends a little before and a little after the multiple of half orbital period respectively. This portion of the chapter aims to compute the approximate duration of the pinching with 99.95% confidence intervals (3.5τ). See Fig. 3.4, it shows that 3.5τ is a sensible choice to a propagated point cloud (during a non break-up event and also initial conditions are not extreme).

Two horizontal sigma states (say, $(\mathbf{x}^{\text{CRTN}(1)}, \dot{\mathbf{x}}^{\text{CRTN}(1)})$ and $(\mathbf{x}^{\text{CRTN}(2)}, \dot{\mathbf{x}}^{\text{CRTN}(2)})$) can be represented using the ASP-CRTN coordinate system as (Sections 3.4 and

3.7),

$$\mathbf{x}^{\text{CRTN}(1)}(0) = \begin{bmatrix} A \\ 0 \\ 0 \end{bmatrix}, \quad \dot{\mathbf{x}}^{\text{CRTN}(1)}(0) = \begin{bmatrix} B \\ C + \tau_1 e_2 \\ 0 \end{bmatrix}, \quad (3.15)$$

$$\mathbf{x}^{\text{CRTN}(2)}(0) = \begin{bmatrix} A \\ 0 \\ 0 \end{bmatrix}, \quad \dot{\mathbf{x}}^{\text{CRTN}(2)}(0) = \begin{bmatrix} B \\ C - \tau_1 e_2 \\ 0 \end{bmatrix}. \quad (3.16)$$

Since $\boldsymbol{\epsilon} = \mathbf{0}$, $\mathbf{x}^{\text{CRTN}(1)}(0) = \mathbf{x}^{\text{CRTN}(2)}(0)$. Further, by combining 3.15 and 3.16, we can write,

$$\mathbf{x}^{\text{CRTN}(l)}(0) = \begin{bmatrix} A \\ 0 \\ 0 \end{bmatrix}, \quad \dot{\mathbf{x}}^{\text{CRTN}(l)}(0) = \begin{bmatrix} B \\ C \pm \tau_1 e_2 \\ 0 \end{bmatrix} = \begin{bmatrix} B \\ C_l \\ 0 \end{bmatrix} \quad l = 1, 2, \quad (3.17)$$

where, $\tau_1 = 3.5\tau$.

Now we compute various orbital elements (using the formulas mentioned in Chapter 1, Section 1.7.3) for these two states. The angular momentum vector can be expressed as,

$$\mathbf{h}_l = \begin{bmatrix} 0 \\ 0 \\ AC_l \end{bmatrix}, \quad (3.18)$$

with squared norm,

$$h_l^2 = A^2 C_l^2. \quad (3.19)$$

The expression for the eccentricity vector \mathbf{e}_l simplifies to

$$\mathbf{e}_l = \frac{1}{\mu} \begin{bmatrix} AC_l^2 - \mu \\ -ABC_l \\ 0 \end{bmatrix}. \quad (3.20)$$

From \mathbf{e} , we can compute its squared norm,

$$e_l^2 = \frac{1}{\mu^2} \{ (AC_l^2 - \mu)^2 + (ABC_l)^2 \}. \quad (3.21)$$

3.8 Application of Sigma points

Then the length of the major axis can be computed as (by combining 3.19 and 3.21),

$$\begin{aligned}
 a_l &= \frac{h_l^2}{\mu} \frac{1}{1 - e_l^2} \\
 &= -\frac{A^2 C_l^2}{\frac{A^2 B^2 C_l^2}{\mu} + \frac{A^2 C_l^4}{\mu} - 2AC_l^2} \\
 &= \frac{A\mu}{2\mu - AB^2 - AC_l^2}, \tag{3.22}
 \end{aligned}$$

where, μ is the gravitational constant (see Chapter 1).

Now, assume that two sigma points take $\square p_1$ and $\square p_2$ times to finish a full orbit (orbital period) respectively, then the approximate pinching time span ($\Delta\square p$) can be written as, $\Delta\square p = \square p_2 - \square p_1$,

Further, from (1.7.3) an orbital period can be written as, $(\square p) = \frac{2\pi}{\sqrt{\mu}} a^{\frac{3}{2}}$. Then,

$$\square p_1 = \frac{2\pi}{\sqrt{\mu}} a_1^{\frac{3}{2}}, \quad \square p_2 = \frac{2\pi}{\sqrt{\mu}} a_2^{\frac{3}{2}}. \tag{3.23}$$

The pinching duration (say, $\Delta\square p$) can be computed analytically as follows (from 3.22 and 3.23),

$$\begin{aligned}
 \Delta\square p &= \square p_2 - \square p_1 \\
 &= \left(\frac{2\pi}{\sqrt{\mu}} \right) \left(a_2^{\frac{3}{2}} - a_1^{\frac{3}{2}} \right). \tag{3.24}
 \end{aligned}$$

Further, the variable part of $\Delta\square p$ can be analytically written as,

$$\begin{aligned}
 a_2^{\frac{3}{2}} - a_1^{\frac{3}{2}} &= \left(\frac{A\mu}{2\mu - AB^2 - AC_2^2} \right)^{\frac{3}{2}} - \left(\frac{A\mu}{2\mu - AB^2 - AC_1^2} \right)^{\frac{3}{2}} \\
 &= (A\mu)^{\frac{3}{2}} \left[\left(\frac{1}{2\mu - AB^2 - AC_2^2} \right)^{\frac{3}{2}} - \left(\frac{1}{2\mu - AB^2 - AC_1^2} \right)^{\frac{3}{2}} \right] \\
 &= \left(\frac{A\mu}{2\mu - AB^2} \right)^{\frac{3}{2}} \left[\left(\frac{1}{1 - \frac{AC_2^2}{2\mu - AB^2}} \right)^{\frac{3}{2}} - \left(\frac{1}{1 - \frac{AC_1^2}{2\mu - AB^2}} \right)^{\frac{3}{2}} \right] \\
 &= \square K \left[\left(\frac{1}{1 - \zeta_2} \right)^{\frac{3}{2}} - \left(\frac{1}{1 - \zeta_1} \right)^{\frac{3}{2}} \right], \tag{3.25}
 \end{aligned}$$

3.9 Distribution of the Radial component

where, (in Equation (3.25)),

$$\square K = \left(\frac{A\mu}{2\mu - AB^2} \right)^{\frac{3}{2}}, \quad \zeta_1 = \frac{AC_1^2}{2\mu - AB^2}, \quad \zeta_2 = \frac{AC_2^2}{2\mu - AB^2}. \quad (3.26)$$

Since the length of the major axis and the orbital period of an orbiting object cannot be negative, we can write,

$$2\mu - AB^2 > AC_1^2, \quad 2\mu - AB^2 > AC_2^2. \quad (3.27)$$

Equation (3.27) indicates that if we increase the uncertainty then the pinching duration also increases.

Fig. 3.6 (Example 3.5.) displays two scenarios (note that again initial conditions are same as in Example 3.1).

- (1) The first image (left) indicates the approximate *beginning* of the pinching. Here, the propagation time is 0.956 central orbital period. The joint distribution of the latitude and longitude is plotted using the spherical coordinate system.
- (2) The second image (right) shows the approximate *end* of the pinching. The propagation time is 1.045 central orbital period. The propagated angular position is represented using the spherical coordinate system.

3.9 Distribution of the Radial component

As of now, we have discussed the distribution of the propagated angles-only vector and showed that the joint distribution of the longitude and the latitude (or standardized latitude) is approximately a bivariate normal. This section discusses the distribution of the propagated radial component (r or $r(t)$).

Example 3.6. uses the same object which was used previously in this chapter. Further, initial uncertainties are same as in Example 3.1.

It can be seen in Fig. 3.7 that if the propagation period is small then the distribution of the radial component can be approximated using a univariate normal distribution (Subplots (a) and (c)) and the starting location has no influence

3.9 Distribution of the Radial component

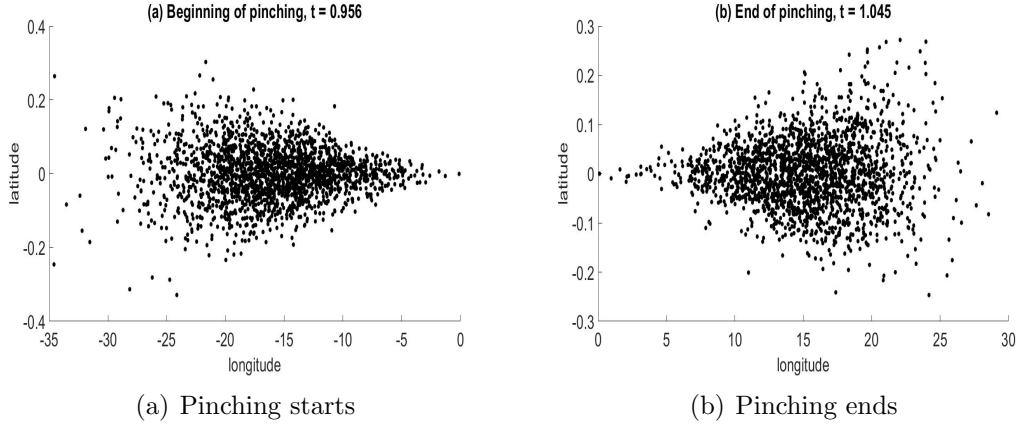


Figure 3.6: **Example 3.5., approximate pinching duration computation.** Subplot (a) indicates the approximate beginning of the pinching effect and Subplot (b) shows the approximate ending of the pinching effect. From this analysis it can be concluded that sigma points works fairly well in computing the pinching duration.

(on the statistical analysis) at all under such set-up. However, if the propagation period is large then the distribution cannot be approximated using a normal distribution.

In this section, we show that the conditional (conditioned on the longitude) distribution of the radial component (standardized radial component) is approximately normal and necessary computation steps are discussed below. Recall Section 1.7.3 (Chapter 1), the radial distance can be written as,

$$r(t) = \frac{h^2}{\mu} \frac{1}{(1 + e \cos T(t))}. \quad (3.28)$$

In Equation (3.28), the radial element is denoted by $r(t)$ (same as r) and the formula given above (3.28) is true for both the central and deviated states. Further in Equation (3.28) only the true anomaly (the true anomaly measured from the perigee, T or $T(t)$) changes with time. From the Chapter 2 (Section 2.5.1), we

3.9 Distribution of the Radial component

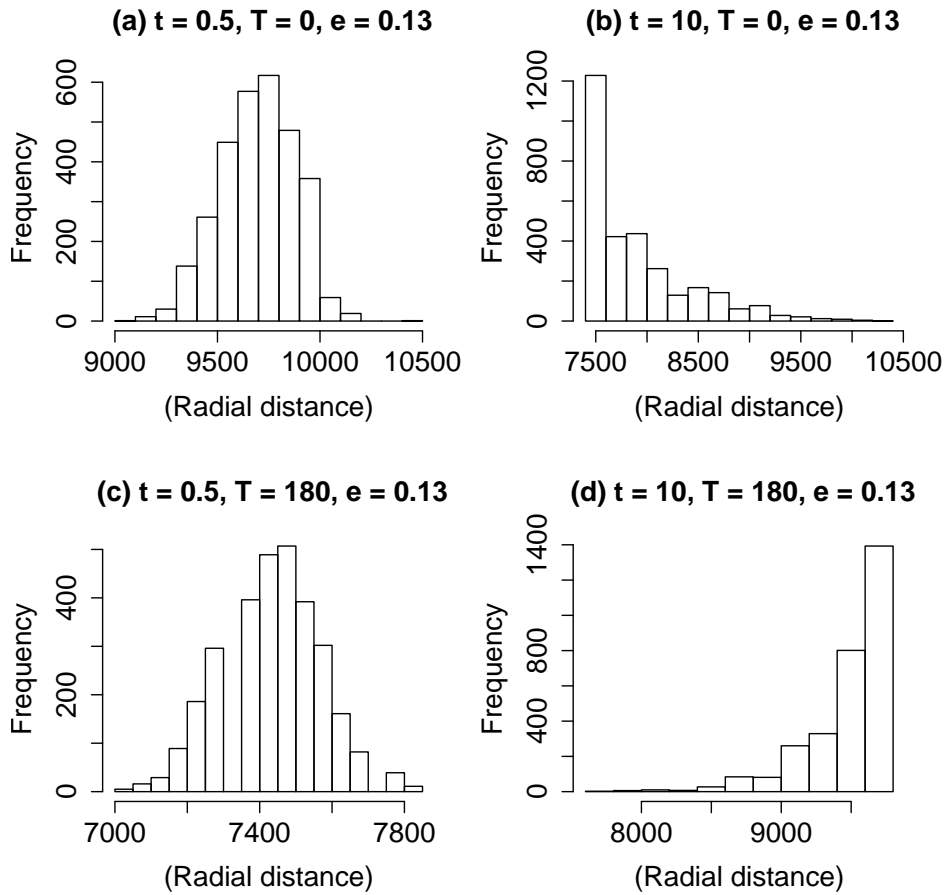


Figure 3.7: **Example 3.6., distribution of the radial component, part 1.** This plot shows distribution of the radial component based on the propagation time and the starting location. The first plot (a) shows the distribution when the starting location is the perigee ($T = 0^\circ$) and the propagation period is small (0.5 central orbital period). Next, plot (b) shows the distribution of the radial component for the same set-up but for a higher number of propagation period (10 central orbital period). For generating plots (c) and (d) we use the same set-up except the starting location is apogee ($T = 180^\circ$).

3.9 Distribution of the Radial component

know that,

$$\begin{aligned}
 h^2 &\approx A^2C^2 + 2AC(A\delta_2 + C\epsilon_1 - B\epsilon_2), \\
 (1 + e \cos T) &= 1 + e \cos(\theta - \theta_p) = 1 + f_1 \cos \theta + f_2 \sin \theta \\
 f_1 &\approx \frac{1}{\mu}(AC^2 + 2\delta_2AC + \epsilon_1C^2 - \epsilon_2BC - \mu - \mu\epsilon_1/A) \\
 f_2 &\approx \frac{1}{\mu}(-ABC - \delta_1AC - \epsilon_1BC - \delta_2AB + \epsilon_2B^2 - \mu\epsilon_2/A). \quad (3.29)
 \end{aligned}$$

Hence, the reciprocal of the radial component can be written as,

$$\begin{aligned}
 \frac{1}{r} &= \frac{\mu}{h^2}(1 + e \cos T) \\
 &\approx \frac{\mu + \mu f_1 \cos \theta + \mu f_2 \sin \theta}{A^2C^2 + 2AC(A\delta_2 + C\epsilon_1 - B\epsilon_2)} \\
 &\approx \frac{\mu + \mu f_1 \cos \theta + \mu f_2 \sin \theta}{A^2C^2[1 + (2\delta_2/C + \epsilon_1/A - B\epsilon_2/AC)]} \\
 &\approx \frac{\mu + \mu f_1 \cos \theta + \mu f_2 \sin \theta}{A^2C^2}(1 - (2\delta_2/C + \epsilon_1/A - B\epsilon_2/AC)) \quad (3.30)
 \end{aligned}$$

Equation (3.30) is computed using the first order Taylor series expansion. Further, from Equation (3.30),

$$\begin{aligned}
 (\mu + \mu f_1 \cos \theta + \mu f_2 \sin \theta) &\approx \mu + (AC^2 - \mu) \cos \theta + (-ABC) \sin \theta \\
 &\quad + (2\delta_2AC + \epsilon_1C^2 - \epsilon_2BC - \mu\epsilon_1/A) \cos \theta \\
 &\quad + (-\delta_1AC - \epsilon_1BC - \delta_2AB + \epsilon_2B^2 - \mu\epsilon_2/A) \sin \theta \quad (3.31)
 \end{aligned}$$

$$= Q_4 + Q_5 \quad (3.32)$$

Let,

$$1 - (2\delta_2/C + \epsilon_1/A - B\epsilon_2/AC) = 1 - Q_6 \quad (3.33)$$

In Equation (3.31) and (3.33),

$$\begin{aligned}
 Q_4 &= \mu + (AC^2 - \mu) \cos \theta + (-ABC) \sin \theta \\
 Q_5 &= (2\delta_2AC + \epsilon_1C^2 - \epsilon_2BC - \mu\epsilon_1/A) \cos \theta \\
 &\quad + (-\delta_1AC - \epsilon_1BC - \delta_2AB + \epsilon_2B^2 - \mu\epsilon_2/A) \sin \theta \\
 Q_6 &= (2\delta_2/C + \epsilon_1/A - B\epsilon_2/AC)
 \end{aligned} \quad (3.34)$$

3.9 Distribution of the Radial component

Note that Q_4 does not depend on ϵ and δ . It only depends on A , B , C and θ . However, both Q_5 and Q_6 depend on ϵ and δ . In addition, by combining (3.32) and (3.33), Equation (3.30) can be written as,

$$\begin{aligned}\frac{1}{r} &= \frac{1}{A^2 C^2} (Q_4 + Q_5)(1 - Q_6) \\ &\approx \frac{1}{A^2 C^2} (Q_4 + Q_5 - Q_4 Q_6)\end{aligned}\quad (3.35)$$

Equation (3.35) ignores $Q_5 Q_6$ as it contains second order expansions of ϵ and δ (too small). Note that one of the major reason behind using the reciprocal of the radial (or deviated radial) component is that the reciprocal can be easily expressed using the first order Taylor series expansion. Further, if h^2 is fixed then r is a linear function of f_1 and f_2 .

Let, $r^{(ic)}$ denotes the analytic expansion of the *inverse* radial component for the central state, it can be written as,

$$r^{(ic)} = [\mu + (AC^2 - \mu) \cos \theta^{(c)} - ABC \sin \theta^{(c)}] \frac{1}{A^2 C^2}, \quad (3.36)$$

where, $r^{(ic)}$ is independent of ϵ and δ terms. However, terms which are dependent on ϵ and δ can be expressed as,

$$r_{\epsilon_1} = \epsilon_1 [(C^2 - \mu/A) \cos \theta + (-BC) \sin \theta - 2Q_4/A] \frac{1}{A^2 C^2} = P_3 \epsilon_1 \quad (3.37)$$

$$r_{\epsilon_2} = \epsilon_2 [(-BC) \cos \theta + (B^2 - \mu/A) \sin \theta + 2Q_4 B/AC] \frac{1}{A^2 C^2} = P_4 \epsilon_2 \quad (3.38)$$

$$r_{\epsilon_3} = \epsilon_3 [0] = 0 \quad (3.39)$$

$$r_{\delta_1} = \delta_1 [-AC \sin \theta] \frac{1}{A^2 C^2} = P_5 \delta_1 \quad (3.40)$$

$$r_{\delta_2} = \delta_2 [-AB \sin \theta + 2AC \cos \theta - 2Q_4/C] \frac{1}{A^2 C^2} = P_6 \delta_2 \quad (3.41)$$

$$r_{\delta_3} = \delta_3 [0] = 0 \quad (3.42)$$

3.9 Distribution of the Radial component

Note that P_3, \dots, P_6 terms are used for the simplification purpose, where,

$$P_3 = [(C^2 - \mu/A) \cos \theta + (-BC) \sin \theta - 2Q_4/A] \frac{1}{A^2 C^2}$$

$$P_4 = [(-BC) \cos \theta + (B^2 - \mu/A) \sin \theta + 2Q_4 B/AC] \frac{1}{A^2 C^2}$$

$$P_5 = [-AC \sin \theta] \frac{1}{A^2 C^2}$$

$$P_6 = [-AB \sin \theta + 2AC \cos \theta - 2Q_4/C] \frac{1}{A^2 C^2}.$$

Note that θ and $\theta^{(d)}$ are the same in this section. Finally, the reciprocal of the radial component (say, $\frac{1}{r} = r^{(id)}$) can be written as,

$$\frac{1}{r} = r^{(id)} = r^{(ic)} + P_3 \epsilon_1 + P_4 \epsilon_2 + P_5 \delta_1 + P_6 \delta_2 \quad (3.43)$$

$$r^{(id-ic)} = r^{(id)} - r^{(ic)} = P_3 \epsilon_1 + P_4 \epsilon_2 + P_5 \delta_1 + P_6 \delta_2 \quad (3.44)$$

In Equation (3.44), $r^{(id-ic)}$ indicates the inverse deviation (containing only ϵ and δ terms). The scaling factor (say, $r^{(sf)}$) can be written as,

$$r^{(sf)} = \sqrt{P_3^2 \Sigma_{\epsilon_1} + P_4^2 \Sigma_{\epsilon_2} + P_5^2 \Sigma_{\delta_1} + P_6^2 \Sigma_{\delta_2}}. \quad (3.45)$$

In Equation (3.45), Σ terms indicate variances associated with various deviations. The inverse scaled-corrected/standardized distribution (say, $r^{(isc)}$) $r^{(isc)} = \frac{r^{(id-ic)}}{r^{(sf)}}$ is approximately normal (See Fig 3.9). Next several examples are provided. Fig. 3.8 shows the distribution of the inverse radial component with initial conditions are exactly the same as in Fig. 3.7. In Fig. 3.9 all the *scaled* inverse radial components are approximately normal, irrespective of the propagation time and the initial starting location.

3.9 Distribution of the Radial component

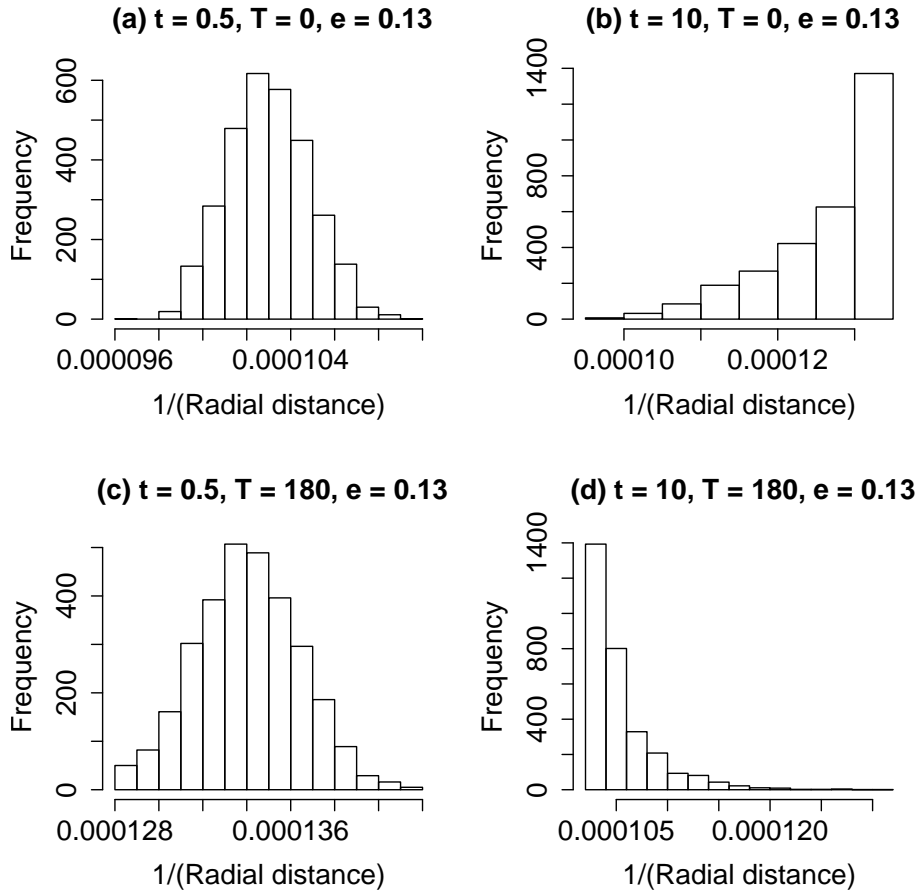


Figure 3.8: **Example 3.6., distribution of the inverse radial component, part 2.** This plot is similar to the plot mentioned previously in Fig. 3.7. The only difference is that in this plot inverse of the radial distributions are highlighted. However, both plots (Figs. 3.7 and 3.8) convey the same message.

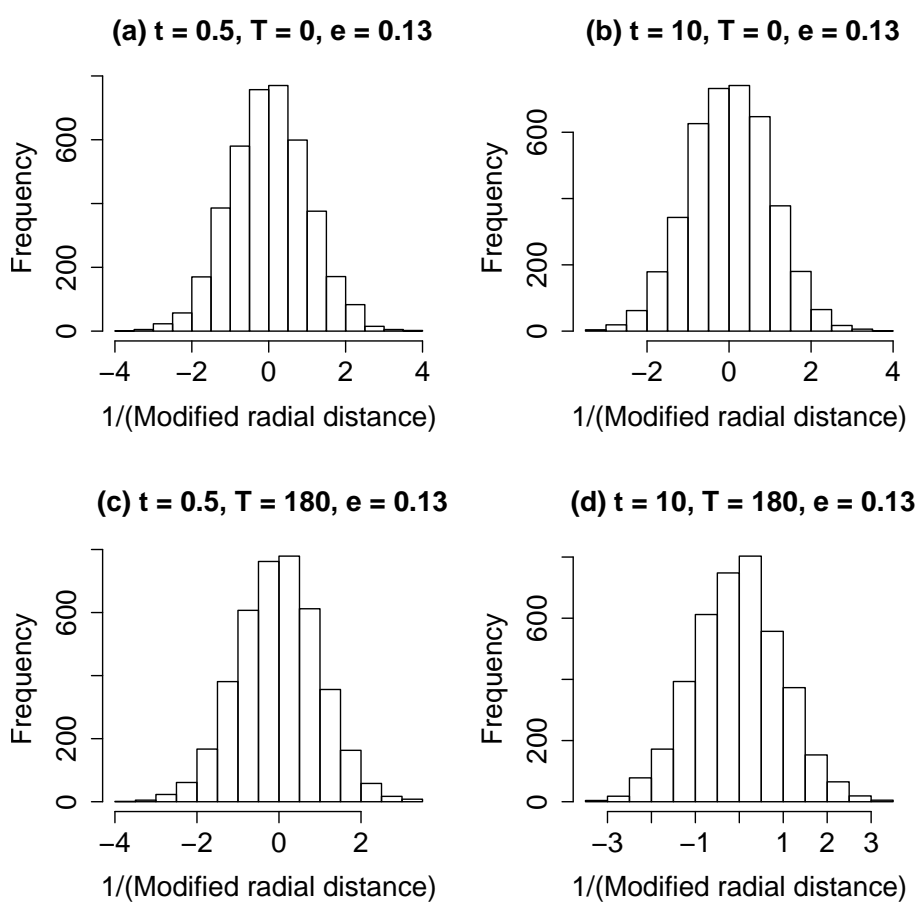


Figure 3.9: **Example 3.6., distribution of the *standardized* inverse radial component, part 3.** This plot represents standardized (inverse) radial components. As it can be seen all the radial distances are approximately univariate normal.

Chapter 4

Filtering, part 1

4.1 Introduction

The construction of a Kalman filter depends on three key ingredients, (i) the state vector, (ii) the observation vector and, (iii) their relation or the transformation function. In our case (space object tracking problem), the state space is the 6-dimensional AST-CRTN coordinate system and the observation space is the 2-dimensional (or 3-dimensional, if we incorporate the radial component) position vector (preferably angles-only). Clearly the transformation from the state space to the observation space is non-linear. Various methods have been proposed for solving the non-linear filtering problem, EKF, IEKF, UKF, IUKF. In this list we add two new Kalman filters, namely the OCEKF and the OCUKF. This chapter and the next chapter discuss these filters in details and a brief summary is given in Table 4.1.

The filtering or the tracking problem is demonstrated using two chapters. This chapter provides the basic details related to the tracking. The key intention of this chapter is to introduce various tracking algorithms to the reader using suitable 1-dimensional (1-to-1) examples. The next chapter discusses the higher dimensional (6-to-2) tracking problem.

Chapter 1 briefly introduced the EKF and UKF but did not talk about the centering location, this chapter mentions it in Section. 4.6. In general, the EKF and UKF are common choices for the non-linear Kalman filtering but there are situations where they are not good choices. The Observation-centered Kalman

Table 4.1: A summary on various non-linear Kalman filters. In this table, the EKF and UKF indicate the Extended Kalman Filter and the Unscented Kalman Filter respectively.

Classification	EKF	UKF	centering location
General	EKF	UKF	Prior mean
Iterated (I)	IEKF	IUKF	Posterior mean
Observation-centred (OC)	OCEKF	OCUKF	Observation mean

filters and iterated Kalman filters are performance wise similar. This chapter explores performance of various Kalman filters using suitable examples.

4.2 Key contributions

The key contributions of this chapter are listed below,

- (1) First, we discuss the *classical* Kalman filter and provide a suitable example (Section 4.4).
- (2) Second, we briefly describe various non-linear Kalman filters (Section 4.6).
- (3) Third, we provide suitable examples to illustrate limitations of the traditional (EKF and UKF) non-linear Kalman filters and advantages of using the iterated and observation-centered Kalman filters (Section 4.9).

Note that the EKF and UKF computational steps are given in the Appendix (Section B.1).

4.3 Relation to other chapters

This chapter and the next chapter will discuss the filtering problem. Of course, Chapter 1 provided some information related to the tracking/filtering but in this chapter we perform a detailed investigation on the tracking problem using 1-dimensional examples. In the next chapter, we will illustrate the usefulness of the AST-CRTN coordinate system for solving the six dimensional tracking problem. Note that the construction of the AST-CRTN coordinate system was

mentioned in Chapter 2. Further, we will discuss the filtering-association problem in Chapter 6 using concepts discussed in this chapter.

In this chapter we will start with the classic Kalman filter and after that we will move our focus to non-linear Kalman filters.

4.4 The classic Kalman filter

The classic Kalman filter (Chen, 2003; Youngjoo & Hyochoong, 2018) is designed for linear propagation and observation equations, with Gaussian noise. There is a sequence of l_1 -dimensional state vectors $\{\mathbf{x}_k\}$ and a sequence of l_2 -dimensional noisy (partial) observations $\{\mathbf{z}_k\}$ at times t_k , $k \geq 1$. Let \mathcal{F}_k denote the information contained in the first k observations $\mathbf{z}_1, \dots, \mathbf{z}_k$. The state vectors evolve through noisy linear propagation

$$\mathbf{x}_k = \mathbf{F}_k \mathbf{x}_{k-1} + \mathbf{w}_k, \quad (4.1)$$

where \mathbf{F}_k is a $l_1 \times l_1$ matrix and \mathbf{w}_k is system noise. Note that \mathbf{F}_k is also called the *state transition* matrix. The observations are noisy versions of linear functions of the state vectors,

$$\mathbf{z}_k = \mathbf{H}_k \mathbf{x}_k + \mathbf{v}_k, \quad (4.2)$$

where \mathbf{H}_k is a $l_2 \times l_1$ matrix and \mathbf{v}_k is the measurement noise. Note that \mathbf{H}_k is also called the *observation* matrix. The random vectors \mathbf{w}_k and \mathbf{v}_k are assumed independent of one another and of $\mathbf{z}_1, \dots, \mathbf{z}_{k-1}$, with $N_{l_1}(0, \mathbf{Q}_k)$ and $N_{l_2}(0, \mathbf{R}_k)$ distributions, respectively. The dimension l_1 of the state vector is allowed to be different from the dimension l_2 of the observation vector.

Start with an initial Gaussian distribution for \mathbf{x}_0 , with mean vector and covariance matrix denoted $\mathbf{x}_{0|0}, \mathbf{P}_{0|0}$. Then the conditional propagated distribution of \mathbf{x}_k given \mathcal{F}_k , $k \geq 1$ follows a Gaussian distribution. The conditional mean vector and covariance matrix, denoted $\mathbf{x}_{k|k}, \mathbf{P}_{k|k}$, say, can be determined iteratively as follows.

Suppose $\mathbf{x}_{k-1|k-1}$ and $\mathbf{P}_{k-1|k-1}$ are known. After propagation from time t_{k-1} to t_k , the conditional distribution of the state becomes

$$\mathbf{x}_k | \mathcal{F}_{k-1} \sim N_{l_1}(\mathbf{x}_{k|k-1}, \mathbf{P}_{k|k-1}),$$

4.5 Example 4.1., 1-dimensional linear tracking example

where

$$\mathbf{x}_{k|k-1} = \mathbf{F}_k \mathbf{x}_{k-1|k-1}, \quad \mathbf{P}_{k|k-1} = \mathbf{F}_k \mathbf{P}_{k-1|k-1} \mathbf{F}_k^T + \mathbf{Q}_k.$$

Given the observation \mathbf{z}_k at time t_k the Bayesian update yields the posterior distribution

$$\mathbf{x}_k | \mathcal{F}_k \sim N(\mathbf{x}_{k|k}, \mathbf{P}_{k|k})$$

and computation steps for the updated mean vector and the covariance matrix are given below (Chen, 2003; Wikipedia contributors, 2020b; Youngjoo & Hy-choong, 2018).

- (1) The measurement residual can be written as,

$$\mathbf{y}_k = (\mathbf{z}_k - \mathbf{H}_k \mathbf{x}_{k|k-1}). \quad (4.3)$$

- (2) Optimal Kalman gain is given by,

$$\mathbf{K}_k = \mathbf{P}_{k|k-1} \mathbf{H}_k^T (\mathbf{H}_k \mathbf{P}_{k|k-1} \mathbf{H}_k^T + \mathbf{R}_k)^{-1}. \quad (4.4)$$

- (3) Finally, the posterior mean and variance can be written as,

$$\mathbf{x}_{k|k} = \mathbf{x}_{k|k-1} + \mathbf{K}_k (\mathbf{z}_k - \mathbf{H}_k \mathbf{x}_{k|k-1}) \quad (4.5)$$

$$\mathbf{P}_{k|k} = (\mathbf{I} - \mathbf{K}_k \mathbf{H}_k) \mathbf{P}_{k|k-1}. \quad (4.6)$$

Next, an example is discussed. This example (Example 4.1.) is not related to the astrodynamics or space object tracking. The purpose of this example is to describe the use of the classical Kalman filter in 1-dimensional setting using computational steps mentioned above.

4.5 Example 4.1., 1-dimensional linear tracking example

Assume that we have some measurement meter and it generates some reading. We do not care about the functionality of the meter or parameters influencing readings. In this example, both the state and observation vectors are 1-dimensional

4.5 Example 4.1., 1-dimensional linear tracking example

(or scalar) (both of them are meter readings, same scale and scalar). The transformation matrix H_k is one dimensional (scaler).

For this example, $x_{1|0} = \mu_x^{\text{Kalman}}$, $P_{1|0} = \xi_1^2$, $Q_1 = 0$ and $R_1 = \xi_2^2$. Using Equations (4.3) to (4.6) for the one step update,

(1) Kalman gain can be written as,

$$K_1 = \frac{\xi_1^2}{\xi_1^2 + \xi_2^2}. \quad (4.7)$$

(2) Posterior mean and variance can be written as,

$$x_{1|1} = \mu_x^{\text{Kalman}} + \frac{\xi_1^2}{\xi_1^2 + \xi_2^2} (z_1 - \mu_x^{\text{Kalman}}). \quad (4.8)$$

$$P_{1|1} = \xi_1^2 - \frac{\xi_1^4}{\xi_1^2 + \xi_2^2} = \frac{\xi_1^2 \xi_2^2}{\xi_1^2 + \xi_2^2}. \quad (4.9)$$

From 4.8 and 4.9,

(a) if $\xi_2^2 \ll \xi_1^2$,

$$\begin{aligned} x_{1|1} &\approx \mu_x^{\text{Kalman}} + (z_1 - \mu_x^{\text{Kalman}}) \approx z_1. \\ P_{1|1} &\approx \xi_2^2, \end{aligned}$$

(b) if $\xi_2^2 = \xi_1^2$,

$$\begin{aligned} x_{1|1} &= \mu_x^{\text{Kalman}} + \frac{1}{2} (z_1 - \mu_x^{\text{Kalman}}). \\ P_{1|1} &= \xi_1^2 / 2, \end{aligned}$$

(c) finally, if $\xi_2^2 \gg \xi_1^2$,

$$\begin{aligned} x_{1|1} &\approx \mu_x^{\text{Kalman}} + \frac{\xi_1^2}{\xi_2^2} (z_1 - \mu_x^{\text{Kalman}}). \\ P_{1|1} &\approx \xi_1^2. \end{aligned}$$

Note that using the Kalman filter principle $x_{1|1}$ and $P_{1|1}$ will be used as the prior mean and variance for the next stage. Further, after the second update stage the posterior variance will be,

$$P_{2|2} = \frac{P_{2|1} \xi_2^2}{P_{2|1} + \xi_2^2} = \frac{\frac{\xi_1^2 \xi_2^2}{\xi_1^2 + \xi_2^2} \xi_2^2}{\frac{\xi_1^2 \xi_2^2}{\xi_1^2 + \xi_2^2} + \xi_2^2} = \frac{\xi_1^2 \xi_2^2}{2\xi_1^2 + \xi_2^2}. \quad (4.10)$$

4.5 Example 4.1., 1-dimensional linear tracking example

After a bit of computation, it can be showed that after the k^{th} update the posterior variance will be,

$$P_{k|k} = \frac{\xi_1^2 \xi_2^2}{k \xi_1^2 + \xi_2^2}. \quad (4.11)$$

Equation (4.11) can be further analysed using two possible test cases and they are mentioned below.

- (1) If $\xi_2^2 \ll \xi_1^2$, then posterior variances for stage 1 to k will be approximately $\xi_2^2, \xi_2^2/2, \xi_2^2/3, \dots, \xi_2^2/k$.
- (2) If $\xi_2^2 = \xi_1^2$, then posterior variances for stage 1 to k will be approximately $\xi_1^2/2, \xi_1^2/3, \xi_1^2/4, \dots, \xi_1^2/(k+1)$.

These two conditions are tested and results are summarized using variance plots.

- (1) Assume that $\xi_2^2 = 0.01$, $\xi_1^2 = 10$ ($\xi_1^2 \gg \xi_2^2$), $x_{1|0} = \mu_x^{\text{Kalman}} = 1$ and number of observations = 5. In this example, $\xi_2^2 \ll \xi_1^2$. Further, there is no process noise and observations are randomly chosen. The posterior variance plot is shown using Fig. 4.1 and it shows that the change of variance is $\propto O(1/k)$.

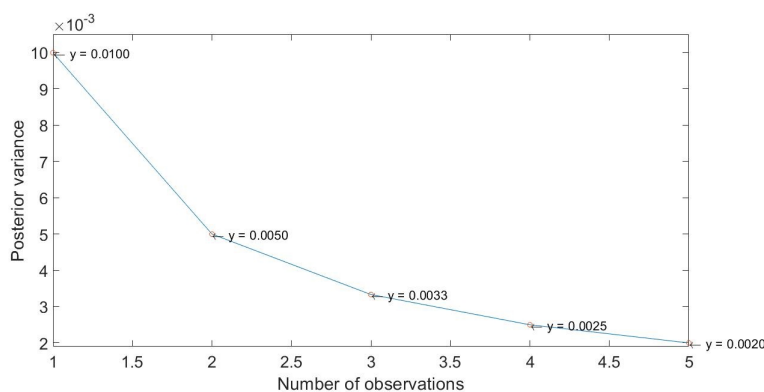


Figure 4.1: **Example 4.1., variance plot**, $\xi_2^2 \ll \xi_1^2$. In this example, total number of observations are 5 and $\xi_2^2 \ll \xi_1^2$. The posterior variance values are displayed in the plot (next to each plot marker) only for the visualization purpose. This plot shows that the rate at which the variances are decaying is $\propto O(1/k)$.

- (2) In this setup $\xi_2^2 = \xi_1^2 = 1$, $x_{1|0} = \mu_x^{\text{Kalman}} = 1$ and number of observations = 5 (same as before). The posterior variance is exhibited using Fig. 4.2 and it shows that rate of change of variance is $\propto O(1/k)$.

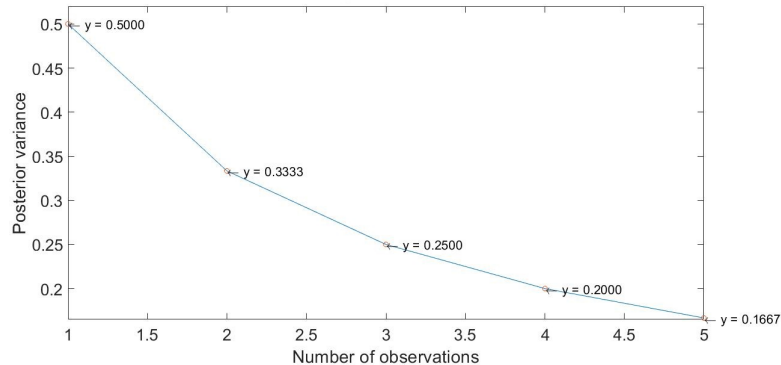


Figure 4.2: **Example 4.1., variance plot**, $\xi_1^2 = \xi_2^2 = 1$. In this example, total number of observations are 5 (same as before). This plot shows that the rate of change of variance is $\propto O(1/k)$.

4.6 Non-linear Kalman filters

Section 4.4 introduced the classic Kalman filter. Next, various non-linear Kalman filters are discussed using suitable 1-dimensional examples. Linear Kalman filters are easy to implement and understand but most of the real world tracking problems (including the space object tracking problem) are non-linear (as the transformation from the state vector to the observation vector is non-linear). This section discusses various non-linear Kalman filters in details.

4.6.1 The EKF, IEKF and OCEKF (1-dimensional setting)

Previous two sections provided details on the one step update for the linear (or classic) Kalman filter and also discussed the rate of change of variance. This section discusses one step update for the non-linear Kalman filters. The key materials for the one step update can be written as,

$$\text{Prior: } x \sim N(\mu_x^{\text{Kalman}}, \xi_1^2) \quad (4.12)$$

$$\text{Likelihood: } z|x \sim N(h_{\text{Kalman}}(x), \xi_2^2), \quad (4.13)$$

where, $h_{\text{Kalman}}(\cdot)$ is a known function, and where $x, \mu_x^{\text{Kalman}}, \xi_1^2, \xi_2^2$ correspond to $x_k, x_{k|k-1}, P_{k|k-1}, R_k$, respectively, in the Section 4.4. Note that vector signs

(boldfaces) are removed as the problems discussed in this chapter are one dimensional. Using Equations (4.12) and (4.13) the posterior distribution for the x given a realization z_{obs} of the observation z can be written as,

$$\begin{aligned} \text{Posterior} &\propto \text{Prior} \times \text{Likelihood}, \\ f(x|z_{\text{obs}}) &\propto \exp \left\{ -\frac{1}{2} \frac{(x - \mu_x^{\text{Kalman}})^2}{\xi_1^2} - \frac{1}{2} \frac{(z_{\text{obs}} - h_{\text{Kalman}}(x))^2}{\xi_2^2} \right\}. \end{aligned} \quad (4.14)$$

The EKF approximates this posterior distribution by a Gaussian distribution. Using the first order Taylor series, we can write,

$$\begin{aligned} z_{\text{obs}} - h_{\text{Kalman}}(x) &= z_{\text{obs}} - h_{\text{Kalman}}(y) + h_{\text{Kalman}}(y) - h_{\text{Kalman}}(x) \\ &\approx z_{\text{obs}} - h_{\text{Kalman}}(y) + h_{\text{Kalman}}'(y)(y - x), \end{aligned} \quad (4.15)$$

In Equation (4.15), the choice of y defines various filters (with different centering locations) Recall, Table 4.1, we discussed the centering location and the choice of y in Equation (4.15) leads to various centering locations. Further, the exponent becomes a quadratic function of x ; hence the approximating posterior distribution is Gaussian with mean and variance

$$\mu_{x|z_{\text{obs}}}^{\text{Kalman}} = \mu_x^{\text{Kalman}} + \frac{h_{\text{Kalman}}' \xi_1^2}{h_{\text{Kalman}}'^2 \xi_1^2 + \xi_2^2} \{z_{\text{obs}} - h_{\text{Kalman}}(y) + h_{\text{Kalman}}'[y - \mu_x^{\text{Kalman}}]\}, \quad (4.16)$$

$$\xi_{1|x|z_{\text{obs}}}^2 = \left(\frac{1}{\xi_1^2} + \frac{h_{\text{Kalman}}'^2}{\xi_2^2} \right)^{-1}, \quad (4.17)$$

where $h_{\text{Kalman}}' = h_{\text{Kalman}}'(y)$.

There are three important choices for y ($y = \mu_x^{\text{Kalman}}, \mu_{x|z_{\text{obs}}}^{\text{Kalman}}$ and x_{obs}).

- (a) $y = \mu_x^{\text{Kalman}}$, the *prior mean*. This choice gives the standard EKF. Equation (4.16) for the posterior mean takes the form,

$$\mu_{x|z_{\text{obs}}} = \mu_x^{\text{Kalman}} + \frac{h_{\text{Kalman}}' \xi_1^2}{h_{\text{Kalman}}'^2 \xi_1^2 + \xi_2^2} \{z_{\text{obs}} - h_{\text{Kalman}}(\mu_x^{\text{Kalman}})\}. \quad (4.18)$$

- (b) $y = \mu_{x|z_{\text{obs}}}^{\text{Kalman}}$, the *posterior mean*. This choice gives the iterated EKF. Equation (4.16) for the posterior mean becomes,

$$\mu_{x|z_{\text{obs}}}^{\text{Kalman}} = \mu_x^{\text{Kalman}} + \frac{h_{\text{Kalman}}' \xi_1^2}{h_{\text{Kalman}}'^2 \xi_1^2 + \xi_2^2} \{z_{\text{obs}} - h_{\text{Kalman}}(\mu_{x|z_{\text{obs}}}^{\text{Kalman}}) + h_{\text{Kalman}}'[\mu_{x|z_{\text{obs}}}^{\text{Kalman}} - \mu_x^{\text{Kalman}}]\}. \quad (4.19)$$

(c) $y = x_{\text{obs}} = h_{\text{Kalman}}^{-1}(z_{\text{obs}})$, the *transformed observation*. This choice gives the observation-centered EKF. Equation (4.16) for the posterior mean simplifies to,

$$\mu_{x|z_{\text{obs}}}^{\text{Kalman}} = \mu_x^{\text{Kalman}} + \frac{h_{\text{Kalman}}^2 \xi_1^2}{h_{\text{Kalman}}^2 \xi_1^2 + \xi_2^2} \{x_{\text{obs}} - \mu_x^{\text{Kalman}}\}. \quad (4.20)$$

Assuming that h_{Kalman} is monotone, so inverse exists.

4.6.2 The UKF, IUKF and OCUKF (1-dimensional setting)

The EKF uses the first order Taylor series approximation whereas the UKF uses the sigma points. Further, similar to the Subsection 4.6.1 various choices of y give different versions of the UKF (UKF, IUKF and OCUKF). The starting point is a collection of three ‘‘UKF sigma points’’,

$$\begin{aligned} x_{-1} &= y - W\xi_1, & x_0 &= y, & x_{+1} &= y + W\xi_1, \\ W &= \sqrt{l + \lambda^{\text{UKF}}}, & \lambda^{\text{UKF}} &= \alpha^{\text{UKF}^2}(l + \kappa^{\text{UKF}}) - l, \end{aligned} \quad (4.21)$$

where W is the weight and made of various ‘‘tuning’’ parameters (α^{UKF} , β^{UKF} and κ^{UKF}). Note that l denotes the dimension. Two sets of weights are defined,

$$\begin{aligned} w_{-1}^a &= w_{+1}^a = \frac{1}{2(l + \lambda^{\text{UKF}})}, & w_0^a &= \frac{\lambda^{\text{UKF}}}{l + \lambda^{\text{UKF}}} \\ w_{-1}^v &= w_{+1}^v = \frac{1}{2(l + \lambda^{\text{UKF}})}, & w_0^v &= \frac{\lambda^{\text{UKF}}}{l + \lambda^{\text{UKF}}} + 1 - \alpha^{\text{UKF}^2} + \beta^{\text{UKF}}, \end{aligned}$$

where the first weights (related to superscript a) are used to compute means and the second weights (related to superscript v) are used to compute variances and covariances.

A smaller value of α^{UKF} indicates that the sigma points are located close to y (mean). The sigma points have weighted mean and variance,

$$\sum w_j^a x_j = y, \quad \sum w_j^v (x_j - y)^2 = \xi_1^2,$$

where in all cases the sums range over $j = -1, 0, +1$.

4.7 Intuition behind the iterated and observation-centered filters

Let $z_j = h_{\text{Kalman}}(x_j)$ denote the transformed sigma points, with mean $\bar{z} = \sum w_j^a z_j$. Let $C_{\text{Kalman}} = C_{\text{Kalman}}(y)$ and $V_{\text{Kalman}} = V_{\text{Kalman}}(y)$ denote the weighted covariance between the $\{z_j\}$ and $\{x_j\}$, and the weighted variance of the $\{z_j\}$, respectively,

$$C_{\text{Kalman}}(y) = \sum w_j^v (z_j - \bar{z})(x_j - y), \quad V_{\text{Kalman}}(y) = \sum w_j^v (z_j - \bar{z})^2.$$

Typically, a small value of α^{UKF} is recommended if the system is highly non-linear, κ^{UKF} can be any number but $\kappa^{\text{UKF}} \geq 0$ or $l + \kappa^{\text{UKF}} = 3$ (l is the dimension) ensures the positive semi-definiteness of the covariance matrix and $\beta^{\text{UKF}} = 2$ (Julier *et al.*, 2000; Yongfang & Tao, 2018). However, the exact choices of these scaling parameters depend on the problem (Yongfang & Tao, 2018). Several choices of unscented filter can be defined by mimicking the extended filters in (4.16)–(4.17),

$$\begin{aligned} \mu_{x|z_{\text{obs}}}^{\text{Kalman}} &= \mu_x^{\text{Kalman}} + \frac{C_{\text{Kalman}}}{V_{\text{Kalman}} + \xi_2^2} \{z_{\text{obs}} - h_{\text{Kalman}}(y) + (V/C)[y - \mu_x^{\text{Kalman}}]\}, \quad (4.22) \\ \xi_{1|x|z_{\text{obs}}}^2 &= \xi_1^2 - C_{\text{Kalman}}^2 / (V_{\text{Kalman}} + \xi_2^2), \end{aligned}$$

for suitable values of y .

- (a) The standard UKF uses $y = \mu_x^{\text{Kalman}}$.
- (b) The IUKF uses $y = \mu_{x|z_{\text{obs}}}^{\text{Kalman}}$ in (4.22).
- (c) Similar to the IUKF, it is possible to define an observation-centered UKF (OCUKF) by using $y = x_{\text{obs}} = h_{\text{Kalman}}^{-1}(z_{\text{obs}})$ in (4.22).

4.7 Intuition behind the iterated and observation-centered filters

The Taylor series approximation in (4.15) is a good approximation if h_{Kalman} is approximately linear over an interval containing y and x . When ξ_2^2 is small and ξ_1^2 is not small, then the posterior distribution of x should be concentrated near x_{obs} . The choice $y = \mu_x^{\text{Kalman}}$ may not be a good choice in this setting; the effective support of the posterior distribution of x may be a long way from μ_x^{Kalman}

4.8 Example 4.2., idealized analytic example

and h_{Kalman} may be very non-linear over this interval. On the other hand, both $y = \mu_{x|z_{\text{obs}}}^{\text{Kalman}}$ (iterated) and $y = x_{\text{obs}}$ (observation-centered) may be very good choices; these two values will be close together and the posterior distribution will be concentrated near both these choices. Since, ξ_2^2 is small (for space object tracking problem), it is reasonable to map the variability in z about $h_{\text{Kalman}}(x)$ from the measurement scale to the signal scale. This approach is used by the iterated and observation-centered filters.

There are several features in this setup that make the iterated and observation-centered filters feasible and effective.

- (1) The prior distribution of the signal is exactly normal.
- (2) The transformation function h_{Kalman} is allowed to be highly non-linear (but still monotone).
- (3) The standard deviation ξ_2 for the distribution of an observation z given x is small.
- (4) For the observation-centered filters, the mapping between signal space and observation space is one to one. In particular it is possible to define x_{obs} , the value on the signal scale corresponding to the observation z_{obs} on the measurement scale. This is the key requirement for the observation-centered filters. We will discuss more about it in the next chapter.

Note that if h_{Kalman} is a linear function (or nearly linear) then all the filters are performance wise similar.

4.8 Example 4.2., idealized analytic example

To illustrate the issues involved, consider an idealized version of the problem and limit attention to the extended filters. Suppose that the mapping from the signal scale to the measurement scale is defined by x^λ (first order derivative $\lambda x^{\lambda-1}$), where λ is a known power. Let $\xi_2^2 = 0$, so there is no measurement error. In addition, assume that $\mu_x^{\text{Kalman}} = 1$ and $z_{\text{obs}} = 2$ are fixed. The choice of ξ_1^2 is irrelevant for this section.

4.9 Application to 1-dimensional orbital dynamics

The standard EKF gets the posterior variance $\xi_{1x|z_{\text{obs}}}^2 = 0$ correct, but gets the posterior mean wrong. Results for various extended filters are summarized in Table 4.2. Note that the EKF overshoots the exact posterior mean if $\lambda < 1$ and undershoots the exact posterior mean if $\lambda > 1$.

Table 4.2: Comparison between various approximations to the posterior distribution for idealized example in Section 4.8. The exact posterior distribution is centered at the value given in the column “Truth”. The IEKF and OCEKF results match the exact result here. However, the EKF gives the wrong value. The exact posterior distribution has zero variance and all three filters (EKF, IEKF and OCEKF) produce the right value.

λ	EKF	IEKF OCEKF Truth
1	2	2.00
0.5	1.5	1.41
2	3	4

4.9 Application to 1-dimensional orbital dynamics

Recall Chapter 1, we use $M(t)$, $T(t)$, e , $F_{M \rightarrow T}$ to denote the mean anomaly at time t (measured from the perigee), the true anomaly at time t (measured from the perigee), orbital eccentricity and the function which maps from the mean to the true anomaly (non-linear but linear if e is 0) respectively. Suppose that the initial mean anomaly $M(0)$ at time $t = 0$ is known exactly, but that the mean motion n has some Gaussian uncertainty, $n \sim N(\mu_n^{\text{Kalman}}, \xi_{1n}^2)$. Then after some time t_1 , say, the mean anomaly has distribution

$$M(t_1) \sim N(M(0) + t_1 \mu_n^{\text{Kalman}}, t_1 \xi_{1n}^2).$$

However, the observation is on the true anomaly scale ($T(t_1)$ or true anomaly measured from the perigee)

$$T_{\text{obs}} \sim N(T(t_1), \xi_2^2), \quad T(t_1) = F_{M \rightarrow T}(M(t_1), e).$$

4.9 Application to 1-dimensional orbital dynamics

Note that even if ξ_{1n}^2 is small, $\xi_1^2 = t_1 \xi_{1n}^2$ can still become large by considering a large propagation time t_1 . For the purposes of this chapter, suppose ξ_1^2 is not too large in order to avoid winding number issues. In particular, restrict $\xi_1 = t_1^{1/2} \xi_{1n}$ to be substantially less than 360° so that T_{obs} can be treated as a number unambiguously satisfying $|T_{\text{obs}} - T(t_1)| < 360^\circ$. In other words the number of whole orbits undergone is essentially known. The choices $\xi_1 = 25^\circ$ and $\xi_1 = 15^\circ$ are used in the examples below.

At the same time, the typical angles-only observations will be highly accurate. Three choices for ξ_2 are used in each example: (a) $\xi_2 = 0^\circ$ for a perfect measurement (rare), (b) $\xi_2 = 1.66e^{-02^\circ}$ (equal to 1 arc-minute) for a realistic measurement error, and (c) $\xi_2 = 2^\circ$ for a good but less accurate measurement.

Let $M(t_1)$ here corresponds to the state x in Section 4.4, with variance ξ_1^2 , and let z_{obs} denotes the observed true anomaly, with variance ξ_2^2 . Thus the state variable is the mean anomaly $x = M(t_1)$ lying on the signal scale, and the observation is the true anomaly $z_{\text{obs}} = T_{\text{obs}}$ lying on the measurement scale.

Here are two numerical examples to illustrate the pitfalls of the EKF, UKF and to demonstrate the benefits of the IEKF, IUKEF, OCEKF and OCUKF. For both examples a high value of ellipticity is used, $e = 0.7$, so that the function $h_{\text{Kalman}} = F_{M \rightarrow T}$ is very non-linear and the differences between the various filters stand out prominently. The parameters for each example are listed in Table 4.3 and highlighted in Figure 4.3. The posterior means and variances for various filters are summarized in Table 4.4. The row labeled ‘‘Truth’’ in that table gives the exact moments from the true posterior distribution, as computed by numerical integration.

Example 4.3. Since $x_{\text{obs}} = 310^\circ = 260^\circ + 2 \times 25^\circ = \mu_x^{\text{Kalman}} + 2\xi_1$, the observation is mildly unusual but not infeasible under the prior distribution.

Part 1 ($\xi_2 = 0^\circ$). Since the observation standard derivation is zero, the posterior distribution for the mean anomaly is concentrated at x_{obs} with zero posterior variance. From Table 4.4, note that just as in the idealized example in Section 4.8, both the EKF and the UKF are hugely incorrect for the mean, whereas the IEKF, IUKEF, OCEKF and OCUKF produce the right mean. All the posterior standard deviations are correctly computed as 0° , except for the UKF,

4.9 Application to 1-dimensional orbital dynamics

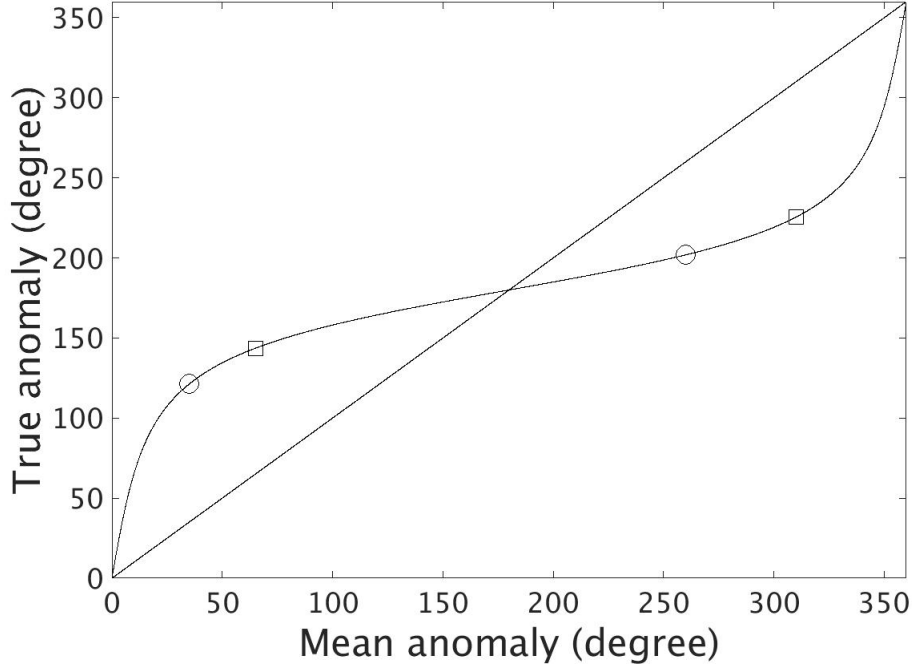


Figure 4.3: **Mapping $F_{M\text{-}to\text{-}T}$ function when $e = 0.7$.** True anomaly as a function of mean anomaly, for eccentricity $e = 0$ (diagonal straight line) and $e = 0.7$ (curved line). Angles are given in degrees. The points indicated by circles, after projection onto the horizontal axis, give the prior means μ_x^{Kalman} for Examples 4.3. and 4.4. The points indicated by boxes, after projection onto the vertical axis, give the observations z_{obs} , and after projection onto the horizontal axis, give the values of $x_{\text{obs}} = h_{\text{Kalman}}^{-1}(z_{\text{obs}})$, for Examples 4.3. and 4.4.

IUKF and OCUKF. The problem with the UKF, IUKF and OCUKF is that they are using differences rather than derivatives to cope with the non-linearity.

Part 2 ($\xi_2 = 1.66e^{-020}$). This is a more realistic assumption. In this case both the EKF and UKF behave badly. However, the IEKF, IUKF, OCEKF, OCUKF are able to approximate the true posterior mean and variance closely.

Part 3 ($\xi_2 = 2^\circ$). In this case the posterior means and standard deviations for IEKF, IUKF, OCEKF and OCUKF posterior means and variances are very close to the true values. On the other hand the EKF and UKF posterior means and variances are so bad that a 95% confidence interval about the true posterior mean would not include either the EKF or the UKF posterior mean. Note that

for EKF and UKF, the posterior means are too *large*.

Example 4.4. Now, $x_{\text{obs}} = 65^\circ = 35^\circ + 2 \times 15^\circ = \mu_x^{\text{Kalman}} + 2\xi_1$, so again the observation is mildly unusual but not infeasible under the prior distribution. For all three values of ξ_2 ($\xi_2 = 0^\circ, 1.66e^{-02^\circ}$ and 2°), the behavior of the different filters and the comparisons between them are the same as for Example 4.3. But in this case for EKF and UKF, the posterior means are too *small*.

Table 4.3: The prior means μ_x^{Kalman} and its standard deviations ξ_1 , plus the observations z_{obs} and its standard deviations ξ_2 for Examples 4.3. and 4.4. In each case three choice for the error standard deviation ξ_2 are considered. The value of $h_{\text{Kalman}}^{-1}(z_{\text{obs}}) = x_{\text{obs}}$ is also given.

Example 4.3.	Example 4.4.
$\mu_x^{\text{Kalman}} = 260^\circ$	$\mu_x^{\text{Kalman}} = 35^\circ$
$\xi_1 = 25^\circ$	$\xi_1 = 15^\circ$
$z_{\text{obs}} = 225.5^\circ$	$z_{\text{obs}} = 143.6^\circ$
$x_{\text{obs}} = 310^\circ$	$x_{\text{obs}} = 65^\circ$
	a: $\xi_2 = 0^\circ$
	b: $\xi_2 = 1.66e^{-02^\circ}$
	c: $\xi_2 = 2^\circ$

4.10 Performance analysis

Several conclusions can be made from above mentioned simulations.

- (1) The EKF and UKF are standard methods to deal with non-linear filtering problems. However, when the non-linearity is high and the observation variance ξ_2^2 is small relative to the prior state variance ξ_1^2 , these filters can perform very poorly.
- (2) In terms of performance, the IEKF, IUKF, OCEKF and OCUKF are very similar for the examples in this chapter. Further, the posterior means and variances computed using these filters closely match the true posterior moments.

4.10 Performance analysis

Table 4.4: Posterior means and standard deviations (s.d.) from various filters for Examples 4.3. (a,b,c) and 4.4. (a,b,c).

KF/Example	moment	4.3(a)	4.3(b)	4.3(c)	4.4(a)	4.4(b)	4.4(c)
Truth	mean	310.0 ^o	309.989 ^o	309.0 ^o	65.0 ^o	64.956 ^o	63.5 ^o
	s.d.	0 ^o	2.3e ^{-02o}	2.8 ^o	0 ^o	3.2e ^{-02o}	3.5 ^o
EKF	mean	329.8 ^o	329.831 ^o	326.1 ^o	55.0 ^o	55.073 ^o	54.8 ^o
	s.d.	0 ^o	4.8e ^{-02o}	5.7 ^o	0 ^o	1.5e ^{-02o}	1.7 ^o
UKF	mean	327.1 ^o	327.088 ^o	323.5 ^o	59.1 ^o	59.184 ^o	58.9 ^o
	s.d.	2e ^{-03o}	4.8e ^{-02o}	5.8 ^o	4e ^{-03o}	3.2e ^{-02o}	1.8 ^o
IEKF	mean	310.0 ^o	309.989 ^o	309.3 ^o	65 ^o	64.956 ^o	63.2 ^o
	s.d.	0 ^o	2.3e ^{-02o}	2.8 ^o	0 ^o	3.2e ^{-02o}	3.5 ^o
IUKF	mean	310.0 ^o	309.989 ^o	309.3 ^o	65 ^o	64.956 ^o	63.2 ^o
	s.d.	7e ^{-03o}	2.3e ^{-02o}	2.8 ^o	2e ^{-03o}	3.2e ^{-02o}	3.5 ^o
OCEKF	mean	310.0 ^o	309.989 ^o	309.3 ^o	65 ^o	64.956 ^o	63.1 ^o
	s.d.	0 ^o	2.3e ^{-02o}	2.7 ^o	0 ^o	3.2e ^{-02o}	3.7 ^o
OCUKF	mean	310.0 ^o	309.989 ^o	309.3 ^o	65 ^o	64.956 ^o	63.2 ^o
	s.d.	7e ^{-03o}	2.3e ^{-02o}	2.8 ^o	2e ^{-03o}	3.2e ^{-02o}	3.7 ^o

- (3) One advantage of the OCEKF and OCUKF over the IEKF and the IUKF is that they do not require iteration.
- (4) However, an advantage of the IEKF and the IUKF over the OCEKF and the OCUKF is that they are more widely applicable. In situations where ξ_2^2 is not small relative to ξ_1^2 , the OC filters can perform badly.

Chapter 5

Filtering, part 2

5.1 Introduction

The previous chapter introduced various Kalman filters and compared them using suitable 1-dimensional examples. This chapter discusses the filtering algorithm for solving the 6-dimensional space object tracking problem. Recall the AST (AST-CRTN) coordinate system discussed in the Chapter 2, one of the main purposes behind the development of the AST-CRTN coordinate system is to use it for treating the filtering problem. The previous chapter discussed and compared various Kalman filters. Note that complexity wise both the UKF and EKF are same and performance wise the UKF is same or better ([Julier *et al.*, 2000](#)). The major benefit of using the UKF is that the construction of the UKF does not require the computation of a complicated Jacobian matrix (like the EKF).

The iterated filters are widely used for dealing with the tracking problem and these filters use the EKF or the UKF in the background (with different centering locations). The first part of this chapter discusses the AST-IUKF algorithm. One tracking example is provided to show the power of the AST-IUKF algorithm. The term AST-IUKF refers that the IUKF algorithm (already mentioned in the previous chapter) is used with the AST-CRTN coordinate system.

The second part of this chapter deals with the Observation-Centered Kalman filter. Recall the previous chapter, we discussed the OCEKF and OCUKF algorithm but for solving one dimensional filtering problems. This chapter illustrates how to use Observation-Centered filters for solving 6-dimensional orbital track-

ing problem. Two methods/versions are proposed and discussed in this chapter. The Observation-Centered filter for solving higher dimensional tracking problem is a *hybrid filter* and consists of two stages, (i) the first stage is the Observation-Centered (OC) filtering stage (non-linear filter, fixing the longitude, 1-to-1 mapping) and, (ii) the second stage is the non-linear Kalman filtering (such as the EKF or the UKF) stage (again non-linear filter, mainly fixing the latitude, 6-to-2 mapping). However, by tuning filtering parameters properly, the second stage of the Observation-Centered filter (for 6-dimensional tracking) reduces to a *linear* Kalman filter.

5.2 Key contributions

This chapter deals with two key contributions, they are listed below.

- (1) First, we discuss the AST-IUKF algorithm and provides an example to illustrate the power of the AST-IUKF algorithm (Section 5.4).
- (2) Next, we discuss the AST-OC filter algorithm. Further, we also show that by using an Observation-Centered filter the space object tracking problem can be solved using a linear Kalman filter to a certain extent (Sections 5.5 to 5.7).

5.3 Relation to other chapters

The previous chapter discussed various Kalman filters and we will use them in this chapter. In addition, we will also use the AST (AST-CRTN) and ASP (ASP-CRTN) coordinate systems for the tracking purpose. Further, we will use tracking algorithms discussed in this chapter to tackle the filtering-association problem in the next chapter.

5.4 Simulated Tracking example using the AST-IUKF algorithm

Assume that each observation is represented in the ASP-CRTN coordinate system and takes the form of an angles-only position measurement (a unit vector $\mathbf{z}_{\text{obs}} = [z_1, z_2, z_3]^T$), the “latitude” $\psi_{\text{obs}} = \psi_{\text{obs}}^{\text{CRTN}} \in [-\pi/2, \pi/2]$ and “longitude” $\theta_{\text{obs}} = \theta_{\text{obs}}^{\text{CRTN}} \in [-\pi, \pi)$. The equivalent Cartesian coordinates are,

$$z_1 = \cos \psi_{\text{obs}}^{\text{CRTN}} \cos \theta_{\text{obs}}^{\text{CRTN}}, \quad z_2 = \cos \psi_{\text{obs}}^{\text{CRTN}} \sin \theta_{\text{obs}}^{\text{CRTN}}, \quad z_3 = \sin \psi_{\text{obs}}^{\text{CRTN}}.$$

- (a) The longitude is computed on the true anomaly scale. Further, when the observation error is small (or zero), the longitude can be written as,

$$\theta_{\text{obs}}^{\text{CRTN}}(t) \approx \theta_p^{\text{CRTN}} + T(t).$$

Note that θ_p^{CRTN} and $T(t)$ are true values.

- (b) AST-CRTN element 3 ($A_3(t) = \phi^{\text{CRTN}}(t)$) is computed on the mean anomaly scale (see 2.4).
- (c) Recall Fig. 4.3, the transformation from mean anomaly to true anomaly can be extremely non-linear under high eccentricity.

Note: In this chapter, all the computations are performed on the CRTN reference basis (similar to Chapters 2 and 3)

Next consider the update stage of the Kalman filter. In particular, it requires a 6-dimensional variance matrix for the propagated state $\mathbf{A}(t)$, and a 2-dimensional measurement variance matrix for $(\theta_{\text{obs}}(t), \psi_{\text{obs}}(t))$. Of these, the most interesting components are the propagated variance of $A_3(t)$ and the measurement variance of the longitude $\theta_{\text{obs}}(t)$. If the eccentricity is high, then a non-linear version of the Kalman filter is needed. Common choices are the unscented and extended Kalman filters (UKF and EKF).

However, if in addition the propagation time is large, then the propagated variance of $A_3(t)$ can be much larger than the measurement variance of $\theta_{\text{obs}}(t)$. In such a situation the UKF and EKF can perform very poorly (also see Section

5.4 Simulated Tracking example using the AST-IUKF algorithm

4.9). The reason is that they deal with the non-linearity by taking a Taylor expansion centered at the propagated mean of $A_3(t)$, whereas it is much better to center the Taylor expansion at or near the measurement value $F_{T-t_0-M}(\theta_{\text{obs}}, e)$ ($\approx F_{T-t_0-M}(\theta_{\text{obs}}, e^{(c)})$), where $e^{(c)}$ is the *central* eccentricity for the mean propagated state.

This (performance issue related to the EKF and UKF) leads to 4 solutions: (a and b) newly developed observation-centered Kalman filters, (c and d) iterated Kalman filters such as the IEKF and IUKF. This chapter uses IUKF for update steps. We choose the IUKF due to the fact that when the measurement error is large, iterated filters are performance-wise better than the Observation-Centered filters. Note that the mapping from AST-CRTN(t) (AST-CRTN state vector) to $(\theta(t), \psi(t))$ (state vector represented in the ambient coordinate) is already mentioned in Chapter 3, Equation (3.12). Next, the AST-IUKF steps are briefly summarized.

Given

- a. The central state in Cartesian-ECI coordinates at time $t = 0$;
- b. The covariance matrix associated with the central state in Cartesian-ECI coordinate system;
- c. Sequence of angles-only measurements;

Computation

- 1) Find the CRTN frame;
- 2) Compute the initial mean state and its covariance matrix in AST-CRTN coordinates;
- 3) Transform angles-only measurements to the CRTN coordinates;
- 4) Propagate and update AST-CRTN state mean and variance using IUKF;
- 5) Repeat stages 3) and 4) for each observation;

Algorithm 1: AST-IUKF stages

5.4.1 Example 5.1.

Example 5.1. Tracking. The purpose of this example is to describe effectiveness of the AST-IUKF algorithm for solving the orbital tracking problem. Consider the same object mentioned in Chapter 2 (Section 2.5.3), and consider

5.5 The Observation-Centered Filter for solving higher dimensional tracking problem, approach 1

a sequence of 200 hourly angles-only observations (sequence of observations), with standard deviations 0.1° in in-track and cross-track directions. Results are summarized using Figs. 5.1 and 5.2. In order to judge the performance of the AST-IUKF, three sets of plots are generated and analyzed. A brief description is given below.

- (a) **Log scaled variance plots.** Intuitively the AST-CRTN posterior variances for $A_1(t_k)$ to $A_5(t_k)$ are expected to decrease at rate $O(1/t_k)$ (Section 4.5, Example 4.1. discusses the rate of change of variance using analytic expansion), and the posterior variance for $A_6(t_k)$ to decrease at rate $O(1/t_k^2)$. To visualize this behavior, Fig. 5.1 shows plots of $\log_e\{A_j(t_k)t_k\}$, $j = 1, \dots, 5$ and $\log_e\{A_6(t_k)t_k^2\}$ vs. t_k . The log transform is used so that a few initial outliers do not distort the plot. As expected, except for a few initial values, each plot is approximately a horizontal straight line.
- (b) **Log scaled absolute difference plots.** Similarly, Fig. 5.2 shows plots of $\log_e\{D_j^{\text{abs}}(t_k)t_k^{1/2}\}$, $j = 1, \dots, 5$ and $\log_e\{D_6^{\text{abs}}(t_k)t_k\}$ vs. t_k , where $D_j^{\text{abs}}(t_k)$ denotes the absolute difference between the true AST-CRTN value and the updated AST-CRTN mean at time t_k , for $j = 1, \dots, 6$. As expected, up to sampling error all the plots are approximately horizontal straight lines.

5.5 The Observation-Centered Filter for solving higher dimensional tracking problem, approach 1

In the previous chapter, we discussed Observation-Centered filters. However, problems discussed in the previous chapter were 1-dimensional. The principle behind the OCEKF/OCUKF works only if the state and the observation have the same dimension. In orbital dynamics problem, the state is always 6-dimensional, but an angles only observation is only 2-dimensional. However, in some cases it may be possible to split the state vector into two parts, where the first part has same dimension as the observation vector. Then an Observation-Centered filter can be used for the first part and an EKF/UKF can be used for the second part (*hybrid approach*).

5.5 The Observation-Centered Filter for solving higher dimensional tracking problem, approach 1

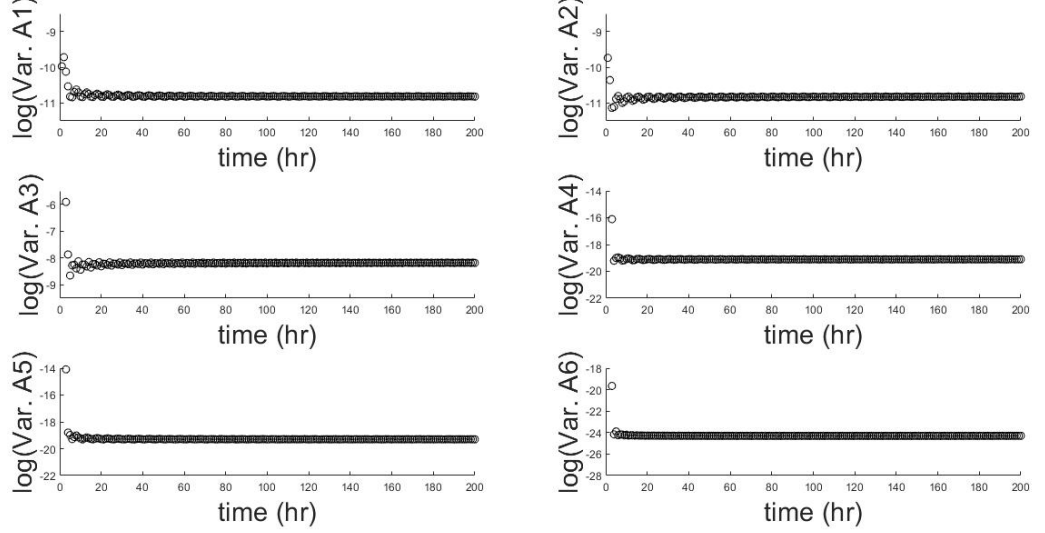


Figure 5.1: **Example 5.1., log scaled variance plots.** The log scaled updated AST-CRTN variances vs. time for A1-A6.

5.5.1 Stage-1, the Observation-Centered filtering stage

As mentioned previously, most interesting elements of the state and the observation vectors are $A_3(t)$ (measured in the mean anomaly scale) and $\theta_{\text{obs}}(t)$ (measured in the true anomaly scale) respectively. In addition, under Keplerian dynamics only $A_3(t)$ changes with time (among all 6 elements of the state vector). The first stage of this *hybrid* filter (or overall filter) consists of 1-dimensional filtering between $A_3(t)$ and $\theta_{\text{obs}}(t)$. Further, perform either the OCEKF or the OCUKF at this stage. This stage is visually illustrated using Equation (5.1).

$$\mathbf{A}(t) = \boldsymbol{\mu}_x^{\text{Kalman}} = \begin{bmatrix} A_3(t) \\ \text{---} \\ A_1 \\ A_2 \\ A_4 \\ A_5 \\ A_6 \end{bmatrix} \left. \begin{array}{l} \} x_1 \\ \\ \} x_2 \end{array} \right\} \quad \mathbf{z}_{\text{obs}} = \begin{bmatrix} \theta_{\text{obs}}(t) \\ \psi_{\text{obs}}(t) \end{bmatrix} \left. \begin{array}{l} \} z_1 \\ \} z_2 \end{array} \right\} \quad \boldsymbol{\mu}_{x|z_{\text{obs}}}^{\text{Kalman}^*} = A_3^*(t) \tag{5.1}$$

5.5 The Observation-Centered Filter for solving higher dimensional tracking problem, approach 1

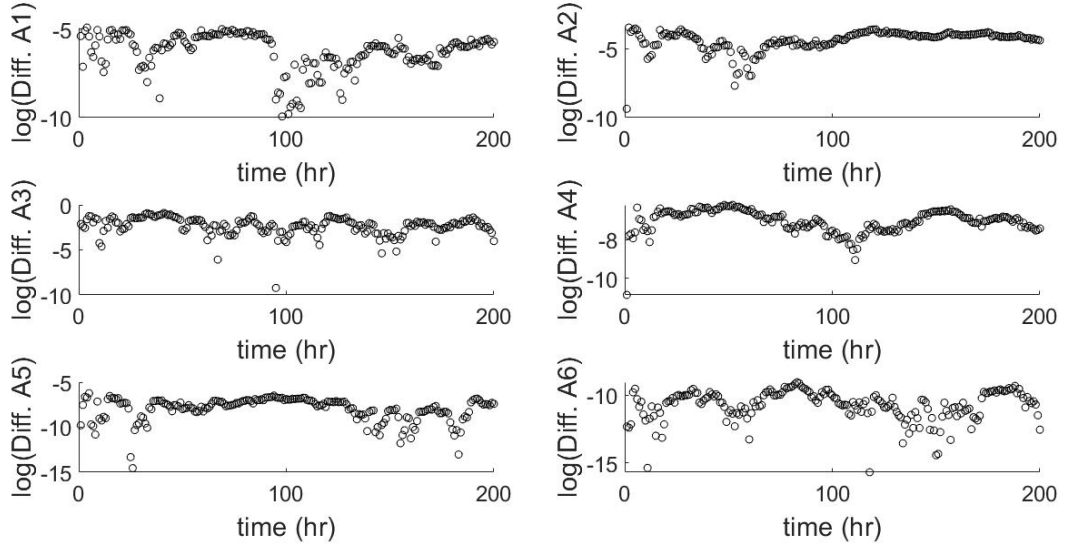


Figure 5.2: **Example 5.1., log scaled absolute difference plots.** The log scaled absolute differences between the true AST-CRTN values and the updated AST-CRTN means vs. time for A1-A6.

For this stage, both the state and observation vectors are scalar (1-dimensional). In Equation (5.1), the state vector ($A_3(t)$) is shown using x_1 and the observation vector ($\theta_{\text{obs}}(t)$) is indicated using z_1 . In addition, assume that after using the Observation-Centered filter the posterior mean or the *pseudo posterior mean* is $A_3^*(t)$ ($= \mu_{x|z_{\text{obs}}}^{\text{Kalman}^*}$), $A_3^*(t)$ will be used as the prior mean (in place of $A_3(t)$) during the second stage.

5.5.2 Stage-2, the non-linear filtering stage

This stage can be performed either using the EKF or the UKF and there is no need to use an iterated Kalman filter. Note that $A_3^*(t)$ is used in place of $A_3(t)$ as the prior mean for the third AST-CRTN element (in $\mu_x^{\text{Kalman}^*}$). In this stage the state vector (say, $\mu_x^{\text{Kalman}^*}$) is 6 dimensional (see Equation (5.2)) and the observation vector is 2 dimensional (consisting of both the latitude and the longitude and indicated using z_{obs} in Equation (5.2)). In addition, the posterior mean is indicated using $\mu_{x|z_{\text{obs}}}^{\text{Kalman}^{**}}$. In a sense this hybrid filter is a specialized

case of the iterated Kalman filter. Further, the third AST-CRTN element will be updated twice during the whole filtering process (first during the Observation-Centered filtering stage and second during the UKF/EKF stage).

See 5.2 for an illustration.

$$\mathbf{A}(t)^* = \boldsymbol{\mu}_x^{\text{Kalman}^*} = \begin{bmatrix} A_1 \\ A_2 \\ A_3^*(t) \\ A_4 \\ A_5 \\ A_6 \end{bmatrix} \quad \mathbf{z}_{\text{obs}} = \begin{bmatrix} \theta_{\text{obs}}(t) \\ \psi_{\text{obs}}(t) \end{bmatrix} \quad \boldsymbol{\mu}_{\mathbf{x}|\mathbf{z}_{\text{obs}}}^{\text{Kalman}^{**}} = \begin{bmatrix} A_1^* \\ A_2^* \\ A_3^{**}(t) \\ A_4^* \\ A_5^* \\ A_6^* \end{bmatrix} \quad (5.2)$$

5.6 The Observation-Centered Filter, approach 2

Section 5.5 discussed a way to use the OC algorithm for tackling the space object tracking problem. Note that during the second stage of the filter, we suggested to use an UKF (non-linear filter). In this section, we propose another version of the OC filter which uses a *linear* Kalman filter for the space object tracking problem. However, the first stage of the filter or the OC stage remains same as before (Subsection 5.5.1) but we modify the second stage. Detailed description is given below.

5.6.1 Stage-1, the Observation-Centered filtering stage

Same as in Subsection 5.5.1.

5.6.2 Stage-2, the non-linear filtering stage

During this step, we suggest two modifications in representing the $\mathbf{z}_{\text{obs}}(t)$ or the observation vector. They are,

- (1) Replace $\theta_{\text{obs}}(t)$ by $\phi_{\text{obs}}(t)$.

$$\begin{aligned} \phi_{\text{obs}} &\approx \phi_p^{(c)}(t) + F_{\text{T-to-M}}(\theta_{\text{obs}} - \theta_p^{(c)}, e^{(c)}), \\ \theta_p^{(c)} &= F_{\text{M-to-T}}(\phi_p^{(c)}, e^{(c)}), \end{aligned}$$

5.6 The Observation-Centered Filter, approach 2

In addition, represent the measurement error for the $\theta_{\text{obs}}(t)$ (true anomaly scale) in $\phi_{\text{obs}}(t)$ (mean anomaly scale) scale. Using the first order Taylor series the variance of a function can be written as,

$$\begin{aligned} X_{Fx} &\sim N(\mu_{Fx}, \sigma_{Fx}^2), \\ f(X_{Fx}) &\approx N(f(\mu_{Fx}), f'(\mu_{Fx})^2 \sigma_{Fx}^2), \end{aligned} \quad (5.3)$$

where, σ_{Fx}^2 is typically small and $f'(\mu_{Fx}) \neq 0$.

Using Equations (5.3) and 92.3), the variance for ϕ_{obs} can be written as,

$$\text{Var}(\phi_{\text{obs}}) \approx \left[\frac{(1 - e^{(c)^2})^{3/2}}{(1 + e^{(c)} \cos T^{(c)})^2} \right]^2 \text{Var}(\theta_{\text{obs}}).$$

(2) From Equation (3.6), (Section 3.5) the observed latitude can be written as,

$$\psi_{\text{obs}}(t) \approx A_1 \sin \theta_{\text{true}}(t) - A_2 \cos \theta_{\text{true}}(t), \quad (5.4)$$

where, θ_{true} (equivalent to θ) is computed using Equation (3.11) from the state vector (\mathbf{A}) (or from the *true* value). Further, for this step we treat $\theta(t)$ as a constant (at time t) for the one step update.

By performing the above mentioned steps, the observation matrix (\mathbf{H}) can be written as,

$$\mathbf{H} = \begin{bmatrix} 0 & 0 & 1 & 0 & 0 & 0 \\ \sin \theta_{\text{true}} & -\cos \theta_{\text{true}} & 0 & 0 & 0 & 0 \end{bmatrix} \quad (5.5)$$

Clearly, the tracking problem can be solved using a linear Kalman filter. Before discussing one example, we summarize both approaches (OCKF approaches 1 and 2).

The steps of the AST-OCKF algorithm can be summarized as follows.

Given

- a. The central state in Cartesian-ECI coordinates at time $t = 0$;
- b. The covariance matrix associated with the central state in Cartesian-ECI coordinate system;
- c. Sequence of angles-only measurements;

Computation

- 1) Find the CRTN frame;
- 2) Compute the initial mean state and its covariance matrix in AST-CRTN coordinates;
- 3) Transform angles-only measurements to the CRTN coordinates;
- 4) Propagate and update AST-CRTN state mean and variance using OCKF;
- 4.1) **Filtering stage 1:** Update the mean of the $A_3(t)$ using the OCUKF or OCEKF algorithm. Assume that the updated (or posterior) mean is denoted by $A_3^*(t)$;
- 4.2) **Filtering stage 2:** Use the updated mean or $A_3^*(t)$, obtained in previous step 4.1 as the prior mean along with other five AST-CRTN elements and perform EKF or UKF (6-to-2 mapping, 6 dimensional state vector to 2 dimensional observation vector) (approach 1) or a linear Kalman filter (approach 2);
- 5) Repeat stages 3) and 4) for each observation;

Algorithm 2: AST-OCKF stages

5.7 OCKF example

In this section, we discuss one example (Example 5.2.). The purpose of this example is to analyze performances of two proposed OC filters.

Example 5.2. One-step update. Assume an uncertain orbiting object with central eccentricity $e^{(c)} = 0.7$ and with initial relative standard errors $P_\sigma = 2.5\%$, $P_\tau = 10\%$ in Cartesian-ECI coordinates, the same as in Examples 2.1 and 2.2. For simplicity here assume the central inclination vanishes, $i^{(c)} = 0^\circ$ and the central angle of perigee is $\theta_p^{(c)} = 0^\circ$. Recall from (1.21) that the propagated variance of $A_3(t)$ increases linearly with t . Choose the propagation time $t = t_1$ large enough that the standard deviation of $A_3(t)$ equals $\xi_1 = 25^\circ$. Also suppose that the propagated mean of $A_3(t)$ is $\mu_x^{\text{Kalman}} = 260^\circ$. This value is chosen to highlight the non-linearity of $F_{T \rightarrow t_0 \rightarrow M}$.

Consider an angles-only observation with longitude $\theta_{\text{obs}} = 225.5^\circ$ and latitude

5.7 OCKF example

$\psi_{\text{obs}} = 0^\circ$ in the ASP-CRTN coordinate system, with measurement standard deviation $5.5e^{-04^\circ}$ (2 arc-seconds) for both. Note that the longitude of the observation, after transformation to the mean anomaly scale, takes the value

$$\phi_{\text{obs}} = F_{\text{T-to-M}}(225.5^\circ, 0.7) = 310^\circ,$$

which is located at the 2 s.d. distance of the propagated distribution for $A_3(t_1)$ since $\phi_{\text{obs}} = \mu_x^{\text{Kalman}} + 2\xi_1 = 260^\circ + 2 \times 25^\circ = 310^\circ$.

The propagated distribution for $A_3(t_1)$ forms the prior in the Bayesian update. Since the measurement standard deviation is very small (2 arc-seconds), the posterior mean for the $A_3(t_1)$ is concentrated very close to 310° . The results are summarized in Table 5.1. For the ‘‘Exact’’ entry in this table, the posterior mean and variance have been computed using a particle filter (Gustafsson *et al.*, 2002; Kent *et al.*, 2019b) with one million particles. Table 5.1 shows that the IUKF, OCKF-1 (using the first approach) and OCKF-2 (using the second approach) all give excellent approximations.

The ‘‘Exact’’ columns gives the correct answer showing that the posterior is highly concentrated about 310° . The IUKF, OCKF-1 and OCKF-2 filters are all similar to one another and provide the exact answer.

Table 5.1: Posterior means and standard deviations for $A_3(t_1)$ in Example 5.2., computed using various filters.

Moment	IUKF	OCKF-1	OCKF-2	‘‘Exact’’
mean (A_3)	310°	310°	310°	310°
s.d (A_3)	$3.2e-02^\circ$	$3.2e-02^\circ$	$3.1e-02^\circ$	$3.2e-02^\circ$

Chapter 6

Application of the propagated observation vector for solving association problems

6.1 Introduction

Recall the association problem discussed in the first chapter (see Section 1.11), in this chapter we provide several examples to illustrate the usefulness of the propagated observation vector in solving association problems. One practical use of the association problem is catalog maintenance (Moretti *et al.*, 2017; Siminski *et al.*, 2014) of various space objects. There are three different types of association problems (Bhattacharjee *et al.*, 2017a; Hussein *et al.*, 2015; Kent *et al.*, 2017a). The first one is the Observation-to-Track association problem (OTTA) (Faber *et al.*, 2017; Kent *et al.*, 2017a), where we want to associate an observation with a track (uncertain orbital state) with the help of historic information about the object from a library of space objects. The second type of association problem is the Observation-to-Observation association problem (OTOA), where we have a database of observations taken at different time intervals and we would like to determine whether any two or more observations are generated from the same space object. Final one is the Track-to-Track association problem (TTA) (Faber *et al.*, 2017; Kent *et al.*, 2017a), where we want to match uncorrelated tracks to see if any two or more tracks are generated from the same space object or not (Faber *et al.*, 2017; Kent *et al.*, 2017a). In this thesis, we solve the OTTA problem

for mainly two objects and we also discuss various test cases. In recent years, a significant number of research works have been performed on solving association problems for two or more number of space objects (in some cases for only a single object, Example 6.2). For instance, (Tchamova *et al.*, 2004) used their algorithm on two objects (plus two tracks and two observations) but (Moretti *et al.*, 2017) and (Hussein *et al.*, 2015) solved association problems for three and four objects respectively. To test the proposed methodology, we use a high amount of initial uncertainties and these ranges are much higher than the values used by other research works. For instance, the paper by (Pirovano *et al.*, 2020) used standard deviation of 0.5 arcsec for generating simulated observations and the paper by (Hussein *et al.*, 2015) used 100m in position and 10m/sec in velocity uncertainties (represented in Cartesian coordinates). The success rate depends on multiple factors (such as, initial uncertainties, methodology, single stage association vs. multiple stage association etc.). High initial uncertainties can often result in ambiguity in custody. Example 6.1 highlights one such issue. However, we solve this problem by using the multistage association or filtering-association (Example 6.4). In this chapter, we also demonstrate the usefulness of the PN-ASP setup by considering an object generated due to a break-up event.

6.2 Key contributions

There are three key contributions made in this chapter.

- (a) First, we discuss various concepts related to solving an association problem (Sections 6.4 to 6.7).
- (b) Second, we provide several examples to discuss various association problems (Section 6.8).
- (c) Third, we discuss an example to show the role of filtering in solving association (*filtering-association*) problem (Subsection 6.8.4).

6.3 Relation to other chapters

Chapter 1 discussed key concepts related to orbital dynamics. In Chapter 1, we also discussed standard astrodynamics coordinate systems. Chapter 2 introduced the AST-CRTN coordinate system to represent the propagated 6-dimensional orbital uncertainty and we used the AST-CRTN coordinate system for the filtering in Chapter 5. In Chapter 3, we talked about the ASP-CRTN coordinate system. This chapter will use these concepts to solve various association problems. We assume that the observation is measured in terms of the angles-only position (similar to the last chapter) and we use the propagated ASP-CRTN coordinate system. Recall, Section 3.6 in Chapter 3, various angles can be summarized as follows.

- (a) **Angle:** Latitude (ψ) (true observation).

Measurement scale: N.A.

Description: Non-normal during a break-up event.

- (b) **Angle:** Longitude (θ) (true observation).

Measurement scale: True anomaly.

Description: Non-normal if the propagation period is large and eccentricity is high.

- (c) **Angle:** Scaled or standardized latitude (ψ_1) (pseudo observation).

Measurement scale: N.A.

Description: Approximately normal.

- (d) **Angle:** Modified/re-invented break-angle (ϕ) (pseudo observation).

Measurement scale: Mean anomaly.

Description: Approximately normal.

6.4 Association problem

In this thesis, we use two different set-ups for solving association problems. These two set-ups are mentioned below.

- (1) **Fixed set-up association problems.** Recall Fig. 1.9, we use this set-up to associate points 1 and 2 with proper distributions. We discuss three possible test cases.
 - (a) Solving the association problem for a non break-up event.
 - (b) Solving the association problem for a break-up event.
 - (c) Solving the association problem for a mixture of break-up and non break-up events.
- (2) **Moving set-up association problems.** We need to use filtering to solve these type of problems. We discuss one such case in this thesis.
 - (a) Solving the association problem when the object custody is ambiguous.

The term *Moving set-up association problems* indicates that the object custody is ambiguous and the association problem cannot be solved in one stage and we need to use filtering to estimate information related to future stages. However, the term *Fixed set-up association problem* means that the association problem can be solved in one stage.

6.5 Discriminant analysis

Consider an angles-only observation \mathbf{z} on the unit sphere (in the ASP-CRTN coordinate system) which may come from one of J possible populations with densities $\triangleright f_j(\mathbf{z})$, $j = 1, \dots, J$. We allocate \mathbf{z} to the population for which $\triangleright f_j(\mathbf{z})$ is largest. Further, if we assume each population has equal prior probability, then the posterior probability that \mathbf{z} comes from population j is

$$\triangleright p_j(\mathbf{z}) = \frac{\triangleright f_j(\mathbf{z})}{\sum_{j'=1}^J \triangleright f_{j'}(\mathbf{z})}, \quad j = 1, \dots, J, \quad (6.1)$$

where $\triangleright f(\mathbf{z}) = \triangleright f(\psi, \theta)$.

6.6 Tail probability

There is one additional possibility to be considered, namely \mathbf{z} is not associated with any of the populations in the library.

After *transforming* to Gaussianity, let $D_{\text{Mahal}}^2(\mathbf{z})$ denotes the squared Mahalanobis distance between \mathbf{z} and the origin (distribution mean). Assuming the observation comes from the specified member of the library, $D_{\text{Mahal}}^2(\mathbf{z})$ follows a χ_2^2 distribution (the same as an exponential distribution with scale parameter 1/2) with tail probability

$$\triangleright P(\mathbf{z}) = \exp\left\{-\frac{1}{2}D_{\text{Mahal}}^2(\mathbf{z})\right\}. \quad (6.2)$$

Going back to the library of populations and an observation \mathbf{z} , we remove from consideration any population j for which $\triangleright P_j(\mathbf{z}) < \nu$, where ν is a small pre-chosen critical value, e.g. $\nu = 0.001$.

If all populations are removed from consideration, we are left with the conclusion that the observation \mathbf{z} is not compatible with any of the populations.

Note that, the difference between the Mahalanobis distance and the Euclidean distance is mentioned in the Appendix (Section B.3) using a suitable example.

6.7 Solving association problem for non break-up and break-up events

In this section, we discuss steps related to solving association problems for objects related to both break-up and non break-up events. First, we start with the non break-up scenario and then we move our focus to the break-up scenario.

6.7.1 Association problem related to the non break-up event

Solving the association problem for the non break-up event is straight forward. Key steps are mentioned below.

- (1) First, compute the probability density $\triangleright f_j(\psi, \theta)$ (see Section B.4) for the given observation with respect to each cluster or propagated distribution separately.

6.7 Solving association problem for non break-up and break-up events

- (2) Next, compute the posterior probability ($\triangleright p_j(z)$ or $\triangleright p_j(\psi, \theta)$).
- (3) Finally, compute tail probabilities using Equation (6.2).

6.7.2 Association problem related to the break-up event

Solving the association problem related to the break-up event requires few more extra computation steps and these steps are mentioned below. Recall the break-up event scenario, the first order approximation to the conditional variance drops to 0 whenever $T(t)$ is a multiple of π and this leads the “pinching problem”.

- (1) In the break-up scenario, $\psi(t)$ depends only on δ_3 and also on the $\theta(t)$ to first order. Hence the conditional distribution of $\psi(t)$ given $\theta(t)$ is

$$\psi(t)|\theta(t) \sim N(0, (\Sigma_{\delta_3}/C^2) \sin^2 \theta(t)). \quad (6.3)$$

- (2) Compute the density ($\triangleright f_j(\theta, \psi)$) and the posterior probability (Mardia *et al.*, 1979). Note that the joint density takes the form,

$$\triangleright f(\psi(t), \theta(t)) = \triangleright f(\theta(t)) f(\psi(t)|\theta(t)), \quad (6.4)$$

$$\triangleright f(\psi(t)|\theta(t)) = \triangleright f(\psi(t); 0, (\Sigma_{\delta_3}/C^2) \sin^2 \theta(t)), \quad (6.5)$$

where, Σ_{δ_3} denotes the variance associated with the third velocity vector ($\Sigma_{\delta_3} = \text{Var}(\delta_3)$) (Recall Chapter 2, where we defined A, B, C, and δ terms).

- (3) Compute tail probabilities.

6.7.3 Note on the distribution of longitude and the related density

As discussed in the previous chapter (Section 3.6) and also shown in the Appendix (A.2) that if the propagation period is large and/or initial uncertainties are large then the distribution of the longitude (θ) cannot be approximated using a bivariate normal distribution. These situations are rare but to deal with such situations, we suggest to use the modified break-angle or ϕ (see Chapter 2) rather than θ . Further, by using ϕ , computation steps related to the density function are mentioned below.

- (1) The Jacobian matrix (J) (Section 2.5.1) shows that $[n - n^{(c)}]$ is to first order a linear combination of ϵ and δ where the terms ϵ_3 and δ_3 do not appear (see 6.6). In particular, to first order the mean motion n has a normal distribution, $n \sim N(n^{(c)}, \rho^2)$, for some $\rho^2 > 0$.

$$[n - n^{(c)}] \approx (P_1C + P_2Q_1)\epsilon_1 + (-P_1B + P_2Q_2)\epsilon_2 + (P_1A + 2P_2A^2BC^2)\delta_1 + (P_2Q_3)\delta_2. \quad (6.6)$$

- (2) The derivative of the mean anomaly $M(t)$ with respect to the true anomaly $T(t)$ is given by

$$\frac{dM(t)}{dT(t)} = \frac{(1 - e^2)^{3/2}}{(1 + e \cos T(t))^2}. \quad (6.7)$$

- (3) Putting the pieces together yields the joint density for $(\psi(t), \theta(t))$

$$\triangleright f(\psi(t), \theta(t)) = \triangleright f(\theta(t)) \triangleright f(\psi(t)|\theta(t)). \quad (6.8)$$

where

$$\triangleright f(\theta(t)) = \triangleright f(\phi(t); \phi^{(c)}(t), t^2 \rho^2) dM(t)/dT(t). \quad (6.9)$$

6.8 Association problems

6.8.1 Example 6.1. Solving association problem for a non break-up event (association problem)

Consider a “library” containing two space objects, and suppose that based on earlier observations the predicted angular location for each object at the current time t can be summarized using the ASP-CRTN coordinate system.

In this example, we have two overlapping distributions (say, 1 and 2). The first distribution is generated from the LEO object ($e = 0.13$) mentioned in the Chapter 3 and is highlighted using green markers in Fig. 6.1. The propagation period is 0.4 orbital period and initial uncertainties are same as before. The second distribution is generated from the HEO object ($e = 0.7$) discussed in Chapter 2 and the distribution is shown using blue markers in Fig. 6.1. The

propagation period is 0.2 orbital periods. Four points, labeled A, B, C, and D (see Fig. 6.1) have been picked to illustrate different properties.

Point A lies midway between the two principal axes, but is close enough to the common mode to be compatible with both distributions. In particular, the posterior probabilities are nearly equal, $\triangleright p_1 = 0.47$, $\triangleright p_2 = 1 - \triangleright p_1 = 0.53$, indicating an inability to discriminate between the two objects. Further, neither tail probability is small, $\triangleright P_1 = 0.99$, $\triangleright P_2 = 0.99$, indicating compatibility with both objects.

Point B lies in the main body of the distribution for object 1, but not for object 2. Hence, the posterior probability that point B comes from object 1 is large ($\triangleright p_1 = 1.00$, $\triangleright p_2 = 1 - \triangleright p_1 = 1.14e^{-13}$). This conclusion is reinforced by the tail probabilities; $\triangleright P_2 = 3.38e^{-14}$ is very low, indicating that the observation is incompatible with object 2 and $\triangleright P_1 = 0.23$ is not low, indicating compatibility with object 1.

Point C lies in the body of the distribution for object 2, but appears to be an outlier for object 1. This interpretation is confirmed by the posterior probabilities ($\triangleright p_1 = 2.03e^{-03}$, $\triangleright p_2 = 1 - \triangleright p_1 = 0.99$) and by the tail probabilities ($\triangleright P_1 = 6.14e^{-05}$, $\triangleright P_2 = 0.038$).

Point D is an outlier, lying far from the predicted distributions for both objects. The tail probabilities are both very small, $\triangleright P_1 = 2.18e^{-67}$, $\triangleright P_2 = 5.93e^{-24}$, indicating an incompatibility with either object. Hence the posterior probabilities are not very meaningful in this case.

6.8.2 Example 6.2. Solving association problem for a break-up event (association problem)

The following example (Example 6.2.) is particularly a simple version of the association problem with one library object that has suffered a break-up event. Two observations have been made after approximately one orbital period. The question is whether either of these observations is compatible with the library object.

The upper panel in Fig. 6.2 is the same (in terms of the propagation period) as panel (b) in Fig. 3.2, with two possible observations marked in red. Horizontally

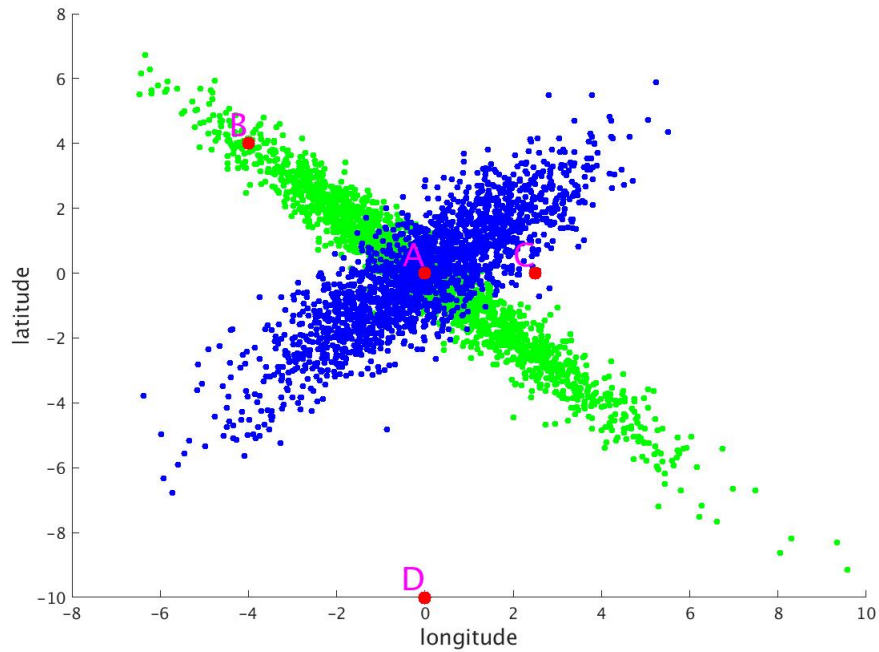


Figure 6.1: **Example 6.1., solving the association problem.** The association problem for two overlapping distributions 1 and 2. Observations are highlighted using red markers, a total of 4 observations are made.

they are equi-distant from 0, and their vertical values are identical. However, point A lies in the left-hand bulge whereas point B lies outside the right-hand bulge. The lower panel shows the data after transformation to bivariate normality. Now it can be clearly seen that point A is somewhat compatible with the bivariate normal distribution but that point B is far way.

This visual impression is confirmed by the tail probability values, equal to 0.07 and 0, respectively, confirming that point A is compatible with the propagated distribution; point B is extremely incompatible.

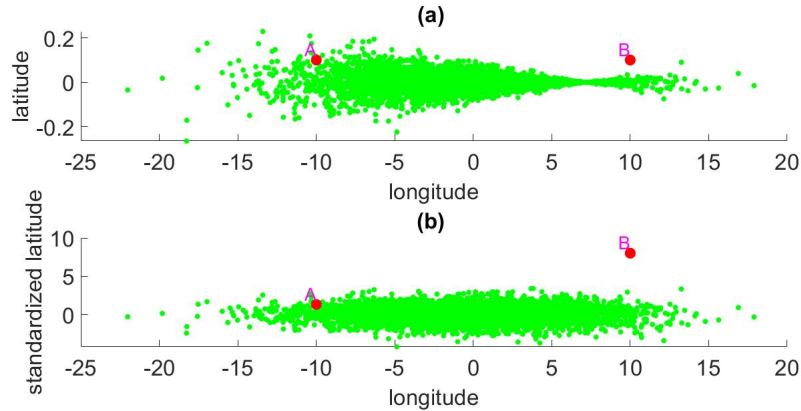


Figure 6.2: **Example 6.2., solving the association problem for a break-up event.** The upper plot is the same (in terms of the propagation period) as panel (b) in Fig. 3.2, with two observations superimposed. The lower plot (with scaled/standardized latitude representing the vertical axis) shows the transformation to bivariate normality. Point A is compatible with this distribution; point B is not.

6.8.3 Example 6.3. Solving the association problem for a mixture of break-up and non break-up events (association problem)

Consider a “library” containing two space objects. Among these two objects, one object is generated due to a break-up event and another object is related to a non break-up event. These two objects are same as the first example (Section 6.8.1), the only difference is that we are assuming that the first object is generated due to a break-up event by making the initial position uncertainty zero for this object. The first object is propagated for exactly 1 central orbital period and the second object is propagated for 0.2 orbital periods (same as before). However, initial velocity uncertainty is reduced for this object (for the visualization purpose).

As usual, the observation (A) is marked using a red marker and distributions 1 and 2 are marked using green and blue clusters respectively in Fig. 6.3. Clearly, distribution 1 suffers from the pinching issue. To associate the observation with the correct object, first we use steps mentioned in Section 6.7.1 to check the compatibility of point A with the distribution 2, see Subplots (a) and (b). Next,

we correct distribution 1 (corrected image is shown in Subplot (d)). Note that in Fig. 6.3 the vertical axis is representing the scaled/standardized latitude. Finally, we compute the tail probability. There is no need to compute posterior probabilities for this example.

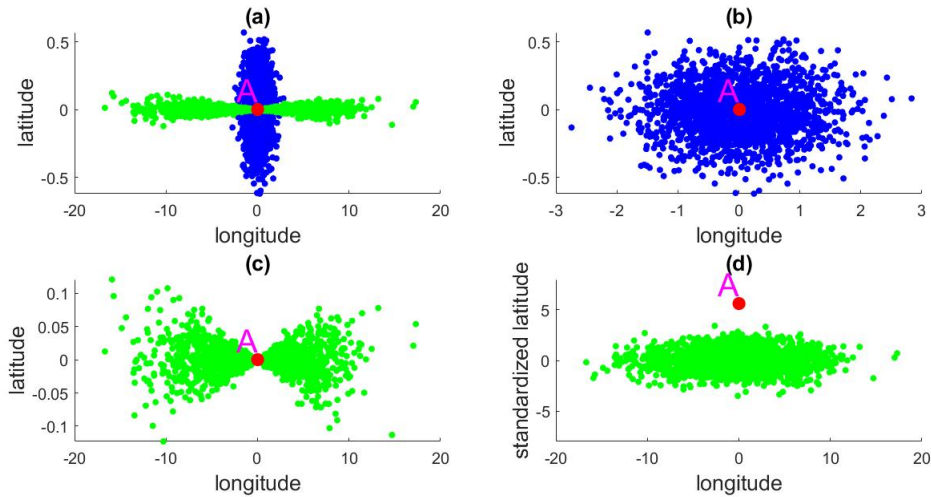


Figure 6.3: **Example 6.3., solving the association problem for for a mixture of break-up and non break-up events.** Two distributions and one single observation where the first object suffers from the pinching problem. The observation is located just outside the pinching zone or the center of the distribution 1. However, the observation is clearly part of the second distribution.

Note that the observation is located slightly higher than the center of the first distribution but clearly part of the second distribution. This interpretation is confirmed by the tail probabilities ($\triangleright P_1 = 2.43e^{-07}$, $\triangleright P_2 = 0.99$) and similar to the previous example there is no need to compute posterior probabilities.

6.8.4 Example 6.4. When the object custody is ambiguous (filtering-association problem)

Recall Fig. 6.1 (Subsection 6.8.1), posterior probabilities were nearly equal for point A. In this section, we use the filtering-association to associate the observation with the correct distribution. The filtering-association can be used in a situation where the object custody is ambiguous. Example 6.4. is a special case

and this example is a complicated version of the Example 6.1. In this example, we assume that normal directions ($\mathbf{h}^{(c)}$) are same for both objects.

In general, when object custody is ambiguous, some modification to this procedure (IUKF/OC filters) is needed. Suppose an object can be associated with two or more objects in a catalog at time t_k . Then the state distribution at time t_k is a mixture of two multivariate normal distributions. Sigma points (UKF sigma points) are constructed and propagated for each component of the mixture. The update step involves re-computing the sigma points as before, after which the updated state distribution is approximated by a new mixture of two multivariate normal distributions.

Example 6.4. To illustrate the procedure consider a situation with two objects at time $t = 0$. The first object is same as in the Chapter 2 (eccentricity = 0.7 and orbital period = 712 minutes). The second object is also located on a HEO orbit (eccentricity = 0.67 and orbital period = 655 minutes, $A = 9078$ km, $B = 2.5$ km/sec and $C = 8.1$ km/sec). The two (central) normal directions to the orbital planes are assumed to be the same (for both objects, $\mathbf{h}^{(c)} \propto [0, 0, 1]^T$ and $h^{(c)} = 73531$ km²/sec). The uncertainties are represented in ECI coordinates by isotropic normal distributions for position ($P_\sigma = 1\%$) and velocity ($P_\tau = 1\%$). The initial state vectors are represented in ECI, Keplerian, Equinoctial and AST coordinates in Figs 6.4-6.8. In general the one-dimensional plots are either unimodal or bimodal, depending on the extent of overlap of initial conditions.

Next we follow these two objects for four different time intervals ($t = 0, 200, 400$ and 600 minutes). Results are shown using Fig. 6.8.

From Fig. 6.8 several conclusions can be reached.

- (1) **(Subplot(a).)** Both distributions are highly overlapped and posterior probabilities are also same ($\triangleright p_1 = 0.5, \triangleright p_2 = 1 - \triangleright p_1 = 0.5$).
- (2) **(Subplot(b).)** Both distributions are still very much overlapped, posterior probabilities are not equal but close ($\triangleright p_1 = 0.53, \triangleright p_2 = 1 - \triangleright p_1 = 0.47$) and as a result it is not possible to allocate the observation to the correct distribution.

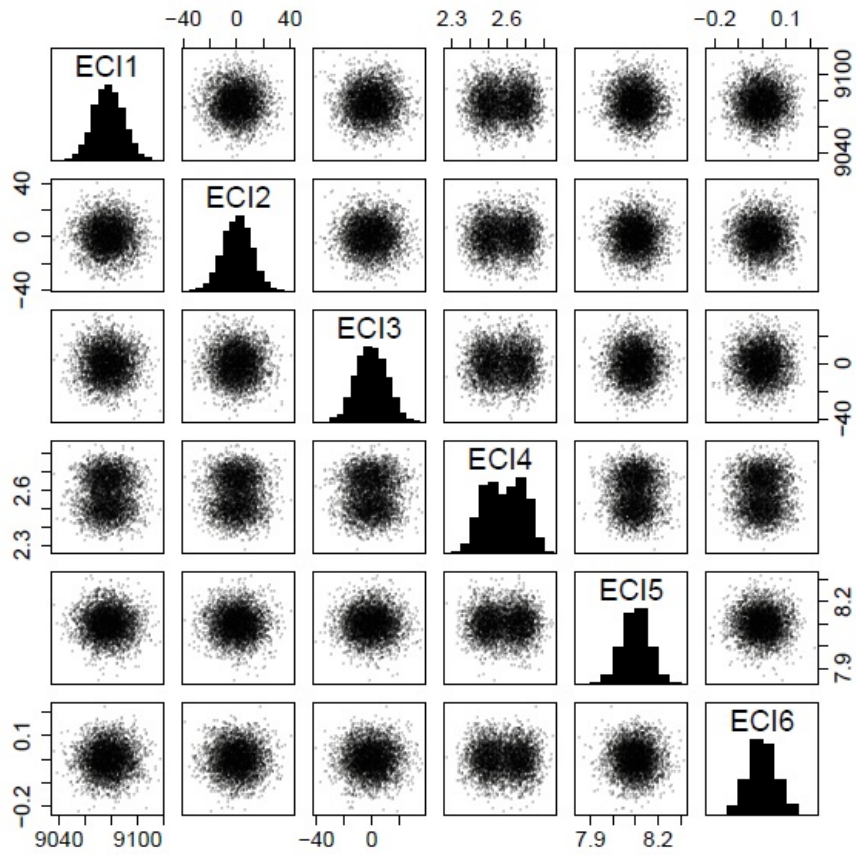


Figure 6.4: **Example 6.4., joint distribution in the Cartesian (CRTN) coordinate system at $t = 0$, part 1.** Initial point clouds ($N_A = 2000$ and $N_B = 2000$) for objects 1 and 2 represented in ECI coordinates.

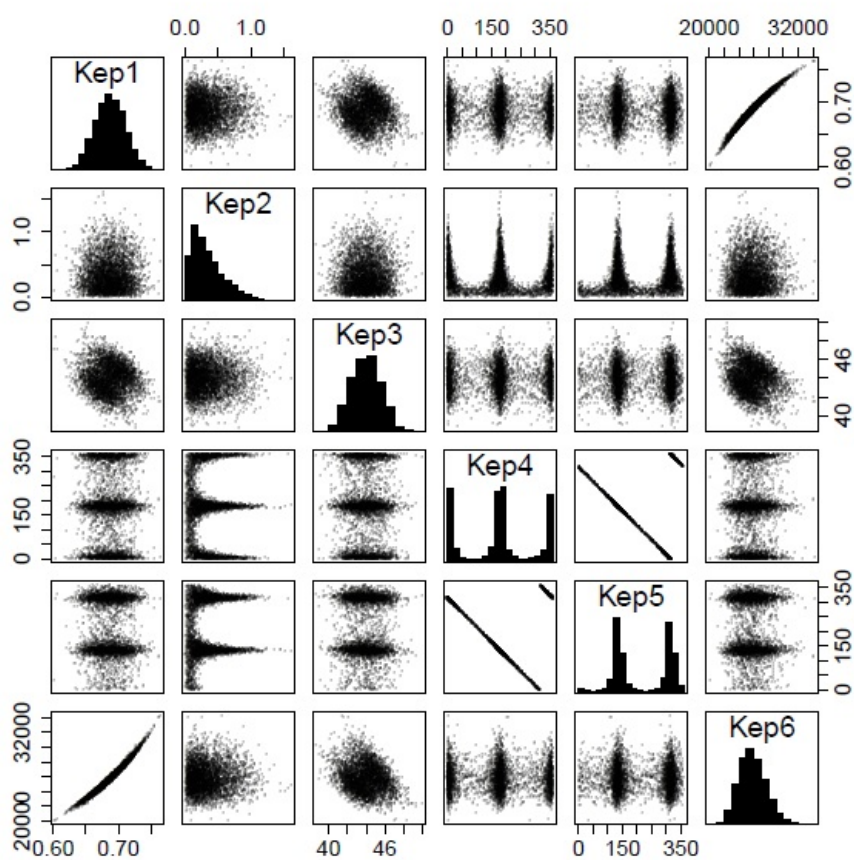


Figure 6.5: **Example 6.4., joint distribution in the Keplerian (CRTN) coordinate system at $t = 0$, part 2.** Initial point clouds ($N_A = 2000$ and $N_B = 2000$) for objects 1 and 2 represented in Keplerian coordinates.

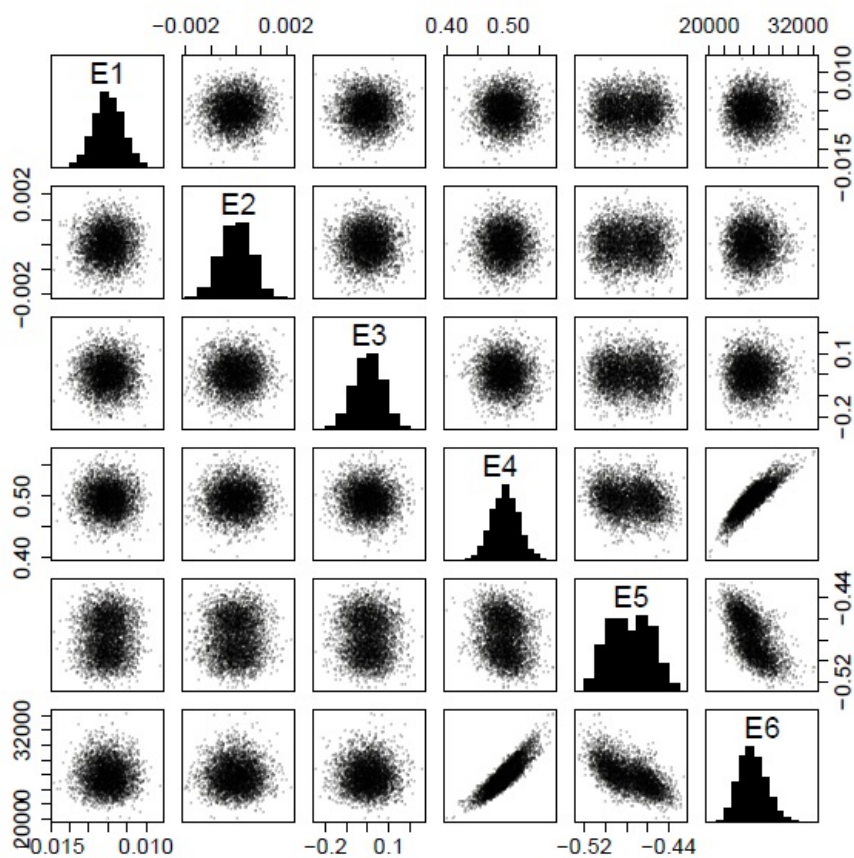


Figure 6.6: **Example 6.4.**, joint distribution in the Equinoctial (CRTN) coordinate system at $t = 0$, part 3. Initial point clouds ($N_A = 2000$ and $N_B = 2000$) for objects 1 and 2 represented in Equinoctial coordinates.

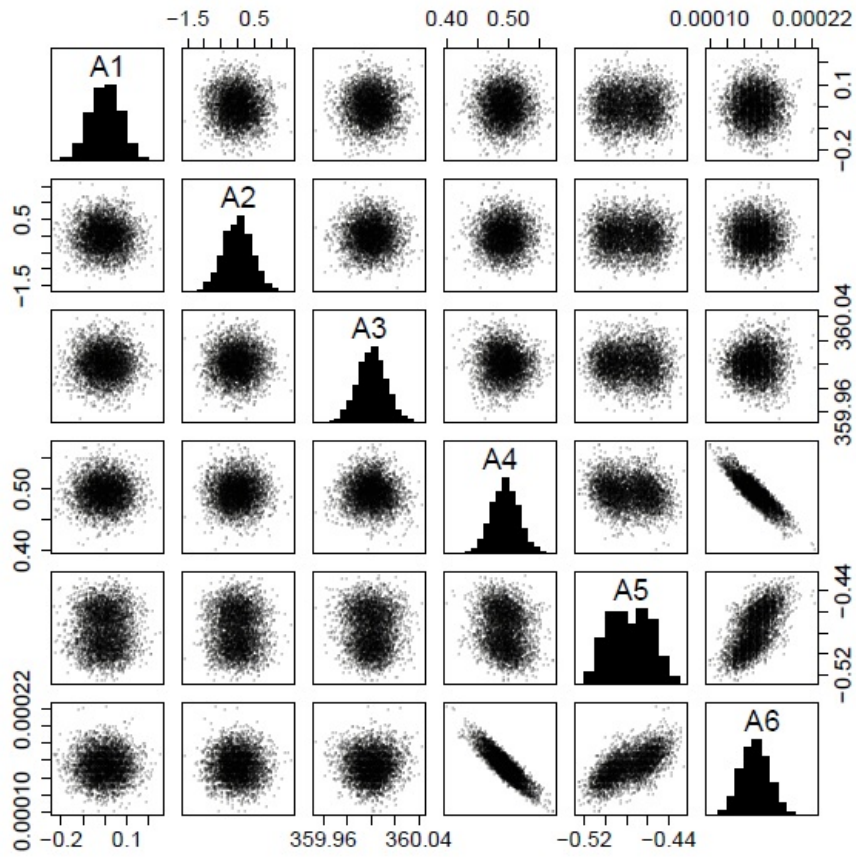


Figure 6.7: **Example 6.4., joint distribution in the AST (CRTN) coordinate system at $t = 0$, part 4.** Initial point clouds ($N_A = 2000$ and $N_B = 2000$) for objects 1 and 2 represented in AST coordinates.

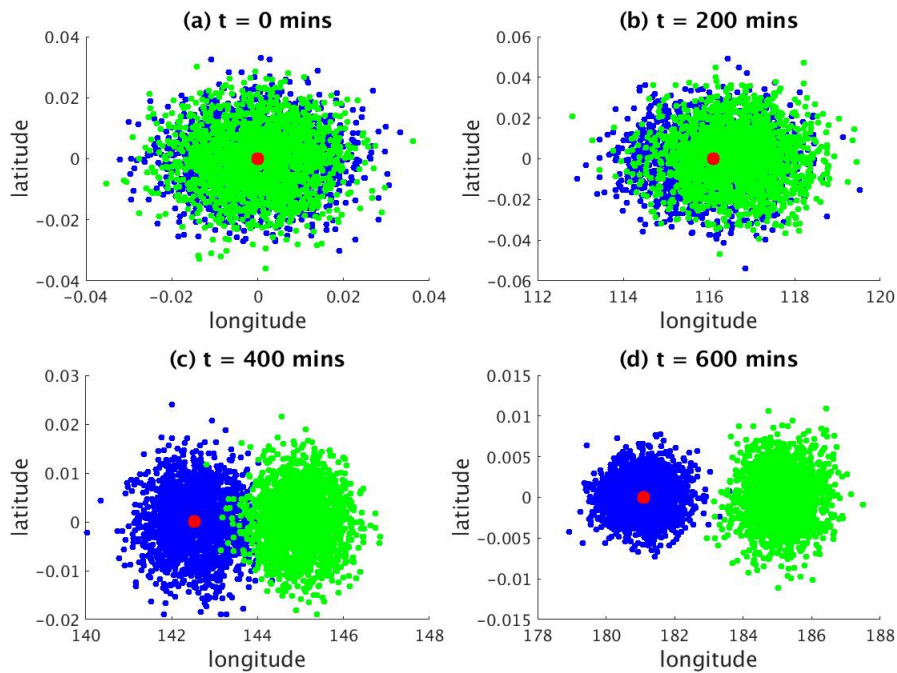


Figure 6.8: **Example 6.4., various filtering stages for ambiguity in custody problem, part 5.** Angles-only representation of the point cloud at $t = 0$. The blue cluster indicates the distribution associated with the first object (object 1) and the green cluster represents the second object (object 2). The red dot is the observation. Subplot (a), at $t = 0$, note the high degree of overlapping between the two distributions. Subplot (b), at $t = 200$ minutes, two distributions are still very much overlapped. Subplot (c), at $t = 400$ minutes, the observation is connected with the first distribution. Subplot (d), at $t = 600$ minutes, clearly the observation can be associated with the first distribution.

- (3) (**Subplot(c).**) The observation is part of the first distribution and posterior probability values provide evidence ($\triangleright p_1 = 0.99, \triangleright p_2 = 1 - \triangleright p_1 = 0.01$).
- (4) (**Subplot(d).**) The observation is clearly part of the first distribution and posterior probabilities confirm it ($\triangleright p_1 = 1, \triangleright p_2 = 1 - \triangleright p_1 = 0$).

Chapter 7

Conclusion and Future directions

7.1 Conclusion

Various issues related to the space object tracking and association problems are discussed in this thesis. The first chapter has set the theme of the thesis. This chapter has discussed various concepts related to the orbital dynamics and coordinate systems. In this chapter, the bounded range problem has been explained using a suitable example. The final part of this chapter briefly introduces the association and tracking problem.

Chapter 2 has discussed the non-linearity in the propagation equation in the Cartesian-ECI coordinate system. A first order Taylor series expansion has been used to represent the AST-CRTN deviations and it has been shown that AST-CRTN coordinates are approximately linear function of the Cartesian-CRTN deviations. This expansion has helped to explain why AST-CRTN coordinates are generally typically approximately Gaussian whatever the initial conditions are. Further, using linearity plots it has been shown that AST-CRTN coordinates are still approximately Gaussian, even under extreme initial uncertainties.

Chapter 3 has dealt with the representation of the propagated uncertainty associated with the angular position. At the beginning, a brief discussion has been provided to introduce the ASP-CRTN coordinate system. If the propagation period is not too extreme or not a close multiple of half orbital period then the joint distribution of the propagated angles-only position can be approximated using a bivariate normal distribution. However, an important special scenario is

a break-up event where there is uncertainty only in initial velocity, but not in position. In this case, the distribution of the propagated latitude and longitude has showed a distinctive “bow-tie” effect whenever the propagated time is an integer multiple of the half-period. This “pinched normal” distribution can be transformed to a standard bivariate normal distribution. The final portion of this chapter has investigated the distribution of the radial component. However, the distribution of the radial component can be turned into an approximate normal if a correct scaling factor is used.

Chapters 4 and 5 have discussed the tracking problem. Further, the development of the fifth chapter has been (partially) based on the second chapter. The overall tracking problem deals with two types of non-linearity. The first type of non-linearity is associated with the propagation equation, which has been mentioned in the second chapter and resolved by using the AST-CRTN coordinate system. The second type of non-linearity arises from the non-linear relationship between the true and the mean anomaly. The relation between the true and the mean anomaly depends on the orbital eccentricity. For example, for a circular ($e = 0$) or near circular orbit the function F_{M-t_0-T} is linear (approximately). This chapter has compared various Kalman filters using suitable 1-dimensional examples. In addition, the usefulness of the AST-CRTN coordinate system has been illustrated for solving the 6-dimensional tracking problem. The final portion of the Chapter 5 has discussed two approaches for using the Observation-Centered Kalman filters for solving the 6-dimensional space object tracking problem.

Chapter 6 has discussed the usefulness of the ASP-CRTN coordinate system and the newly developed PN distribution. Three different examples have been used to discuss the association problem under varying conditions. In addition, this chapter has also mentioned the filtering-association problem for solving the object custody problem.

To summarize, this thesis has investigated various issues related to the orbital uncertainty analysis and tracking. The AST coordinate system is the localized version of the equinoctial coordinate system and it has been developed to overcome the limitations of the equinoctial coordinate system. This thesis also highlights various facts related to the propagated uncertainty associated with the angular position and the radial component. The distribution of the latitude is

non-normal if the object is generated due to a break-up event. Besides, the distribution of the radial component can often behave as non-normal. This thesis has discussed these two distributions in detail. In particular, standardization is sometimes needed to ensure the Gaussianity of the distributions of the latitude and the inverse radial distance. These results have been combined to compute a one-step update for the tracking problem using the OCKF. The newly developed OCKF works perfectly with a wide variety of initial conditions that can cause problems for other available methods and by using an OCKF the tracking problem can be solved using a linear Kalman filter.

7.2 Future directions

Previous chapters discussed my contributions related to this project. This chapter illustrates some of my other works which are partially developed and require more attention in the future. In this chapter, we will discuss two of such topics. Note that we have performed explorative analysis on these topics and discuss results in this chapter but detailed analysis needs to be performed to understand various reasons.

- (1) Observer-centric representation (origin is at the location of the observer) of the propagated angles-only point cloud.
- (2) Analyzing sensitivity of various multivariate normality tests.

7.3 Observer-centric analysis on the propagated angles-only position vector

As of now, we performed all our analyses by assuming that the observer is located at the center of the earth. However, we have also performed a structural analysis on the *observer-centric* observation. The term *observer-centric* indicates that the observer is located at the surface of the earth. The distribution of the propagated true angular elements (or the true angles) in an observer-centric frame of reference mainly depend on two parameters and they are listed below.

7.3 Observer-centric analysis on the propagated angles-only position vector

- (1) **Altitude:** An object located at the GEO orbit remains largely unaffected by the observer-centric observation and the joint distribution of the latitude (or scaled latitude) and the longitude can be approximated using a bivariate normal distribution. See Example 7.1. for more details. However, the change of frame (or the location of the observer) from the earth-centric to the observer-centric has major impact on an object residing at the LEO orbit.
- (2) **Propagation period:** The observer-centric reference frame (or observation) has less severe effect on the joint distribution of the propagated angular uncertainty, if the propagation period is very small and/ or initial uncertainties are also small. Example 7.2. provides further details.

7.3.1 Example 7.1. Observer-centric analysis based on altitude

This section provides two examples to show the impact of the observer-centric frame of reference for analysing the propagated angular uncertainty. The purpose of this section is to understand the role of observer-centric observation in uncertainty propagation and normality analysis.

Consider two orbiting objects, the first object is located at the LEO orbit (the object which we used in Chapter 3, Example 3.1.) and the second object is located at the GEO orbit ($A = 42167$ km, $B = -5.38e^{-04}$ km/sec, $C = 3.075$ km/sec). The LEO cloud is propagated for exactly 1 central orbital period (equivalent to 131 minutes) and the GEO cloud is also propagated for 1 central orbital period (equivalent to 1436 minutes). The final assumption is that the observer is located at the $[6000$ km, $0, 0]$ location. The propagated angular uncertainties for the LEO and GEO clouds are shown in Figs 7.1 and 7.2. Initial uncertainties are 1% each (i.e., $P_\sigma = 1\%$) ($P_\tau = 1\%$).

The joint distribution in Fig. 7.1 cannot be approximated using a bivariate normal distribution (p-values obtained using Mardia's test are $2e^{-07}$ and $1.7e^{-12}$ for the skewness and kurtosis respectively. Note that Shapiro-Wilk's test confirm the univariate non-normal behaviors with p-values $< 2e^{-16}$ and 0.0143 for the longitude and the latitude respectively). However, the joint distribution in

7.3 Observer-centric analysis on the propagated angles-only position vector

Fig. 7.2 is approximately a bivariate normal (Mardia's test results: p-value for skewness- 0.51, p-value for kurtosis- 0.25. Shapiro-Wilk's test results: p-value for the longitude- 0.69, p-value for the latitude- 0.41).

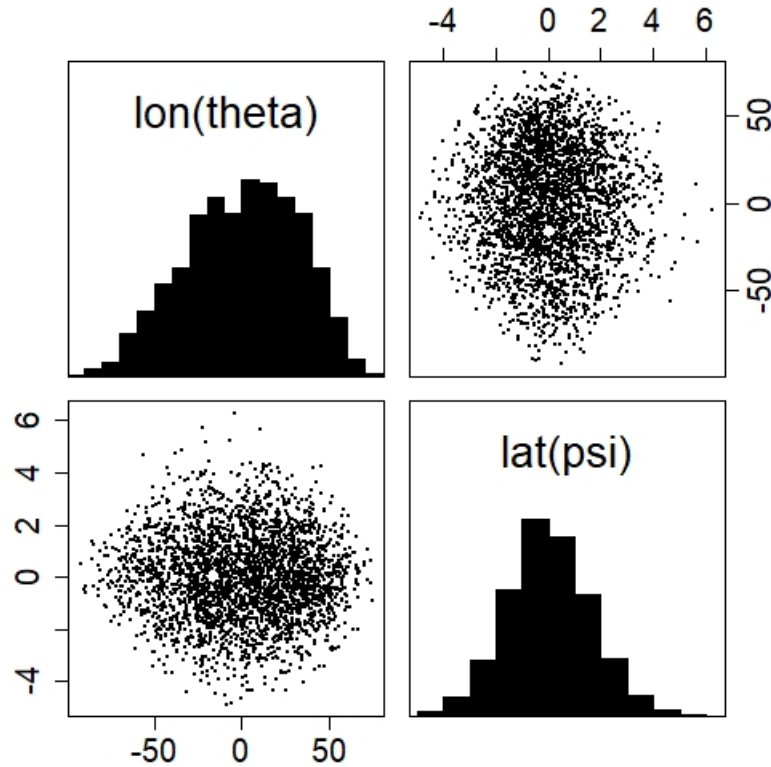


Figure 7.1: **Example 7.1., observer-centric propagation analysis for a LEO object.** In this example, a LEO object is propagated and the propagated angular uncertainties are represented using the observer-centric frame of reference (or observation). The joint distribution is clearly non-normal.

7.3.2 Example 7.2. Observer-centric analysis based on the propagation period

In this example (Fig. 7.3), the propagation period is reduced to 0.1 orbital period for the same LEO object (Fig. 7.1) which was used in Example 7.1. (other

7.3 Observer-centric analysis on the propagated angles-only position vector

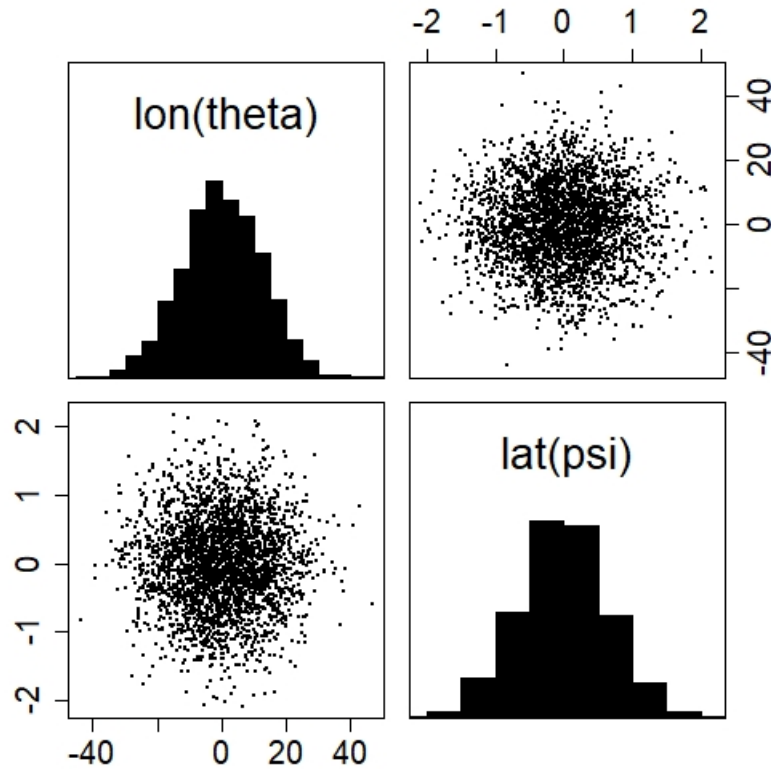


Figure 7.2: **Example 7.1., observer-centric propagation analysis for a GEO object.** In this example, a GEO object is propagated for 1 central orbital period and the propagated angular uncertainties are represented using the observer-centric frame of reference. The joint distribution is approximately normal.

conditions are same as before). Notice that the joint distribution of two angular component is approximately normally distributed. Further, this can also be confirmed by computing p-values (Mardia's test results: p-value for skewness- 0.87, p-value for kurtosis- 0.28. Shapiro-Wilk's test results: p-value for the longitude- 0.62, p-value for the latitude- 0.74).

7.3 Observer-centric analysis on the propagated angles-only position vector

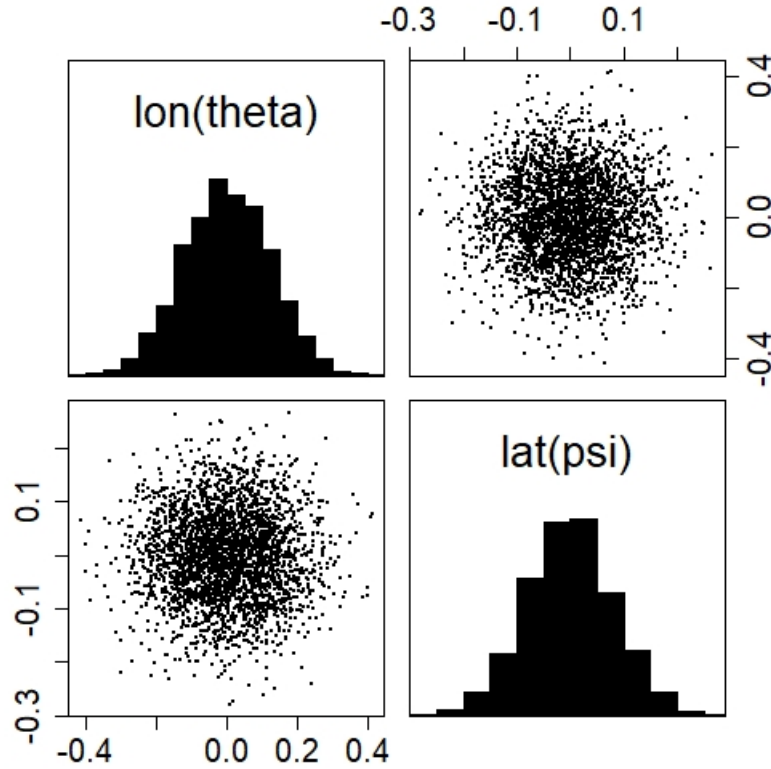


Figure 7.3: **Example 7.2., observer-centric propagation analysis for a LEO object with short propagation time.** In this example, we use the same LEO object which we used in Fig. 7.1. However, the propagation period is reduced. In this example the propagation period is 0.1 orbital period (equivalent to 13.1 minutes). Clearly, the joint distribution of the latitude and the longitude is approximately a bivariate normal.

7.3.3 Remarks

- (1) Objects located at the GEO orbit generally do not affected by the Observer-centric observation but LEO objects are very sensitive.
- (2) The best way to avoid any issue with the normality analysis in the propagated point cloud is to covert back to the Earth-centered reference frame. However, more research work needs to be carried out in the future.

7.4 Analyzing sensitivity of various multivariate normality tests

We used Mardia’s multivariate normality test to quantify approximate multivariate normality in Chapters 2 and 3. However, we also used Shapiro-Wilk’s normality test to judge AST coordinates statistically (to check univariate normality). In this section, we have performed an explorative study to understand the behavior of various normality tests, i.e., how reliable (able to capture slightest amount of non-normality) they are under extreme conditions. The MVN package (Korkmaz *et al.*, 2014) in R contains a list of normality tests.

This section compares performances of three normality tests. They are Mardia’s p-value test (provides two p-values, one for the skewness and another for the kurtosis) (Mardia, 1970; Mardia *et al.*, 1979), Henze-Zirkle’s p-value test (Henze & Zirkler, 1990)(provides one p-value) and Shapiro-Wilk’s univariate normality test (tests are performed for both the latitude and the longitude separately). We use the same HEO object, which was considered in Chapter 2. Further, we restrict our view to the propagated angles-only observation vector and we consider two different propagation periods (25 and 60 days respectively). In addition, initial uncertainties are kept almost same as before. Results are shown using Figs. 7.4 (Example 7.3.) and normality test values are summarized in Table 7.1.

From Fig. 7.4, we can see that both the joint distributions are mildly non-normal. For the first Subplot (a), even though non-normality is visible (non normality in the longitude due to the wrapping effect) but p-value test designed by Henze-Zirkle is unable to capture it. However, Shapiro-Wilk’s test is able to classify the distribution of the longitude as non-normal and Mardia’s p-value test also classify the joint distribution as non-normal. The second joint distribution (Subplot (b)) is also not normal (again, the longitude is not normal due to the wrapping issue). However, Mardia’s test is unable to classify the joint distribution as non-normal but Henze-Zirkle’s test can identify the joint distribution as non-normal. Further, Shapiro-Wilk’s univariate test confirms the non-normality in the longitude.

7.4 Analyzing sensitivity of various multivariate normality tests

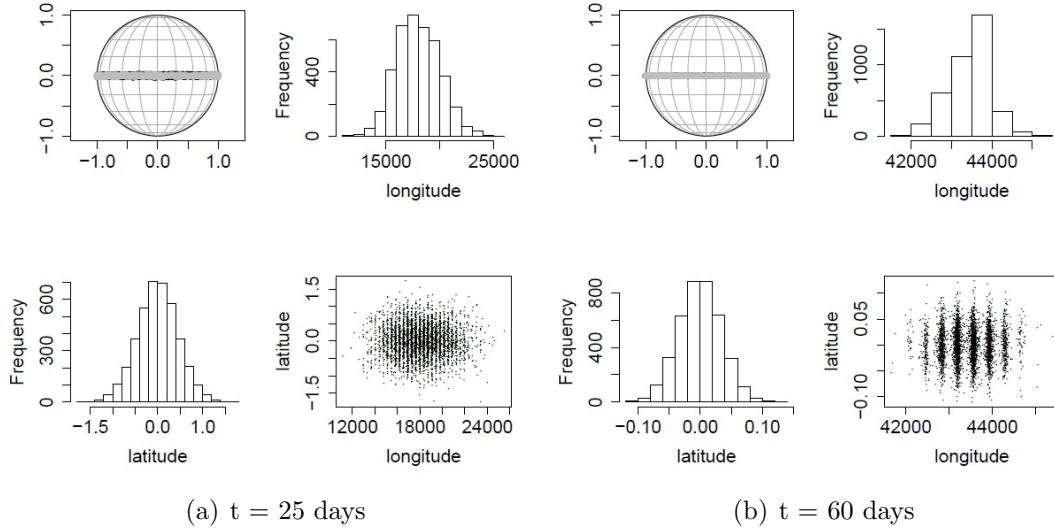


Figure 7.4: **Example 7.3., multivariate sensitivity analysis.** Analyzing sensitivity of different multivariate normality tests. In both subplots, the plot at the upper left shows a spherical representation of the point cloud. The remaining plots show histograms (true angles) and a scatter plot for the longitude (unit - degree) and latitude (unit - degree). Note that we use unwrapped longitude in both subplots. The term unwrapped means we are treating the longitude as a number rather than an angle. Notice that both subplots are non-normal. Results are discussed in Table 7.1

Table 7.1: Here “M. p-val. 1” and “M. p-val. 2” denote multivariate p-values for skewness and kurtosis respectively computed using Mardia’s MVN p-value computation method. “Hz p-val” indicates p-value obtained using the Henze-Zerkler’s MVN computation. Finally, “Lon. p-val.” and “Lat. p-val” indicate p-values for the longitude and latitude respectively computed using the Shapiro-Wilk’s test.

Subplot No.	M. p-val. 1	M. p-val. 2	HZ p-val.	Lon. p-val.	Lat. p-val.
a	$3.10e^{-03}$	0.22	0.07	$4.40e^{-07}$	0.73
b	0.95	0.23	$1.66e^{-15}$	$< 2.2e^{-16}$	0.81

Appendix A

More on orbital dynamics

A.1 Orbital dynamics

Recall Chapter 1 (Section 1.7), we discussed various orbital elements, coordinate systems and orbits. This chapter intends to provide a few more details on various orbital elements. Note that some of the elements are already discussed in the Chapter 1 but we provide further details in this section. In particular, we discuss the transformation from the Cartesian to the Keplerian coordinate system.

Our aim is to compute various orbital elements for an object in the sky for which the initial states (given in the Cartesian coordinate system) are exactly known (position \mathbf{x} (x_1, x_2, x_3) and velocity $\dot{\mathbf{x}}$ ($\dot{x}_1, \dot{x}_2, \dot{x}_3$)), various orbital elements can be written as follows (Curtis, 2006; Roy, 2004).

Note. Note that Section 1.7.3 discussed some of the orbital elements briefly but in this portion we wish to provide more details.

- (1) The radial distance (r) and the speed (v) can be computed as follows,

$$r = \sqrt{\mathbf{r} \cdot \mathbf{r}} = \sqrt{\mathbf{x} \cdot \mathbf{x}} = \sqrt{x_1^2 + x_2^2 + x_3^2},$$
$$v = \sqrt{\mathbf{v} \cdot \mathbf{v}} = \sqrt{\dot{\mathbf{x}} \cdot \dot{\mathbf{x}}} = \sqrt{\dot{x}_1^2 + \dot{x}_2^2 + \dot{x}_3^2}.$$

- (2) The radial velocity (v_r) indicates whether the object flying away ($v_r > 0$) or towards ($v_r < 0$) the perigee,

$$v_r = \frac{\mathbf{r} \cdot \mathbf{v}}{r}.$$

(3) The specific angular vector and its magnitude are,

$$\begin{aligned}\mathbf{h} &= \mathbf{r} \times \mathbf{v}, \\ h &= \sqrt{\mathbf{h} \cdot \mathbf{h}}.\end{aligned}$$

(4) The inclination angle takes the following form,

$$i = \cos^{-1} \frac{h_z}{h}.$$

(5) The node vector (also defines the node line) and its magnitudes are,

$$\begin{aligned}\mathbf{N}_{\text{RAAN}} &= \mathbf{w} \times \mathbf{h}, \\ N_{\text{RAAN}} &= \sqrt{\mathbf{N}_{\text{RAAN}} \cdot \mathbf{N}_{\text{RAAN}}}.\end{aligned}$$

(6) The eccentricity vector and the eccentricity value can be computed as,

$$\begin{aligned}\mathbf{e} &= \frac{1}{\mu} \left(\mathbf{v} \times \mathbf{h} - \mu \frac{\mathbf{r}}{r} \right), \\ e &= \sqrt{\mathbf{e} \cdot \mathbf{e}}.\end{aligned}$$

(7) The RAAN angle is computed as,

$$\begin{aligned}\Omega &= \cos^{-1} \frac{N_x}{N_{\text{RAAN}}}, \quad (N_y \geq 0), \\ \Omega &= 360^\circ - \cos^{-1} \frac{N_x}{N_{\text{RAAN}}}, \quad (N_y < 0),\end{aligned}$$

see Fig. A.1 for further details.

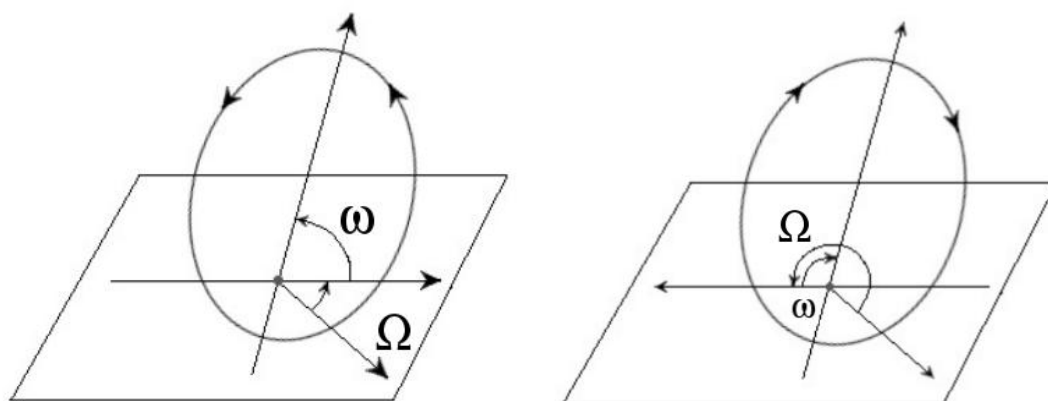
(8) The argument of perigee is,

$$\begin{aligned}\omega &= \cos^{-1} \frac{\mathbf{N}_{\text{RAAN}} \cdot \mathbf{e}}{N_{\text{RAAN}} e}, \quad (e_z \geq 0), \\ \omega &= 360^\circ - \cos^{-1} \frac{\mathbf{N}_{\text{RAAN}} \cdot \mathbf{e}}{N_{\text{RAAN}} e}, \quad (e_z < 0),\end{aligned}$$

see Fig. A.1 for further details.

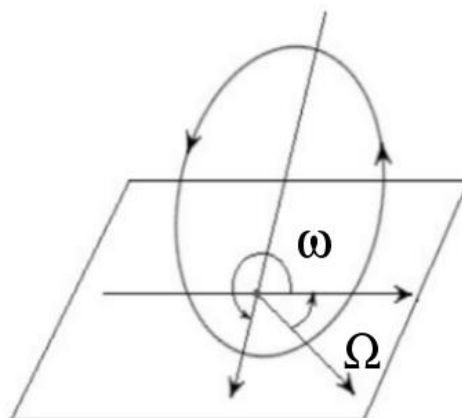
(9) Finally, the true anomaly (measured from the perigee) is,

$$\begin{aligned}T &= \cos^{-1} \frac{\mathbf{e} \cdot \mathbf{r}}{er}, \quad (v_r \geq 0), \\ T &= 360^\circ - \cos^{-1} \frac{\mathbf{e} \cdot \mathbf{r}}{er} \quad (v_r < 0).\end{aligned}$$



(a) $\omega, \Omega < 180^\circ$

(b) $\omega < 180^\circ, \Omega > 180^\circ$



(c) $\omega > 180^\circ, \Omega < 180^\circ$

Figure A.1: **Examples to show various values of the RAAN and the argument of Perigee (Not scaled to size).** (a) For the first image both the ω and Ω values are $< 180^\circ$ and the direction of motion is anti-clock wise. For the second image $\Omega > 180^\circ$ but $\omega < 180^\circ$ and the direction of motion is clock-wise. (c) For the third image $\omega > 180^\circ$ but $\Omega < 180^\circ$ and the direction of motion is anti-clock wise like the first image.

A.2 More examples (propagation)

This portion provides few more propagation examples. The main purpose of this section is to highlight the behavior of various coordinate elements under varying conditions. Total four examples are presented.

- (1) Cartesian-CRTN coordinate system under short-term propagation and small initial uncertainties.

Purpose: To show that the Cartesian coordinate system is able to preserve normality if the propagation period and/or initial uncertainties are small.

- (2) Keplerian-CRTN coordinate system for a near circular orbit.

Purpose: To show that if the orbit is circular or near circular ($e = 9e^{-05}$, $A = 7113$ km, $B = 4e^{-03}$ km/sec, $C = 7.47$ km/sec, for the purpose of this example, the amount of initial uncertainties are not relevant) then several Keplerian coordinate elements behave poorly (bounded range problem and/or singularity). Note that we also show the propagated uncertainty using the AST-CRTN coordinate system.

- (3) Propagated angles-only position vector for a HEO orbit when the propagation period is large.

Purpose: To show that θ or the longitude is non-normal if the propagation period is large.

- (4) Propagated angles-only position vector for a near circular LEO orbit.

Purpose: To show that θ and ϕ are almost identical.

A.2.1 Cartesian-ECI coordinate system under short term propagation

Fig. A.2 shows the propagated Cartesian-ECI coordinate system under small term propagation. In this example, we use the same object which was used in Chapter 2 (HEO object with $e = 0.7$). The propagation time is 0.1 central orbital period (*reduced*) and initial uncertainties are 0.1 times of the previously used uncertainties (*also reduced*). This example shows that if the propagation period

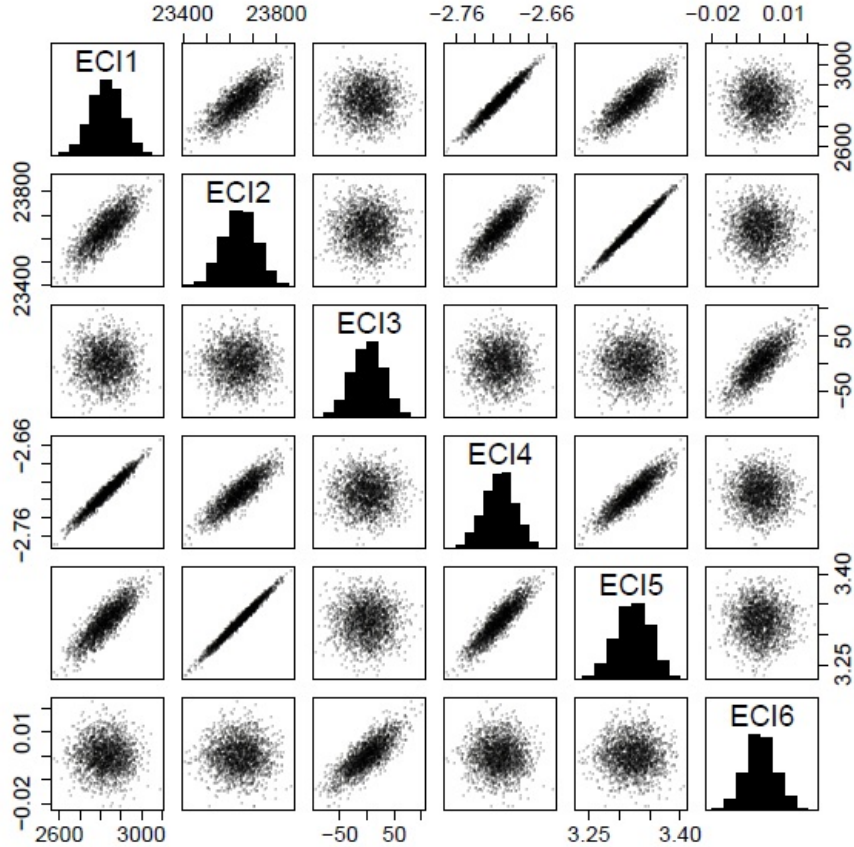


Figure A.2: **Propagated Cartesian-ECI coordinates for small-term propagation.** All the coordinates are approximately normal.

is small and initial uncertainties are also small then the propagated point cloud in the Cartesian-ECI coordinate system is approximately normally distributed.

A.2.2 Keplerian coordinate system for a near circular orbit

Figs. A.3 and A.4 show the propagated Keplerian-CRTN and AST-CRTN coordinate systems for a near circular orbit at the propagation time $t = 0$. The purpose of this example is to highlight the bounded range problem for the Keplerian coordinate system. Note that since the orbit is near circular ($e \approx 0$)

A.2 More examples (propagation)

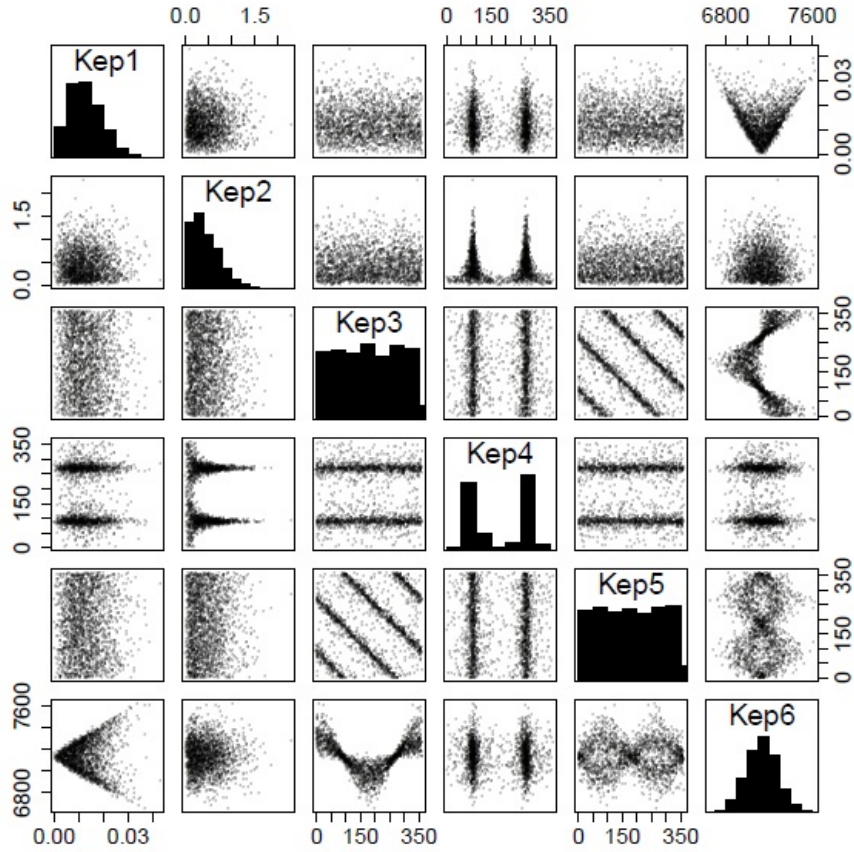


Figure A.3: **Keplerian-CRTN coordinates for a near circular orbit at $t = 0$.** Most of the elements are non-normal.

and the initial inclination is also 0 ($i = 0^\circ$ due to the construction), both these elements suffer from the bounded range problem. In addition, the distribution of the true anomaly ($T(0)$) is also not normal as perigee is ill-defined. However, all the AST-CRTN elements are approximately normally distributed (see Fig. A.4).

A.2 More examples (propagation)

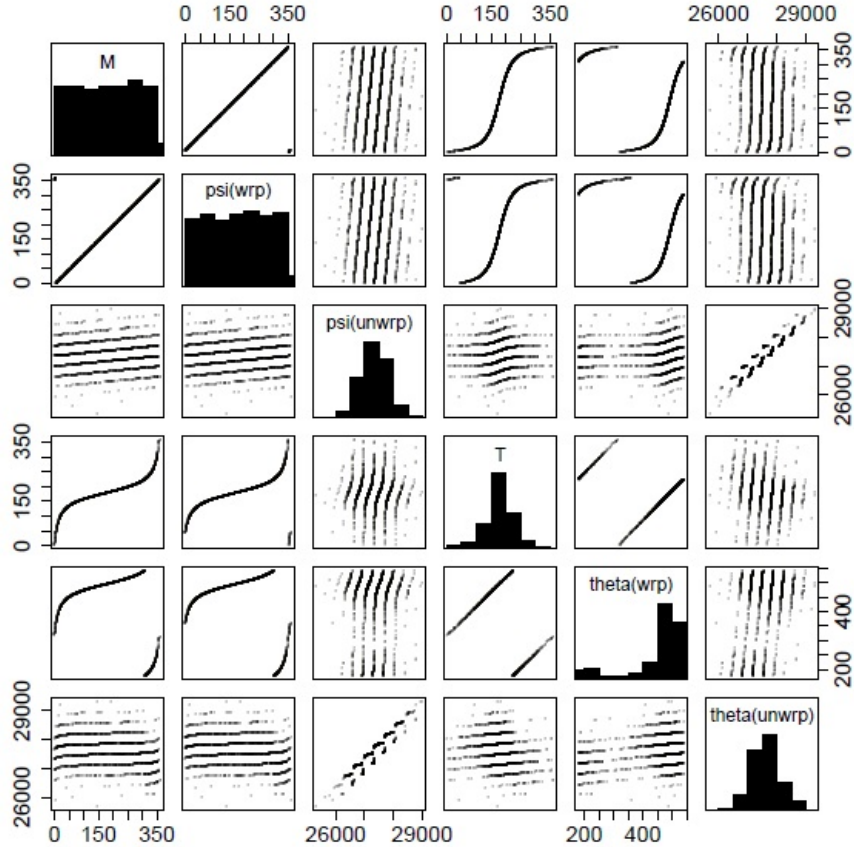


Figure A.5: **Propagated angles-only position vector for a HEO orbit when the propagation period is large.** Notice that the distribution of the unwrapped ϕ is approximately normal. However, unwrapped θ is not normal. Further, look at the scatter plot (1,4), it exactly shows the non-linear pattern which we discussed in the Chapter 5.

- (2) The wrapped ϕ is uniformly distributed but wrapped θ is not and the distribution of the wrapped θ depends on the starting location (like the true anomaly).
- (3) The unwrapped ψ is approximately normal but unwrapped θ is not.

A.2.4 Propagated angles-only position vector for a near circular LEO orbit

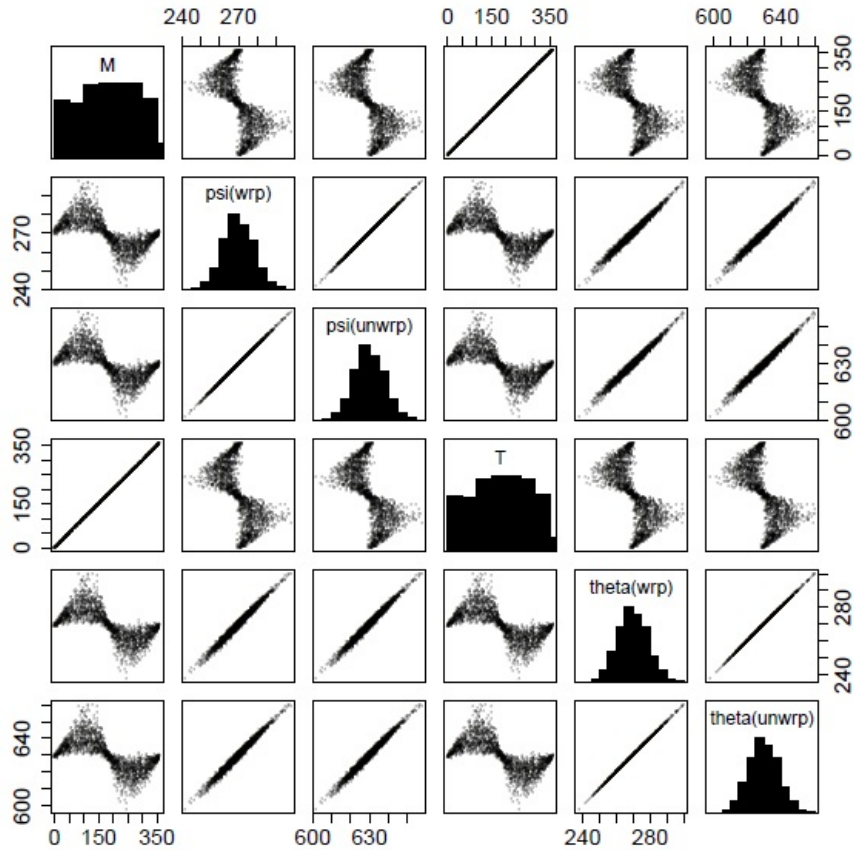


Figure A.6: **Propagated angles-only position vector for a circular LEO orbit.** Since the perigee is ill-defined for a circular orbit, distributions of the true and mean anomaly are no longer behave as normal. However, notice that both $\phi(t)$ and $\theta(t)$ are approximately normal. The orbit is not exactly circular ($e = 9e^{-05}$) but a near circular orbit and distributions of θ and ϕ are nearly the same.

In this portion, we judge distribution of various angular elements in a near circular orbit. Of course, the perigee is ill-defined and as a result both the mean and the true anomalies cannot be approximated using a normal distribution. However, the longitude θ and the remapped break-angle ϕ (A_3) do not suffer

A.3 True anomaly vs. mean anomaly for various eccentricity values ($F_{M\text{-}t\text{o-}T}$ function)

from any such issues. Further, ranges (standard deviations) for the θ and ϕ are similar (as $e \approx 0$).

A.3 True anomaly vs. mean anomaly for various eccentricity values ($F_{M\text{-}t\text{o-}T}$ function)

In this section, we show the relationship between the true anomaly and the mean anomaly for varying eccentricity values. A total of 10 eccentricity values (starting from 0 and ending at 0.9 with intervals 0.1) are considered. From Fig. A.7, we can see that when the eccentricity is 0 both the true anomaly and the mean anomaly are same. Further, for a small eccentricity value the relation between true anomaly and mean anomaly is approximately linear (or $F_{M\text{-}t\text{o-}T}$ function is approximately linear). However, non-linearity is clearly visible for higher eccentricity values.

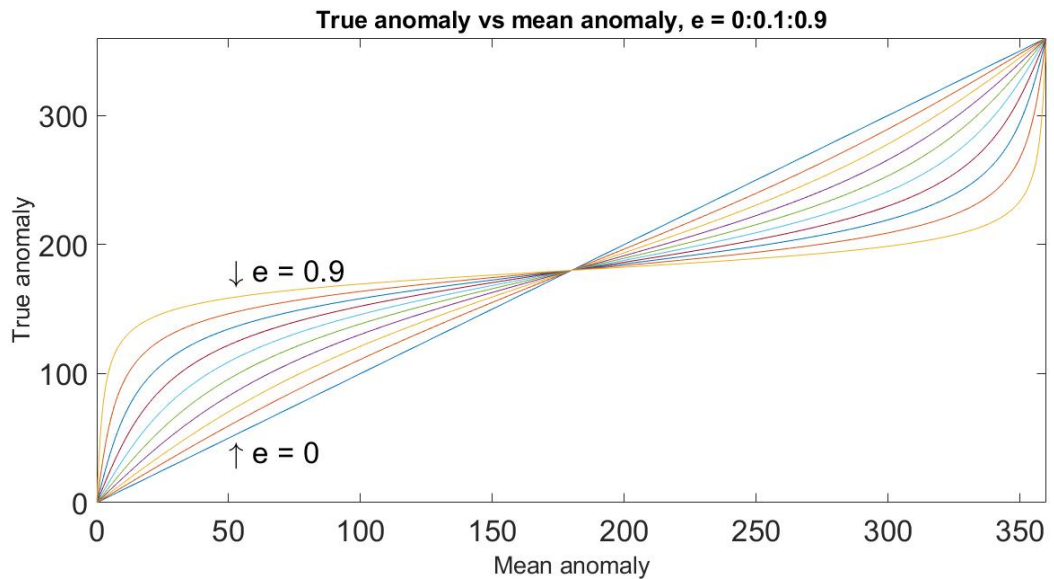


Figure A.7: **True anomaly vs mean anomaly for varying eccentricity values.** Relationship between the true anomaly (T) and the mean anomaly (M) is highlighted in this plot. A total of 10 different eccentricity (e) values are considered. Note that when $e = 0$, both true and mean anomalies are same.

A.4 True anomaly and eccentric anomaly (simpler representation)

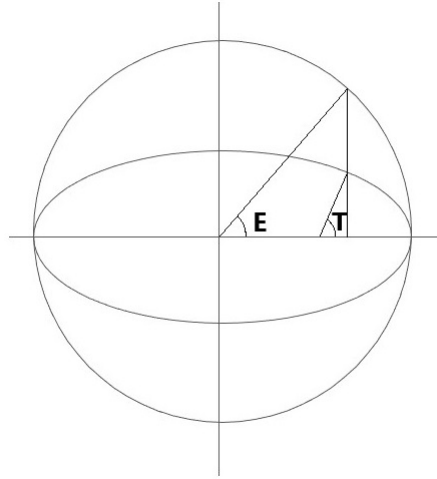


Figure A.8: **The true and eccentric anomalies (Not scaled to size)**. This plot provides a brief idea on the true and eccentric anomalies.

A.4 True anomaly and eccentric anomaly (simpler representation)

Fig. 1.2 already presented various anomalies. In this section we provide a simpler representation of true and eccentric anomalies using Fig. A.8.

Appendix B

Miscellaneous results

B.1 The EKF and UKF computing steps

Recall the classic Kalman filter stages mentioned in the Chapter 4 (Section 4.4), in this section we discuss computing steps for the extended and unscented Kalman filters.

B.1.1 The extended Kalman filter

The extended Kalman filter (EKF) (Bhaumik & Paresh, 2019; Gustafsson & Hendeby, 2012; Havlík & Straka, 2015; LaViola, 2003; Wikipedia contributors, 2020a) stages are mentioned below.

Propagation steps

$$\begin{aligned} \mathbf{x}_{k|k-1} &= \mathbf{f}(\mathbf{x}_{k-1|k-1}, \mathbf{u}_k) \\ \mathbf{P}_{k|k-1} &= \mathbf{F}_k \mathbf{P}_{k-1|k-1} \mathbf{F}_k^T + \mathbf{Q}_k \\ \mathbf{F}_k &= \left. \frac{\delta \mathbf{f}}{\delta \mathbf{x}} \right|_{\mathbf{x}_{k-1|k-1}, \mathbf{u}_k}. \end{aligned}$$

Update steps

$$\begin{aligned}
 \mathbf{y}_k &= \mathbf{z}_k - \mathbf{h}_k(\mathbf{x}_{k|k-1}), \quad \mathbf{H}_k = \left. \frac{\delta \mathbf{h}}{\delta \mathbf{x}} \right|_{\mathbf{x}_{k|k-1}} \\
 \mathbf{S}_k &= \mathbf{H}_k \mathbf{P}_{k|k-1} \mathbf{H}_k^T + \mathbf{R}_k \\
 \mathbf{K}_k &= \mathbf{P}_{k|k-1} \mathbf{H}_k^T \mathbf{S}_k^{-1} \\
 \mathbf{x}_{k|k} &= \mathbf{x}_{k|k-1} + \mathbf{K}_k \mathbf{y}_k \\
 \mathbf{P}_{k|k} &= (\mathbf{I} - \mathbf{K}_k \mathbf{H}_k) \mathbf{P}_{k|k-1}.
 \end{aligned}$$

Here, \mathbf{y}_k , \mathbf{S}_k , \mathbf{K}_k , $\mathbf{x}_{k|k}$ and $\mathbf{P}_{k|k}$ are called residual, innovation covariance, Kalman gain, posterior (updated) mean and posterior (updated) variance respectively. The state transition matrix and the observation matrices are indicated using \mathbf{F}_k and \mathbf{H}_k . Recall Chapter 4, the EKF performs the linearisation at the prior mean using the first order Taylor series expansion (See further information on the Taylor series in Section B.6).

B.1.2 The unscented Kalman filter

Before mentioning the propagation and update steps of an unscented Kalman filter (Julier, 2002; Julier & Uhlmann, 2004; Ponomareva *et al.*, 2010; Wan & Merwe, 2000), we mention how to compute various weights for performing the unscented Kalman filter. Note that some of these steps are already mentioned in Chapter 4 (Section 4.6.2). In this portion, we introduce several new parameters (with different names) for the discussion purpose.

Sigma points generation

$$\begin{aligned}
 \chi_0 &= \bar{\mathbf{y}} \\
 \chi_l &= \bar{\mathbf{y}} + \left(\sqrt{(l + \lambda^{\text{UKF}}) \mathbf{P}_{k-1|k-1}} \right)_l, \quad l = 1, \dots, N \\
 \chi_l &= \bar{\mathbf{y}} - \left(\sqrt{(l + \lambda^{\text{UKF}}) \mathbf{P}_{k-1|k-1}} \right)_l, \quad l = n + 1, \dots, 2N
 \end{aligned}$$

Further, note that we use the Cholesky decomposition (Cherny, 2005) for computing the matrix square root.

Weight computation

$$\begin{aligned}
 W_0^a &= \lambda^{\text{UKF}} / (l + \lambda^{\text{UKF}}), & W_0^v &= \lambda^{\text{UKF}} / (l + \lambda^{\text{UKF}}) + (1 - \alpha^{\text{UKF}^2} + \beta^{\text{UKF}}) \\
 W_l^a &= W_l^v = 1 / \{2(l + \lambda^{\text{UKF}})\} \\
 \lambda^{\text{UKF}} &= \alpha^{\text{UKF}^2} (l - \kappa^{\text{UKF}}) - l
 \end{aligned}$$

Note that α^{UKF} , β^{UKF} and κ^{UKF} are tuning parameters.

Propagation steps

$$\begin{aligned}
 \chi_{k|k-1} &= f(\mathbf{x}_{k-1|k-1}, \mathbf{u}_k) \\
 \mathbf{x}_k^- &= \sum_{l=0}^{2N} W_l^a \chi_{l,k|k-1} \\
 \mathbf{P}_k^- &= \sum_{l=0}^{2N} W_l^v [\chi_{l,k|k-1} - \mathbf{x}_k^-][\chi_{l,k|k-1} - \mathbf{x}_k^-]^T.
 \end{aligned}$$

Update steps

$$\begin{aligned}
 \gamma_{k|k-1} &= H[\chi_{k|k-1}] \\
 \mathbf{y}_k^- &= \sum_{l=0}^{2N} W_l^a \gamma_{l,k|k-1} \\
 \mathbf{P}_{\mathbf{y}_k} &= \sum_{l=0}^{2N} W_l^v [\gamma_{l,k|k-1} - \mathbf{y}_k^-][\gamma_{l,k|k-1} - \mathbf{y}_k^-]^T \\
 \mathbf{K}_k &= \left(\sum_{l=0}^{2N} W_l^v [\chi_{l,k|k-1} - \mathbf{x}_k^-][\gamma_{l,k|k-1} - \mathbf{y}_k^-]^T \right) \mathbf{P}_{\mathbf{y}_k}^{-1} \\
 \mathbf{x}_{k|k} &= \mathbf{x}_k^- + \mathbf{K}_k (\mathbf{z}_k - \mathbf{y}_k^-) \\
 \mathbf{P}_{k|k} &= \mathbf{P}_k^- - \mathbf{K}_k \mathbf{P}_{\mathbf{y}_k} \mathbf{K}_k^T.
 \end{aligned}$$

First, we compute various weights (using tuning parameters) and the sigma points (propagated). During the update stage we compute the transformed sigma points (i.e., sigma points generated in the state space are then converted to the observation space). After that we follow various computation stages to compute the posterior mean and the variance. Note that \mathbf{K}_k is the Kalman gain and also called the cross covariance matrix.

B.2 Rotation matrix

- (a) A 2-dimensional rotation matrix (Curtis, 2006; Evans, 2001) which rotates points located in the xy plane by an angle θ takes the following form,

$$\mathbf{R}(\theta) = \begin{bmatrix} \cos \theta & -\sin \theta \\ \sin \theta & \cos \theta \end{bmatrix}$$

- (b) In general 3-dimensional rotation matrices (Curtis, 2006; Evans, 2001) can be built from similar rotations by holding one of the coordinate axes fixed.

- (1) Rotation with respect to the x axis (rotation angle θ),

$$\mathbf{R}_x = \begin{bmatrix} 1 & 0 & 0 \\ 0 & \cos \theta & -\sin \theta \\ 0 & \sin \theta & \cos \theta \end{bmatrix}.$$

- (2) Rotation with respect to the y axis (rotation angle θ),

$$\mathbf{R}_y = \begin{bmatrix} \cos \theta & 0 & \sin \theta \\ 0 & 1 & 0 \\ -\sin \theta & 0 & \cos \theta \end{bmatrix}.$$

- (3) Rotation with respect to the z axis (rotation angle θ),

$$\mathbf{R}_z = \begin{bmatrix} \cos \theta & \sin \theta & 0 \\ \sin \theta & \cos \theta & 0 \\ -0 & 0 & 1 \end{bmatrix}.$$

B.3 Mahalanobis distance vs. Euclidean distance

The Mahalanobis distance (Mardia *et al.*, 1979; Mclachlan, 1999) (say, d_{Mahal}) indicates the distance between vector \mathbf{x} and a distribution with mean $\boldsymbol{\mu}$ (and variance matrix $\boldsymbol{\Sigma}$) in number of standard deviations (i.e., how many standard deviations away). Note that the Euclidean distance (say, d_{Euclid}) is the original distance between two data points (basically it is the straight line distance between vector \mathbf{x} and the distribution mean $\boldsymbol{\mu}$). To understand the difference between two distances consider the following example.

B.3 Mahalanobis distance vs. Euclidean distance

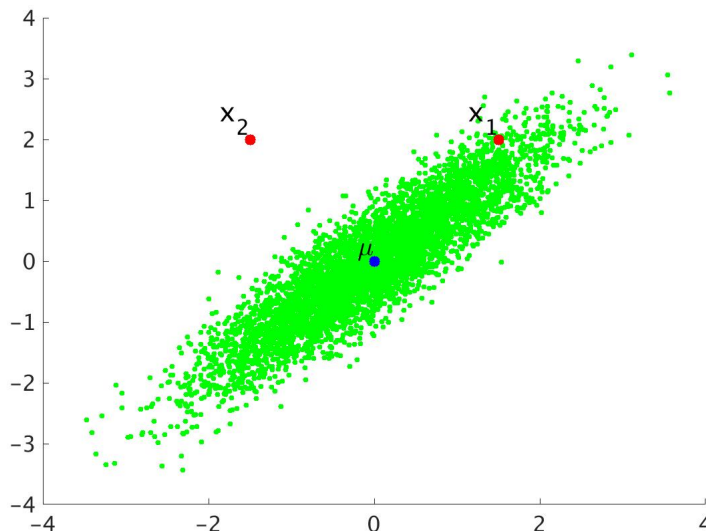


Figure B.1: **Euclidean distance vs. Mahalanobis distance.** Of course, x_1 is part of the distribution $D_{\text{bivariate}}$ but x_2 is not. However, the Euclidean distances are same for both the points.

$$d_{\text{Mahal}} = \sqrt{(\mathbf{x} - \boldsymbol{\mu}) \boldsymbol{\Sigma}^{-1} (\mathbf{x} - \boldsymbol{\mu})^T},$$
$$d_{\text{Euclid}} = \sqrt{(\mathbf{x} - \boldsymbol{\mu}) (\mathbf{x} - \boldsymbol{\mu})^T}.$$

Comparing the Euclidean distance and the Mahalanobis distance

Consider a bivariate normal distribution (say, $D_{\text{bivariate}}$) with $\boldsymbol{\mu} = [0, 0]^T$ and $\boldsymbol{\Sigma} = \begin{bmatrix} 1 & 0.9 \\ 0.9 & 1 \end{bmatrix}$ and we want to compute the Euclidean and Mahalanobis distances for points \mathbf{x}_1 ($[1.5, 2]^T$) and \mathbf{x}_2 ($[-1.5, 2]^T$) to understand whether \mathbf{x}_1 and/or \mathbf{x}_2 are part of the distribution $D_{\text{bivariate}}$ or not. Fig. B.1 shows the distribution and points \mathbf{x}_1 , \mathbf{x}_2 and $\boldsymbol{\mu}$. Further, results are summarized in Table B.1.

By comparing results obtained in Table B.1, we can conclude that Mahalanobis distance is much more effective than the Euclidean distance for this example.

B.4 The density computation for a bivariate normal distribution

Table B.1: Comparing the Mahalanobis distance and the Euclidean distance.

Computation method	\mathbf{x}_1	\mathbf{x}_2
Euclidean distance	2.50	2.50
Mahalanobis distance	2.11	7.83

B.4 The density computation for a bivariate normal distribution

The probability density function for a univariate normal distribution can be written as (Mardia *et al.*, 1979),

$$p(\mathbf{x}; \boldsymbol{\mu}, \boldsymbol{\Sigma}) = \frac{1}{\sqrt{2\pi|\boldsymbol{\Sigma}|}} \exp\left(-\frac{1}{2}(\mathbf{x} - \boldsymbol{\mu})^T \boldsymbol{\Sigma}^{-1}(\mathbf{x} - \boldsymbol{\mu})\right).$$

For a bivariate normal distribution,

$$\mathbf{x} = \begin{bmatrix} x_1 \\ x_2 \end{bmatrix}, \quad \boldsymbol{\mu} = \begin{bmatrix} \mu_1 \\ \mu_2 \end{bmatrix}, \quad \boldsymbol{\Sigma} = \begin{bmatrix} \Sigma_1 & \rho_{\text{cor}}\sigma_1\sigma_2 \\ \rho_{\text{cor}}\sigma_1\sigma_2 & \Sigma_2 \end{bmatrix}.$$

Here, ρ denotes the correlation ($\rho_{\text{cor}} = \frac{\text{COV}(X_1, X_2)}{\sigma_1\sigma_2}$). Further, σ_1 ($\Sigma_1 = \sigma_1^2$) and σ_2 ($\Sigma_2 = \sigma_2^2$) are standard deviations.

Then,

$$\begin{aligned} (\mathbf{x} - \boldsymbol{\mu})^T \boldsymbol{\Sigma}^{-1}(\mathbf{x} - \boldsymbol{\mu}) &= \frac{1}{\Sigma_1 \Sigma_2 (1 - \rho_{\text{cor}}^2)} \begin{bmatrix} x_1 - \mu_1 \\ x_2 - \mu_2 \end{bmatrix}^T \begin{bmatrix} \Sigma_2 & -\rho_{\text{cor}}\sigma_1\sigma_2 \\ -\rho_{\text{cor}}\sigma_1\sigma_2 & \Sigma_1 \end{bmatrix} \begin{bmatrix} x_1 - \mu_1 \\ x_2 - \mu_2 \end{bmatrix} \\ &= \frac{1}{(1 - \rho_{\text{cor}}^2)} \left(\frac{(x_1 - \mu_1)^2}{\Sigma_1} - 2\rho_{\text{cor}} \frac{(x_1 - \mu_1)(x_2 - \mu_2)}{\sigma_1\sigma_2} + \frac{(x_2 - \mu_2)^2}{\Sigma_2} \right). \end{aligned}$$

The density can be written as,

$$f(x_1, x_2) = \frac{1}{2\pi\sigma_1\sigma_2\sqrt{1 - \rho_{\text{cor}}^2}} \exp\left[\frac{-1}{2} \frac{1}{(1 - \rho_{\text{cor}}^2)} \left(\frac{(x_1 - \mu_1)^2}{\Sigma_1} - 2\rho_{\text{cor}} \frac{(x_1 - \mu_1)(x_2 - \mu_2)}{\sigma_1\sigma_2} + \frac{(x_2 - \mu_2)^2}{\Sigma_2} \right)\right].$$

Further, if $\rho_{\text{cor}} = 0$, then,

$$f(x_1, x_2) = \frac{1}{2\pi\sigma_1\sigma_2} \exp\left[\frac{-1}{2} \left(\frac{(x_1 - \mu_1)^2}{\Sigma_1} + \frac{(x_2 - \mu_2)^2}{\Sigma_2} \right)\right].$$

B.5 The Gram-Schmidt process

The rotation matrix $\mathbf{G}^{(c)}$ mentioned in Chapters 1, 2, 3 is computed using the Gram-Schmidt algorithm (Salehi & Dehkordi, 2015; Thornton & Bierman, 1975) (or the qr decomposition)

Any matrix (say, \mathbf{A}) can be written as $\mathbf{A} = \mathbf{QR}$, where

$$\mathbf{A} = [a_1|a_2|\dots|a_n], \quad (\text{B.1})$$

$$u_1 = a_1, \quad e_1 = \frac{u_1}{\|u_1\|}, \quad (\text{B.2})$$

$$u_2 = a_2 - (a_2 \cdot e_1)e_1, \quad e_2 = \frac{u_2}{\|u_2\|}, \quad (\text{B.3})$$

$$u_{k+1} = a_{k+1} - (a_{k+1} \cdot e_1)e_1 - \dots - (a_{k+1} \cdot e_k)e_k, \quad e_{k+1} = \frac{u_{k+1}}{\|u_{k+1}\|}, \quad (\text{B.4})$$

$$\mathbf{Q} = [e_1, e_2, \dots, e_n], \quad (\text{B.5})$$

$$\mathbf{R} = \mathbf{Q}^T \mathbf{A}. \quad (\text{B.6})$$

Note that for our case \mathbf{Q} is the rotation matrix and \mathbf{A} consists of initial Cartesian-ECI state vectors.

B.6 Taylor series expansion

The Taylor series expansion (Smith *et al.*, 2011; Wikipedia contributors, 2020d) is an infinitely differentiable series and can be written as,

$$f(a) + \frac{f'(a)}{1!}(x-a) + \frac{f''(a)}{2!}(x-a)^2 + \frac{f'''(a)}{3!}(x-a)^3 + \dots \quad (\text{B.7})$$

In B.7, the Taylor series expansion of $f(x)$ is taken at a .

The Taylor series expansion of $\frac{1}{1+x}$ can be written as

$$\frac{1}{1+x} = 1 - x + x^2 - x^3 + x^4 + \dots \quad (\text{B.8})$$

Further, if x is small, Equation (B.8) takes the form,

$$\frac{1}{1+x} \approx 1 - x.$$

B.7 Matrix basics

- (1) Suppose \mathbf{A} and \mathbf{B} are two matrices with same size $l_1 \times l_2$ then,

$$\begin{aligned}\mathbf{A} + \mathbf{B} &= \mathbf{B} + \mathbf{A}, \\ \mathbf{A} + \mathbf{B} &= (a_{ij} + b_{ij})_{l_1 \times l_2}, \\ c(\mathbf{A} + \mathbf{B}) &= c\mathbf{A} + c\mathbf{B} = c(a_{ij})_{l_1 \times l_2} + c(b_{ij})_{l_1 \times l_2},\end{aligned}$$

where, c is a real number.

- (2) Suppose \mathbf{A} and \mathbf{B} with sizes $l_1 \times l_2$ and $l_2 \times l_3$ respectively and their product $\mathbf{C} = \mathbf{AB}$ (size of \mathbf{C} is $l_1 \times l_3$) then,

$$c_{ij} = \sum_{k=1}^{l_2} a_{ik} b_{kj}, \quad i = 1, \dots, l_1, \quad j = 1, \dots, l_3.$$

- (3) Suppose \mathbf{A} , \mathbf{B} and \mathbf{D} are three matrices with sizes $l_1 \times l_2$, $l_2 \times l_3$ and $l_2 \times l_3$ respectively then,

$$\begin{aligned}\mathbf{A}(\mathbf{B} + \mathbf{D}) &= \mathbf{AB} + \mathbf{AD}, \\ (\mathbf{B} + \mathbf{D})\mathbf{A} &= \mathbf{BA} + \mathbf{DA}.\end{aligned}$$

- (4) Suppose \mathbf{A} and \mathbf{B} two matrices with sizes $l_1 \times l_2$ and $l_2 \times l_3$ respectively then,

$$\begin{aligned}(\mathbf{A}^T)^T &= \mathbf{A}, \\ (\mathbf{A} + \mathbf{B})^T &= \mathbf{A}^T + \mathbf{B}^T, \\ (\mathbf{AB})^T &= \mathbf{B}^T \mathbf{A}^T.\end{aligned}$$

- (5) Suppose \mathbf{A} is a matrix with size $l_1 \times l_2$ and $\det(\mathbf{A})$ denotes the determinant of \mathbf{A} then,

$$\det(\mathbf{A}^T) = \det(\mathbf{A}).$$

B.8 Key MATLAB functions used in this thesis

- (6) Suppose \mathbf{A} and \mathbf{B} are two square matrices with size $l_1 \times l_1$ then, diagonal elements of \mathbf{A} . Further,

$$\begin{aligned}\text{trace}(\mathbf{A}^T) &= \text{trace}(\mathbf{A}), \\ \text{trace}(c\mathbf{A}) &= c\text{trace}(\mathbf{A}), \\ \text{trace}(\mathbf{A}^T + \mathbf{B}^T) &= \text{trace}(\mathbf{A} + \mathbf{B}) = \text{trace}(\mathbf{A} + \mathbf{B})^T = \text{trace}(\mathbf{A}) + \text{trace}(\mathbf{B}).\end{aligned}$$

- (7) Suppose \mathbf{A} is a square matrix (size $l_1 \times l_1$) and invertible and \mathbf{E} (unique) denotes the inverse of \mathbf{A} then,

$$\begin{aligned}\mathbf{AE} &= \mathbf{EA} = \mathbf{I}, \\ \det(\mathbf{A}) &\neq 0, \\ (\mathbf{A}^{-1})^T &= (\mathbf{A}^T)^{-1}.\end{aligned}$$

- (8) A matrix \mathbf{A} is a symmetric matrix iff i) \mathbf{A} is a square matrix and ii) $\mathbf{A} = \mathbf{A}^T$.

- (9) A matrix \mathbf{A} is a Skew-symmetric matrix iff i) \mathbf{A} is a square matrix and ii) $\mathbf{A} = -\mathbf{A}^T$.

- (10) A matrix \mathbf{A} is orthogonal iff i) \mathbf{A} is a square matrix and ii) $\mathbf{A}^{-1} = \mathbf{A}^T$. Further, we can also write,

$$\mathbf{A}^T \mathbf{A} = \mathbf{A} \mathbf{A}^T = \mathbf{I}.$$

In addition, if $\det(\mathbf{A}) = 1$, then \mathbf{A} is a rotation matrix (see Section B.2).

- (11) A symmetric matrix \mathbf{A} is positive definite if $\mathbf{x}^T \mathbf{A} \mathbf{x} > 0$ for all $\mathbf{x} \neq 0$.

- (12) A symmetric matrix \mathbf{A} is positive definite if $\mathbf{x}^T \mathbf{A} \mathbf{x} \geq 0$ for all $\mathbf{x} \neq 0$.

B.8 Key MATLAB functions used in this thesis

- (1) `randn`. To generate normally distributed random variables.
- (2) `det`. To compute the determinant of a matrix \mathbf{A} .

B.8 Key MATLAB functions used in this thesis

- (3) `inv`. To compute the matrix inverse.
- (4) `dot`. To compute the dot product.
- (5) `cross`. To compute the cross product.
- (6) `qr`. To perform the qr decomposition.
- (7) `chol`. To compute the Cholesky factorization.

Appendix C

List of objects

This portion summarizes various objects used in this thesis.

- (1) **Object 1 (O1).** $A = 9078$ km, $B = 2.6$ km/sec and $C = 8.1$ km/sec, period = 712 minutes, $e = 0.7$.

Object classification. HEO object.

Purpose of use. To show that AST coordinates are able to preserve approximate normality under extreme circumstances. Further, we also use this object for treating filtering and association examples.

- (2) **Object 2 (O2).** $A = 8582$ km, $B = 0.88$ km/sec and $C = 6.74$ km/sec, period = 131 minutes, $e = 0.13$.

Object classification. LEO object.

Purpose of use. This object is located neither at a circular nor at a highly eccentric orbit. We use this object to demonstrate angles-only propagation (true angles-only, Chapter 3). In addition, we also use this object for analyzing the break-up event in Chapter 2 and for solving association problems in Chapter 6.

- (3) **Object 3 (O3).** $A = 42167$ km, $B = 5e^{-04}$ km/sec and $C = 3.07$ km/sec, period = 1436 minutes, $e = 5e^{-03}$.

Object classification. GEO object.

Purpose of use. This object (along with O2) is used to demonstrate the concept of observer-centric reference frame.

-
- (4) **Object 4 (O4).** $A = 9078$ km, $B = 2.50$ km/sec and $C = 8.1$ km/sec, period = 654 minutes, $e = 0.67$.

Object classification. HEO object.

Purpose of use. The normal direction vector ($\mathbf{h}^{(e)}$) and its magnitudes ($h^{(e)}$) for this object are same with the Object 1. This object is used to solve the ambiguity in custody problem.

- (5) **Object 5 (O5).** $A = 7113$ km, $B = 4e^{-03}$ km/sec, $C = 7.47$ km/sec, period = 99 minutes, $e = 9e^{-05}$.

Object classification. LEO object (near circular).

Purpose of use. This object is located at a near circular LEO orbit, we use this object to show limitations of the Keplerian orbital elements (in statistical normality analysis).

Appendix D

Papers

Published papers

- (1) S. Bhattacharjee, J. T. Kent, I. Hussein, and M. K. Jah, “Bayesian Filtering using Directional Statistics for Space Debris Tracking Problem”, 68th International Astronautical Congress, Adelaide, Australia, IAF/ IAC 2017.
- (2) S. Bhattacharjee, J. T. Kent, I. Hussein, and M. K. Jah, “Application of Directional Statistics to Problems in SSA”, 1st IAA Conference on Space Situational Awareness, Orlando, Florida, USA, 2017.
- (3) S. Bhattacharjee, J. T. Kent, I. Hussein, and M. K. Jah, “Filtering under ambiguity for the debris tracking problem”, 69th International Astronautical Congress, 2018.
- (4) S. Bhattacharjee, J. T. Kent, I. Hussein, and M. K. Jah, “Understanding the effect of perturbations on the Gaussianity of various coordinates for the space object tracking problem”, AMOS conference, 2018.
- (5) S. Bhattacharjee, J. T. Kent, I. Hussein, and M. K. Jah, “Tackling association and tracking problems using directional statistics to model uncertainty”, 69th International Astronautical Congress, 2018.
- (6) J. T. Kent, S. Bhattacharjee, I. Hussein, and M. K. Jah, “Filtering when object custody is ambiguous”, IEEE, 21st International Conference on Information Fusion, Cambridge, UK, 2018.

-
- (7) J. T. Kent, S. Bhattacharjee, I. Hussein, and M. K. Jah, "Orbital Error Propagation Analysis using Directional Statistics for Space Objects", 27th space flight mechanics meeting, San Antonio, Texas, USA, AIAA/AAS, 2017.
 - (8) J. T. Kent, S. Bhattacharjee, I. Hussein, and M. K. Jah, "Angles-Only Data Association Using Directional Discriminant Analysis", 27th space flight mechanics meeting, San Antonio, Texas, USA, AIAA/AAS, 2017.
 - (9) J. T. Kent, S. Bhattacharjee, I. Hussein, and M. K. Jah, "Geometric re-structurization of the space object tracking problem for improved uncertainty representation", 7th European Conference on Space Debris, ESA/ESOC, 2017.
 - (10) J. T. Kent, S. Bhattacharjee, I. Hussein, and M. K. Jah, "The Performance of a Direction-Based Bayesian Filter in the Orbital Tracking Problem", the Astrodynamics Specialist Conference, Stevenson, USA, AIAA/AAS, 2017.
 - (11) W. Faber, I. Hussein, J. T. Kent, S. Bhattacharjee, and M. K. Jah, "Optical Data Association in a Multiple Hypothesis Framework with Maneuvers", the Astrodynamics Specialist Conference, Stevenson, USA, AIAA/AAS, 2017.
 - (12) W. Faber, I. Hussein, J. T. Kent, S. Bhattacharjee, and M. K. Jah, "FBK Optical Data Association in a Multi-Hypothesis Framework with Maneuvers", AMOS conference, 2017.
 - (13) J. T. Kent, S. Bhattacharjee, I. Hussein, and M. K. Jah, "Nonlinear Filtering using Directional Statistics for the Orbital Tracking Problem with Perturbation Effects", 28th space flight mechanics meeting, Florida, USA, AIAA/AAS, 2018.
 - (14) W. Faber, I. Hussein, J. T. Kent, S. Bhattacharjee, and M. K. Jah, "Optical Data Processing Using Directional Statistics in a Multi-Hypothesis Framework with Maneuvers", 28th space flight mechanics meeting, Florida, USA, AIAA/AAS, 2018.

-
- (15) J. T. Kent, S. Bhattacharjee, I. Hussein, and M. K. Jah, “FISHER-BINGHAM-KENT Mixture Models for Angles-Only Observation Processing”, 28th space flight mechanics meeting, Florida, USA, AIAA/AAS, 2018.
 - (16) S. Bhattacharjee, J. T. Kent, W. Faber, I. Hussein, and M. K. Jah, “Revisiting the filtering problem”, IAC, 2019, October.
 - (17) S. Bhattacharjee, J. T. Kent, W. Faber, I. Hussein, and M. K. Jah, “Understanding the distribution of the propagated angles-only position vector”, IAC, 2019, October.

Papers recently finished and uploaded at the arXiv

- (1) J. T. Kent, S. Bhattacharjee, I. Hussein, and W.R. Faber, “Observation-centered Kalman filters”. (Preprint: arXiv:1907.13501).
- (2) J. T. Kent, S. Bhattacharjee, I. Hussein, and W.R. Faber, “Revisiting the orbital tracking problem”. (Preprint: arXiv:1909.03793).

Papers currently under preparation/ready to submit

- (1) S. Bhattacharjee, J. T. Kent, W. Faber, I. Hussein, and M. K. Jah, “Representing uncertainty associated with the angles-only position of an orbiting object”.
- (2) J. T. Kent, S. Bhattacharjee, I. Hussein, and W.R. Faber, “Performance analysis of the Fisher-Bingham distribution for representing propagated orbital uncertainty”.
- (3) S. Bhattacharjee, J. T. Kent, W. Faber, I. Hussein, and M. K. Jah, “Tracking space object under ambiguity”.

References

- BHATTACHARJEE, S., KENT, J.T., HUSSEIN, I.I. & JAH, M.K. (2017a). Application of directional statistics to problems in ssa. In *1st IAA Conference on Space Situational Awareness, Orlando, Florida*. 34, 137
- BHATTACHARJEE, S., KENT, J.T., HUSSEIN, I.I. & JAH, M.K. (2017b). Bayesian filtering using directional statistics for space debris tracking problem. In *68th International Astronautical Congress, Adelaide, Australia*, IAF. 34
- BHATTACHARJEE, S., KENT, J.T., HUSSEIN, I.I., FABER, W.R. & JAH, M.K. (2018a). Filtering under ambiguity for the debris tracking problem. In *69th International Astronautical Congress, Bremen, Germany*, IAF. 34
- BHATTACHARJEE, S., KENT, J.T., HUSSEIN, I.I., FABER, W.R. & JAH, M.K. (2018b). Tackling association and tracking problems using directional statistics to model uncertainty. In *69th International Astronautical Congress, Bremen, Germany*, IAF. 34
- BHATTACHARJEE, S., KENT, J.T., HUSSEIN, I.I., FABER, W.R. & JAH, M.K. (2018c). Understanding the effect of perturbations on the gaussianity of various coordinates for the space object tracking problem. In *AMOS conference, Hawaii, USA*. 34
- BHATTACHARJEE, S., KENT, J.T., FABER, W. & HUSSEIN, I. (2019a). Understanding the distribution of the propagated angles-only position vector. In *Proceedings of the International Astronautical Congress, Bremen, Germany*, IAC. 34, 35

REFERENCES

- BHATTACHARJEE, S., KENT, J.T., FABER, W. & HUSSEIN, I.I. (2019b). Revisiting the filtering problem. In *Proceedings of the International Astronautical Congress, Bremen, Germany*, IAC. 34
- BHAUMIK, S. & PARESH, D. (2019). *Nonlinear Estimation Methods and Applications with Deterministic Sample Points; The Kalman filter and the extended Kalman filter*, 27–50. Taylor Francis Group. 31, 175
- BHUSAL, R. & SUBBARAO, K. (2019). Generalized polynomial chaos expansion approach for uncertainty quantification in small satellite orbital debris problems. *The Journal of the Astronautical Sciences*, **0021-9142**, 1–29. 30
- CEFOLA, P. (1972). Equinoctial orbit elements - application to artificial satellite orbits. In *AIAA/AAS Astrodynamics Conference, Palo Alto, CA, USA*, AIAA/AAS. 49
- CHEN, Z. (2003). Bayesian filtering: From Kalman filters to particle filters, and beyond. *Statistics*, **182**. 31, 32, 112, 113
- CHERNY, S. (2005). Cholesky decomposition. *Encyclopedia of Statistics in Behavioral Science*. 176
- CURTIS, H. (2006). *Orbital Mechanics for Engineering Students*, 1–187. Elsevier Aerospace Engineering Series. 37, 39, 40, 43, 46, 47, 48, 164, 178
- ESA (2020a). Space debris by the numbers. https://www.esa.int/Safety_Security/Space_Debris/Space_debris_by_the_numbers. 28
- ESA (2020b). Types of orbits. https://www.esa.int/Enabling_Support/Space_Transportation/Types_of_orbits. 46, 47
- EVANS, P. (2001). Rotations and rotation matrices. *Acta crystallographica. Section D, Biological crystallography*, **57**, 1355–1359. 178
- FABER, W.R., HUSSEIN, I.I., KENT, J.T., S, B. & JAH, M.K. (2017). FBK optical data association in a multi-hypothesis framework with maneuvers. In *AMOS conference, Hawaii, USA*. 137

REFERENCES

- FENFENA, X., SHISHIA, C. & YING, X. (2014). Dynamic system uncertainty propagation using polynomial chaos. *Chinese Journal of Aeronautics*, **27**, 1156–1170. [30](#)
- FITZPATRICK, R. (2012). Orbital elements. <https://farside.ph.utexas.edu/teaching/celestial/Celestial/node34.html>. [53](#)
- GUSTAFSSON, F. & HENDEBY, G. (2012). Some relations between extended and unscented Kalman filters. *IEEE Transactions on Signal Processing*, **60**, 545–555. [175](#)
- GUSTAFSSON, F., GUNNARSSON, F., BERGMAN, N., FORSELL, U., JANSSON, J., KARLSSON, R. & NORDLUND, P.J. (2002). Particle filters for positioning navigation and tracking. *IEEE Transactions on Signal Processing*, **50**, 425–437. [32](#), [136](#)
- HAVLÍK, J. & STRAKA, O. (2015). Performance evaluation of iterated extended Kalman filter with variable step-length. *Journal of Physics: Conference Series*, *IOP Publishing*, **659**, 12–22. [32](#), [175](#)
- HENZE, N. & ZIRKLER, B. (1990). A class of invariant consistent tests for multivariate normality. *Biometrika*, **19(10)**, 3595–3617. [162](#)
- HONGBIN, M., LIPING, Y., YUANQING, X. & MENGYIN, F. (2020). *Kalman Filtering and Information Fusion*. Springer Nature. [31](#)
- HUSSEIN, I., I, CHRISTOPHER, T.R., W & WILKINS, P., M (2015). Track-to-track association using bhattacharyya divergence. In *AMOS conference, Hawaii, USA*. [31](#), [137](#), [138](#)
- JULIER, S., UHLMANN, J. & DURRANT-WHYTE, F., H (2000). A new method for the nonlinear transformation of means and covariances in filters and estimators. *IEEE Transactions on Automatic Control*, **45**, 477–482. [119](#), [126](#)
- JULIER, S.J. (2002). The scaled unscented transformation. In *Proceedings of the 2002 American Control Conference (IEEE Cat. No.CH37301)*, vol. 6, 4555–4559, IEEE. [31](#), [176](#)

REFERENCES

- JULIER, S.J. & UHLMANN, J.K. (2004). Unscented filtering and nonlinear estimation. *Proceedings of the IEEE*, **92**, 401–422. [31](#), [176](#)
- JUNKINS, J.L., AKELLA, M.R. & ALFRIEND, K.T. (1996). Non-gaussian error propagation in orbital mechanics. *Journal of the Astronautical Sciences*, **44**, 541–563. [29](#)
- KENT, J.T., HUSSEIN, I.I. & JAH, M.K. (2016). Directional distributions in tracking of space debris. In *Proceedings of the 19th International Conference on Information Fusion (FUSION), Heidelberg, Germany*, IEEE. [29](#)
- KENT, J.T., BHATTACHARJEE, S., HUSSEIN, I.I. & JAH, M.K. (2017a). Angles-only data association using directional discriminant analysis. In *27th space flight mechanics meeting, San Antonio, USA*. [34](#), [137](#)
- KENT, J.T., BHATTACHARJEE, S., HUSSEIN, I.I. & JAH, M.K. (2017b). Geometric restructurization of the space object tracking problem for improved uncertainty representation. In *Proceedings of the 7th European Conference on Space Debris, Darmstadt, Germany*. [34](#)
- KENT, J.T., BHATTACHARJEE, S., HUSSEIN, I.I. & JAH, M.K. (2017c). Orbital error propagation analysis using directional statistics for space objects. In *27th space flight mechanics meeting, San Antonio, Texas, USA*, AIAA/AAS. [34](#)
- KENT, J.T., BHATTACHARJEE, S., HUSSEIN, I.I. & JAH, M.K. (2018a). Filtering when object custody is ambiguous. In *IEEE, 21st International Conference on Information Fusion, Cambridge, UK*, IEEE. [34](#)
- KENT, J.T., BHATTACHARJEE, S., HUSSEIN, I.I. & JAH, M.K. (2018b). Fisher-Bingham-Kent mixture models for angles-only observation processing. In *28th space flight mechanics meeting, Florida, USA*, AIAA/AAS. [34](#)
- KENT, J.T., BHATTACHARJEE, S., HUSSEIN, I.I. & JAH, M.K. (2018c). Non-linear filtering using directional statistics for the orbital tracking problem with perturbation effects. In *28th space flight mechanics meeting, Florida, USA*, AIAA/AAS. [34](#)

REFERENCES

- KENT, J.T., BHATTACHARJEE, S., FABER, W.R. & HUSSEIN, I.I. (2019a). Observation-centered Kalman filter. *arXiv:1907.13501*. [32](#), [34](#), [35](#)
- KENT, J.T., BHATTACHARJEE, S., FABER, W.R. & HUSSEIN, I.I. (2019b). Revisiting the orbital tracking problem. *arXiv:1909.03793*. [32](#), [34](#), [35](#), [136](#)
- KORKMAZ, S., GOKSULUK, D. & ZARARSIZ, G. (2014). MVN: An R package for assessing multivariate normality. *The R Journal*, **6**, 151–162. [54](#), [162](#)
- LAVIOLA, J.J. (2003). A comparison of unscented and extended Kalman filtering for estimating quaternion motion. In *Proc American Control Conf*, 2435–2440. [175](#)
- MARDIA, K.V. (1970). Measures of multivariate skewness and kurtosis with applications. *Biometrika*, **57**, 519–530. [162](#)
- MARDIA, K.V., KENT, J.T. & BIBBY, J.M. (1979). *Multivariate Analysis*, 1–85. Academic Press. [54](#), [142](#), [162](#), [178](#), [180](#)
- MCCABE, S., J & DEMARS, J., K (2014). Particle filter methods for space object tracking. In *The Astrodynamics Specialist Conference, Stevenson, USA*, AIAA/AAS. [30](#)
- MCLACHLAN, G. (1999). Mahalanobis distance. *Resonance*, **4**, 20–26. [178](#)
- MIT (2010). The Shapiro-Wilk and related tests for normality. <https://math.mit.edu/~rmd/465/shapiro.pdf>. [54](#)
- MORETTI, N., RUTTEN, M., BESSELL, T. & MORREALE, B. (2017). Autonomous space object catalogue construction and upkeep using sensor control theory. In *AMOS conference, Hawaii, USA*. [137](#), [138](#)
- PARK, I. & SCHEERES, D.J. (2018). Hybrid method for uncertainty propagation of orbital motion. *Journal of Guidance, Control and Dynamics*, **41**, 240–254. [30](#)
- PARK, R.S. & SCHEERES, D.J. (2006). Nonlinear mapping of gaussian statistics: theory and applications to spacecraft trajectory design. *Journal of Guidance, Control and Dynamics*, **29**, 1367–1375. [30](#)

REFERENCES

- PARK, R.S. & SCHEERES, D.J. (2012). Analytical nonlinear propagation of uncertainty in the two body problem. *Journal of Guidance, Control and Dynamics*, **35**, 497–509. [30](#)
- PIROVANO, L., PRINCIPE, G. & ARMELLIN, R. (2020). Data association and uncertainty pruning for tracks determined on short arcs. *Celest Mech Dyn Astr*, **132**, 1–23. [138](#)
- PONOMAREVA, K., DATE, P. & WANG, Z. (2010). A new unscented kalman filter with higher order moment-matching. In *Proceedings of the 19th Int Symp Mathematical Theory of Networks and Systems, Budapest, Hungary*, 1609–1613, IEEE. [176](#)
- RAIHAN A, D., V & CHAKRAVORTY, S. (2018). An unscented kalman-particle hybrid filter for space object tracking. *J of Astronaut Science*, **65**, 111–134. [30](#)
- ROY, A.E. (2004). *Orbital Motion*, 1–72. Routledge. [33](#), [37](#), [39](#), [40](#), [49](#), [164](#)
- SALEHI, S. & DEHKORDI, R.M. (2015). Application of Gram-Schmidt orthogonalization method in uncertainty quantification of computational fluid dynamics problems with arbitrary probability distribution functions. *Modares Mechanical Engineering*. [181](#)
- SHAPIRO, S.S. & WILK, M.B. (1965). An analysis of variance test for normality (complete samples). *Biometrika*, **52**, 591–611. [54](#)
- SHIN, Y., YOON, S., SEO, Y., JIN, H. & SEON, J. (2015). Radiation effect for a cubesat in slow transition from the earth to the moon. *Advances in Space Research*, **31**. [48](#)
- SIGGES, F. & BAUM, M. (2017). A nearest neighbour ensemble kalman filter for multi-object tracking. In *2017 IEEE International Conference on Multisensor Fusion and Integration for Intelligent Systems (MFI)*, 227–232. [30](#)
- SIMINSKI, A., J, RUTTEN, M., WEIGEL, M. & FIEDLER, H. (2014). Catalog build-up for geostationary orbit using simulated short-arc tracklets. In *AMOS conference, Hawaii, USA*. [137](#)

REFERENCES

- SMITH, T., THOMPSON, J. & MOUNTCASTLE, D. (2011). Student understanding of Taylor series expansions in statistical mechanics. *Physical Review Special Topics - Physics Education Research*, **9**. [181](#)
- TCHAMOVA, A., SEMERDJIEV, T., KONSTANTINOVA, P. & DEZERT, J. (2004). *Generalized Data Association for Multitarget Tracking in Clutter*, 303–324. Advances and Applications of DSMT for Information Fusion, American Research Press. [138](#)
- THORNTON, C.L. & BIERMAN, G.J. (1975). Gram-schmidt algorithms for covariance propagation. In *1975 IEEE Conference on Decision and Control including the 14th Symposium on Adaptive Processes*, 489–498. [181](#)
- VALLADO, A., D & CEFOLA, J., P (2012). Two-line element sets practice and use. In *Proceedings of the International Astronautical Congress, Naples, Italy*, IAC. [31](#)
- VALLADO, D.A. (2001). *Fundamentals of Astrodynamics and Applications*, 1–231. Springer Science Business Media. [39](#), [40](#), [44](#), [48](#)
- VALLI, M., ARMELLIN, R., LIZIA, P. & LAVGNA, M. (2013). Non linear mapping of uncertainties in celestial mechanics. *Journal of Guidance, Control and Dynamics*, **36**, 48–63. [29](#)
- VITTALDEV, V., RUSSELL, R.P. & LINARES, R. (2016). Spacecraft uncertainty propagation using gaussian mixture models and polynomial chaos expansions. *Journal of Guidance, Control and Dynamics*, **39**, 2615–2626. [30](#)
- WAN, E.A. & MERWE, R.V.D. (2000). The unscented Kalman filter for non-linear estimation. In *Proc of the IEEE 2000 Adaptive Systems for Signal Processing, Communications, and Control Symposium*, 153–158, IEEE. [31](#), [176](#)
- WIKIPEDIA CONTRIBUTORS (2019). Earth-centered inertial — Wikipedia, the free encyclopedia. https://en.wikipedia.org/w/index.php?title=Earth-centered_inertial&oldid=931601689. [39](#)

REFERENCES

- WIKIPEDIA CONTRIBUTORS (2020a). Extended Kalman filter — Wikipedia, the free encyclopedia. https://en.wikipedia.org/w/index.php?title=Extended_Kalman_filter&oldid=942870361. 175
- WIKIPEDIA CONTRIBUTORS (2020b). Kalman filter — Wikipedia, the free encyclopedia. https://en.wikipedia.org/w/index.php?title=Kalman_filter&oldid=943554728. 113
- WIKIPEDIA CONTRIBUTORS (2020c). List of orbits — Wikipedia, the free encyclopedia. https://en.wikipedia.org/w/index.php?title=List_of_orbits&oldid=942841212. 46, 47
- WIKIPEDIA CONTRIBUTORS (2020d). Taylor series — Wikipedia, the free encyclopedia. https://en.wikipedia.org/w/index.php?title=Taylor_series&oldid=941973047. 181
- WOODBURN, J. & TANYGIN, S. (2014). Coordinate effects on the use of orbit error uncertainty. In *International Symposium on Space Flight Dynamics, Laurel, Maryland*. 31
- YANG, Z., LUO, Z., Y, LAPPAS, V. & TSOURDOS, A. (2018). Nonlinear analytical uncertainty propagation for relative motion near j2-perturbed, elliptic orbits. *Journal of Guidance, Control and Dynamics*, **41**, 888–903. 31
- YONGFANG, N. & TAO, Z. (2018). Scaling parameters selection principle for the scaled unscented kalman filter. *Journal of Systems Engineering and Electronics*, **29**, 601–610. 119
- YOUNGJOO, K. & HYOCHOONG, B. (2018). *Introduction to Kalman Filter and Its Applications*, 1–16. InTechOpen. 31, 112, 113
- ZHAN, R. & WAN, J. (2007). Iterated unscented Kalman filter for passive target tracking. *IEEE Transactions on aerospace and electronic systems*, **43**, 1155–1163. 32